ELECTRON BEAM WELDING OF ROLLED INCONEL 718

A Thesis

by

VIVEK R. PATEL

Submitted to the Office of Graduate and Professional Studies of
Texas A&M University
in partial fulfillment of the requirements for the degree of

MASTER OF SCIENCE

Chair of Committee,	Wayne Nguyen P. Hung
Committee Members,	Angie Hill Price
	Bruce Tai
Head of Department,	Andreas A. Polycarpou

May 2021

Major Subject: Mechanical Engineering

ABSTRACT

This study was conducted to investigate the effect of Electron Beam Welding parameters on the weld quality of thick rolled Inconel 718 plate and to optimize the same. A full-factorial experiment having nine heat inputs (three different levels of welding speed and beam current) was designed. The weld quality was characterized based on weld geometry, microhardness, and mechanical properties. The transverse section of a weld bead when observed under a high magnification microscope showed a typical nail-head-shaped fusion zone. Scanning Electron Microscopy with Energy Dispersive Spectroscopy was performed on fractured surfaces to analyze the material composition and inclusion defects. The fusion area and weld penetration depth were found to be directly proportional to the heat input. At the lowest heat input, the microhardness measurements at the beam entrance showed a softer and wider weld zone compared to the weld-bottom regions. The hardness values increased and became uniform at different weld depths post-heat treatment. Keyhole defects at the highest beam power can be removed by a suitable machining process post welding. All samples but one had tensile strength exceeding the specification for as-received rolled IN718; ductility of welded specimens also met the specification when welded with low heat input. At lower heat inputs, the welded samples fractured outside of the weld zone showing ductile fracture characteristics and indicated their exceptional weld strengths. These results provided a benchmark for comparison with a parallel study on Electron Beam Welding of Selective Laser Melted Inconel 718.

DEDICATION

I dedicate this work to the strongest and loving woman, my mother, Jayshreeben Patel who raised me in her hardships and always believed in my dreams to be the person I am today. I am always thankful to my brother, Dr. Anand Patel who supported me in my education and endeavors. This work goes in the memories of my late father, Dr. Rajeshbhai Patel who always dreamt big for me. I thank all for their care and love.

CONTRIBUTORS AND FUNDING SOURCES

Contributors

This work was supervised by a thesis committee consisting of Dr. Wayne Nguyen P. Hung, Dr. Bruce Tai of the Department of Mechanical Engineering, and Dr. Angie Hill Price of the Department of Manufacturing and Mechanical Engineering Technology.

James Hyder, Mike Corliss, David Hyder, and Mathew Carl of Knust-Godwin SBO facilitated manufacturing activities. Mr. Rodney Inmon of the Department of Aerospace Engineering assisted in Tensile Testing and Mr. Tom Stephens of Microscopy and Imaging Center guided on the usage of the Scanning Electron Microscope and Energy Dispersive Spectroscopy system.

All other work conducted for the thesis was completed by the student.

Funding Sources

Rolled Inconel 718 plate as raw material procurement and fabrication services were provided by Knust-Godwin SBO, Katy, Texas.

NOMENCLATURE

AM	Additive Manufacturing
AMS	Aerospace Material Specifications
ANOVA	Analysis of Variance
ASM	American Society for Metals
ASTM	American Society for Testing and Materials
CHT	Cyclic Solution Heat Treatment
CI	Confidence Interval
CW	Continuous Wave
DA	Direct Aged
DAZ	Diffusion Affected Zone
EBW	Electron Beam Welding
EDM	Electrical Discharge Machining
EDS	Energy Dispersive Spectroscopy
FSW	Friction Stir Welding
FZ	Fusion Zone
GTAW	Gas Tungsten Arc Welding
HAZ	Heat Affected Zone
HIP	Hot Isostatic Pressing
IN718	Inconel 718
ISZ	Isothermally Solidified Zone

LBW	Laser Beam Welding
OM	Optical Microscope
PWHT	Post-weld Heat Treatment
RD	Rolling Direction
SAE	Society of Automotive Engineering
SEM	Scanning Electron Microscopy
SS	Sum of Squares
STA	Solution Treated and Aged
SLM	Selective Laser Melting
TCL	Total Crack Length
UTS	Ultimate Tensile Strength
XRD	X-ray Diffraction
YS	Yield Strength

LIST OF SYMBOLS

α	significance level
ε_f	Elongation at Fracture
I	Beam Current
P	Electron Beam Power or Laser Power
S	Welding Speed
S_u	Ultimate Tensile Strength
S_y	Yield Strength
V	Beam Voltage

TABLE OF CONTENTS

Page

Page

LIST OF FIGURES

Page

Page

Page

Page

Page

LIST OF TABLES

Page

Page

1. INTRODUCTION

Inconel 718 (IN718) is a nickel-based austenitic superalloy that can be hardened by precipitation. Due to its superior high-temperature mechanical properties and corrosion resistance, it has a wide range of applications in the automobile, aerospace, nuclear, and petrochemical industry (Akca & Gürsel, 2015). Inconel also has good weldability as compared to other superalloys of similar chemical characteristics (Muralidharan et al., 1996). Advanced products operating at demanding conditions require components with complex geometries and tight tolerances; however, they are difficult and costly to be manufactured by conventional manufacturing processes. Selective laser melting (SLM), a powder bed fusion technique, can produce near-net-shaped metal parts, but one of the constraints on current SLM equipment is the limited working volume. The advent of metal 3D printing technology has shown the possibility to achieve intricacies in the design, but a large volume metal additive manufacturing process has economical and quality challenges.

It has thus become more evident to develop efficient ways to produce large components by successfully joining different SLM parts. Among all joining processes, electron beam welding (EBW) is among the best techniques for high quality and deep penetration (Norrish J., 2006). EBW has the ability to produce narrow HAZ with deep weld penetration resulting in a minimum alteration in the base metal characteristics. Published literature includes welding of rolled or extruded IN718 by different methods; joining of additively manufactured IN718 by Gas Tungsten Arc Welding (GTAW) and

brazing was performed by a few researchers, but none is yet to be found for EBW of 3D printed IN718. The objectives of this research are to:

- Understand the effect of EBW parameters on rolled IN718 weld quality characterized by weld geometry and mechanical properties of welds.
- Optimize parameters for EBW of rolled IN718 to obtain the best mechanical properties.
- Examine the feasibility and reliability of the deep weld of rolled IN718 by EBW.
- Set the benchmark results which then can be used at a later stage as a reference for comparison against SLM'ed IN718 components after joining by EBW.

2. LITERATURE REVIEW

Due to the popularity of IN718 in industry, various methods to join IN718 have been previously investigated by researchers. Laser Beam Welding and Electron Beam Welding are the most widely researched joining methods for wrought IN718. Whereas, Gas Tungsten Arc Welding (GTAW) and brazing have been explored for 3D printed IN718. The literature on these joining methods along with basic characteristics of rolled IN718 is discussed below.

2.1. Characteristics of Inconel Alloy 718 (IN718)

Having better mechanical properties and corrosion in the working temperature range of 250 °C – 700 °C, it was important to understand involved thermal treatments in the manufacturing and established specifications of the nickel-chromium-based alloy IN718. It was equally important to inspect the microstructure, various phases, base metal grain size effects as the relevance of the results depend upon the kinetics of time-dependent phenomena during welding. The mechanical behavior of rolled specimens in different orientations was observed to get useful motivation for the process development of the experiment in a later stage.

2.1.1. Chemical Composition

In the very early stages of the development, the composition range for IN718 was mentioned in the SAE AMS 5596A specification (see Table 2.1). Along with the chemical composition specifications, the manufacturing cycle involving specific thermal treatment was studied which led to achieving specific mechanical properties for the

alloy. There exist different specifications for the IN718 and corresponding manufacturing cycle to meet established requirements, Table 2.2 can be referred for SAE AMS 5596A specification for annealing and aging temperatures. The recommended aging method options were as follows:

I) hold for 8 hours at the first aging temperature of 720 °C, furnace cooling at 100 °C/hour to the second aging temperature of 620 °C, hold for 8 hours followed by air cooling.

II) hold for 8 hours at the first aging temperature of 720 °C, furnace cooling to the second aging temperature of 620 °C, hold at the second aging temperature until total elapsed time since first aging is 18 hours.

Table 2.1 Nominal composition (wt%) range of IN718 (SAE AMS 5596A)

Ni	Cr	Fe	Nb	Mo	Ti	Al	C	Co	Cu	Si	Mn
50-55	17-21	~17	5-5.5	2.8-3.3	0.65-1.15	0.4-0.8	0.03-0.1	<1.0	<0.1	<0.35	<0.35

Table 2.2 Annealing and aging temperature for IN718 (SAE AMS 5596A)

Specification ID	Annealing Temperature (°C)	First Aging Temperature (°C)	Second Aging Temperature (°C)
AMS 5596A	955	720	620

2.1.2. Microstructure and phases

The knowledge of the commonly observed microstructure of IN718 and variations in the same due to imparted heat help to understand the rationale behind changes in the mechanical and corrosion properties. The microstructure analysis would

give relevant information about grain size, shape, orientation, grain boundary, defects, and special phases of alloying elements. Devaux et al. (2008) mentioned the microstructure of hot-rolled IN718 cut along the rolling direction after the heat treatment at 1243 K for 1 hour followed by oil quenching. A small grain size of 13 μm with equiaxed morphology and homogeneous δ phase precipitates were found along the grain boundary.

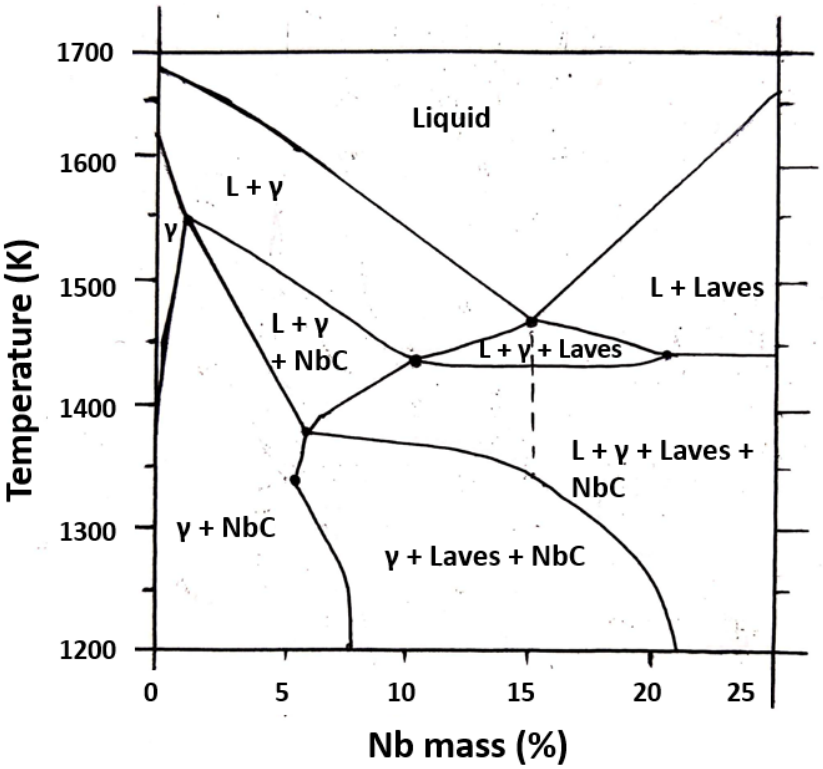

Figure 2.1 Phase diagram of Inconel 718 alloy based on Thermo-Calc software (adapted, Luo et al., 2000)

Luo et al. (2000) showed a phase diagram of IN718 representing liquid (L), gamma (γ, γ', γ"), carbide (NbC), and Laves phases (see Figure 2.1). The precipitates of intermetallic phases occur during preheating processes. The strength of the alloy is influenced by body-centered tetragonal γ"-Ni_3Nb and face-centered cubic Ni_3(Al, Ti) precipitates. Such metastable phases (γ', γ") were recorded above 873 K temperature.

The equilibrium intermetallic phase was claimed to sustain at an elevated temperature when the δ phase (orthorhombic Ni_3Nb, Ni_3Mo) happened entirely. The formation of the interdendritic Laves particle responsible for brittle characteristics can be reduced by increasing the cooling rate of thermal treatment (Ram et al., 2005). Excessive δ phase promotes stress concentration, local distortion, and cracks along grain boundaries under loading, however lack of δ phase leads to reduced high-temperature strength (Gao et al., 2019). Hence, suitable heat treatment and a balanced δ phase proportion can further improve the mechanical properties at high temperatures.

2.1.3. Mechanical properties

Based on specific chemical composition and executed thermal treatment in the preparation of IN718 (annealing or annealing + aging), the tensile strength was reported to vary from 760 MPa to 1400 MPa (Rahim et al., 2015). The corresponding range for 0.2% yield strength was 310 MPa to 1000 MPa. For extreme condition applications, the high-strength alloy can be manufactured following both annealing and aging at optimal conditions. A study was carried out to investigate the mechanical properties variation of rolled IN718 sheets with respect to the rolling direction (Prasad et al., 2017). As shown in Figure 2.2, standard tensile specimens were produced along the rolling direction, at 45°, and 90° (transverse) to the rolling direction. The highest values of UTS and YS were observed for the specimens cut along the rolling direction and the lowest for the specimens cut at 45 ° to the rolling direction. Total elongation was slightly higher for the transverse specimens and lower for the specimens cut along the rolling direction (see Table 2.3) due to the observed random distribution of strengthening precipitates.

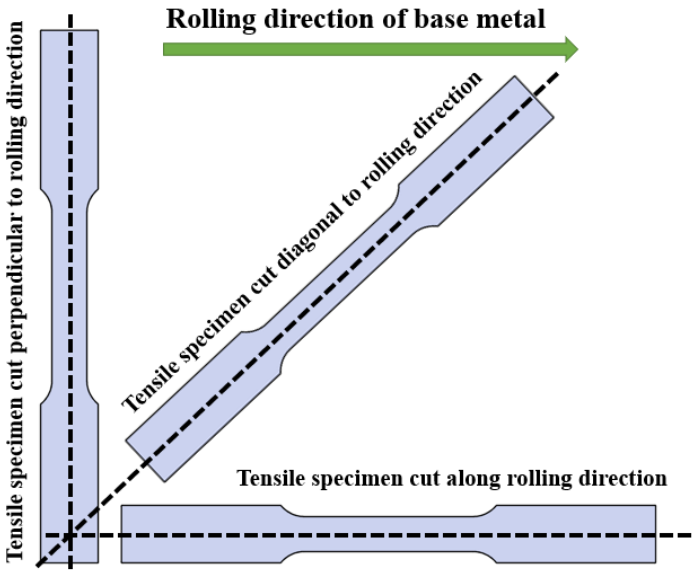

Figure 2.2 Standard ASTM E8M tensile specimen cut at three different orientations to the rolling direction for rolled IN718 (adapted, Prasad et al., 2017)

Table 2.3 Tensile properties at different orientations to the rolling direction for rolled IN718 (Prasad et al., 2017)

Orientation to the rolling direction	Average UTS, S_u (MPa)	Average YS, S_y (MPa)	Average Total elongation (%)
0°	1010	555	39.33
45°	973	519	41.53
90°	991	543	42.25

2.2. Laser Welding of Wrought IN718

Laser Beam Welding of IN718 was investigated by OdabaşI et al. (2010). The 1.3 mm thick IN718 plates with an average grain size of 13 µm were used as base metal conforming to ASTM material standards (ASTM #9.5). Using PRC STS 3000 CO_2 Laser

Beam Welding (LBW) machine, autogenous butt welds were produced along the edge of 200 mm length. The surfaces to be welded were machined with low grinding stresses on a milling machine. After proper cleaning and drying of the specimens, Ar gas was used as shielding gas while performing LBW on the plates. The base metal composition and properties matched the SAE AMS 5596J standards. The details of the process parameters are mentioned in Table 2.4. Four heat inputs (defined below) in the range of 74.5 J/mm to 126.6 J/mm were used. An optical microscope and field emission SEM was used to investigate the microstructure. The microstructure and weld profile were analyzed considering the effect imposed by different process parameters as discussed below.

$$\text{Heat Input} = \frac{\text{Laser Power } (P)}{\text{Welding speed } (S)} \quad (1)$$

Table 2.4 Process parameters of LBW of IN718 plate (OdabaşI et al., 2010)

Sample No #	Laser Power, P (watt)	Welding Speed, S (mm/s)	Parameters specific to machine maker			Heat Input (J/mm)
			Plasma Suppression and Inert Gas Application (liter/min)			
			Plasma	Trail	Back	
1	2900	38.94	35	35	10	74.5
2	2512	31.75				78.8
3	2000	19.89				100.5
4	1500	11.85				126.6

With all the different heat inputs mentioned above, the full penetration through the thickness of 1.3 mm was successfully achieved. The weld profile progression

corresponding to different beam power and welding speed was analyzed. Increasing the heat input from 74.5 J/mm to 126.6 J/mm resulted in a change of weld profile from a wine glass to a stemless wine glass shape with a wider bead at the top. The change in the weld width at different weld depths was also studied (see Figure 2.3) with respect to applied heat input measures. As heat input increased, the widths of weld sections increased. The width at the top increased rapidly compared to the width at the middle and the bottom. Only sample #4 showed the bottom width higher than the width in the middle of the penetration depth.

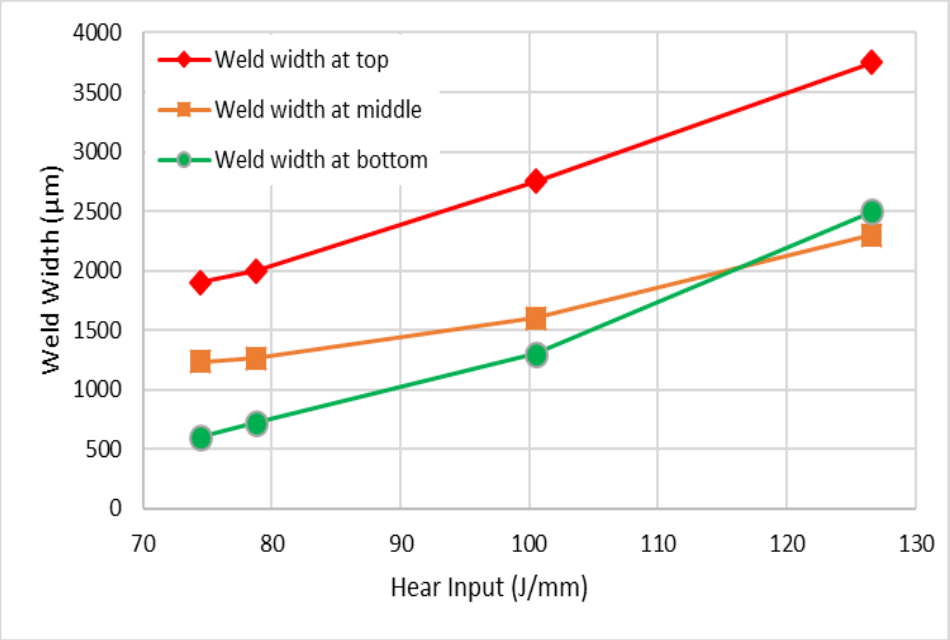

Figure 2.3 Weld width at different depths corresponding to different heat input for LBW of IN718 (adapted, OdabaşI et al., 2010)

Microfissuring (microscopic cracking) in HAZ is a phenomenon resulting based on welding parameters and base metal condition. At high heat input, and consequently,

with a low cooling rate and less steep thermal gradients in HAZ, microfissuring can be avoided. The results showed an increase in dendrite arm spacing with an increase in heat input. An intensive liquation of grain boundaries in HAZ was observed at the highest heat input. No cracks in HAZ were reported even at the lowest heat input.

An attempt was made to investigate laser beam welding of 5 mm-thick rolled IN718 rolled plates (Hong et al., 2008). The study also incorporated two different variants ASTM #4 and ASTM #10 of the base metal to understand the effect of process parameters on weld quality for different grain sizes. The specimens were butt-welded using a CW CO_2 laser welding machine with a power rating of 12 kW. Helium was selected as shielding gas with a flow rate of 15 *l*/min. Different combinations of beam power and welding speed along with resulted potential weld defects and penetration depth status are shown in Figure 2.4. The study incorporated both pre-weld and post-weld heat treatments. There were three different conditions before welding: as-received, 955 °C solution treatment, and 955 °C solution treatment + aging. The four different conditions after welding were as follows: as-welded, direct aging, 955 °C solution treatment + aging, cyclic solution heat treatment (CHT). CHT involved holding a welded specimen at 1000 °C for 3 min, furnace cooling at the rate of 3 °C/min followed by holding at 985 °C for 8 min, and then repeating the cycle for 3 times followed by air cooling to the room temperature. An optical microscope and scanning electron microscope were used to analyze the microstructure of HAZ and fusion zone. A standard tensile test was performed with a standard ASTM E8 sub-size tensile specimen to analyze tensile properties.

Beam Power (kW)	Welding Speed (m/min)						
	1	1.5	2	2.5	3	3.5	4
5	N	N	N	N	PO I	N	SP I
6	CR, SP III	SP III	 III	 III	 II	 I	 I
7	N	N	CR III	SP III	SP III	SP II	PO I
8	N	N	N	N	SP III	SP III	 III
10	N	N	N	N	CR,SP III	N	SP III

N: Unexplored parameter combinations
CR: Crack
SP: Spatter
PO: Porosity

I: Partial penetration
II: Partial/Full penetration
III: Full penetration

Figure 2.4 Process parameters and resulting weld-defects along with full-penetration depth status for LBW of thick rolled IN718 (adapted, Hong et al., 2008)

From the figure above, it was noted that a full depth weld penetration of 5 mm was successfully achieved with a beam power of 6 kW and above with welding speed in the range of 1 m/min-4 m/min. Along with full penetration, defect-free welds were obtained at 6 kW beam power with welding speed of 2 m/min, 2.5 m/min, and at 8 kW beam power with welding speed of 4 m/min. The coarse grain (ASTM #4) base metal showed a higher amount of niobium segregation and microfissuring under the nail head in a transverse section of the weld bead after various heat treatments. The fine grain (ASTM #10) base metal was found with no cracks and Nb segregation was less compared to coarse grain base metal after different heat treatments. The details of tensile results (base metal ASTM #10) are mentioned in Table 2.5 below.

Table 2.5 Tensile test results for LBW of thick rolled IN718 (ASTM #10) at 6 kW beam on the surface, 2.5 m/min welding speed involving STA, CHT as post-weld heat treatments (Hong et al., 2008)

Specimen No.	Pre-weld Heat Treatment	Post-weld Heat Treatment (PWHT)	UTS (MPa)	YS (MPa)	Elongation (%)
1	Base Metal		1380	1068	18
2	As-rolled	STA	1340	1191	3
3	As-rolled	CHT	1417	1265	5
4	Solution	STA	1206	1150	2
5	Solution	CHT	1380	1253	4
6	Solution	Direct Aging	1392	1212	4
7	STA	As-weld	989	769	2
8	STA	Direct Aging	1346	1216	2
9	STA	STA	1286	1179	2

The tensile properties of the as-received welded specimen after cyclic treatment (CHT) was 1417 MPa as compared to 1380 MPa of the base metal. But the same condition compromised the ductility as elongation before fracture reduced by 72% compared to the base metal. The least strength of 989 MPa was observed for samples pretreated by solution treatment followed by aging and no post-weld heat treatment. The results gave important insights on the effect of different process parameters, base metal

grain size, various combinations of heat treatments, and their sequence in the operation on the weld quality.

2.3. Joining of Additively Manufactured IN718

Research on joining additively manufactured IN718 has taken the attention of many in recent years. Efforts have been made to join SLM'ed IN718 by various methods. Raza et al. (2018) conducted the Varestraint test using Gas Tungsten Arc Welding (GTAW) on IN718 samples manufactured by SLM to evaluate cracking susceptibility and microstructure quality in HAZ. The SLM samples (3.4 mm thick, 50 mm × 100 mm) were present in two conditions: as-built and HIP'ed at 1160 °C 105 MPa for 3 hours. The HIP'ed sampled were machined to the thickness of 3.3 mm to remove the oxide layer. The results were then compared against wrought alloy IN718 samples' cracking under a similar test setup. The GTAW was performed along the building direction with a welding current of 70 A, welding speed of 1 mm/s, and an arc length of 2 mm. The plates were bent with a stroke rate of 10 mm/s. The radii of the die mandrel were 40, 60, 100, 200, and 300 mm which induced augmented strains between 0.5% to 4% when accounted for the thickness. Total Crack Length (TCL) which is the length of all visible cracks in FZ and HAZ was measured by a stereomicroscope after manual micro-polishing.

After electrolytically etching the samples with oxalic acid, a weld cross-section of as-SLM'ed welded and top view of SLM'ed HIP'ed welded IN718 plates were observed. After HIP, the grains of HIP'ed IN718 became equiaxed with a larger average grain size of 60 μm. The result indicating TCL with respect to the augmented strain rate

was studied. For wrought and as-built SLM'ed IN718, the threshold strain value to have visible cracks was between 0.8%-1.6%. The saturation strain was observed around 2.6% (after which the TCL remained almost constant) for all three conditions. The wrought alloy and as-built SLM'ed samples showed equal hot crack susceptibility. A higher value of TCL with wider cracks observed for HIP'ed samples was claimed due to larger grains of the same.

Xia et al. (2018) studied the joining of 3D printed IN718 specimens by brazing. An additive manufacturing process for metal (SLM) was used with Ar as protective gas to produce 20 × 20 × 4 mm samples. Laser power and scanning speed for SLW were 350 W and 700 mm/s respectively with a layer thickness of 0.06 mm and a hatch distance of 0.1 mm. Joining of 3D printed samples by brazing was done with a filler metal BrazeLet (BNi-2) foil parallel to the build direction. The foil had a thickness of 60 μm and a size of 20 × 6 mm. Before brazing, the samples were thoroughly cleaned and polished. The filler metal foil was pressed between two samples at 50 kPa in a vacuum chamber with a pressure of 6×10^{-3} Pa. The brazing temperature was set at 1060 °C with a holding time of 30 min. Brazed parts were cut to size 40 × 3 × 4 mm by a linear cutting machine for testing. The etching process was performed with a mixed solution of HCl, CH_3CH_2OH, and $CuCl_2$ (100 mL: 100 mL:5 g) for about 30 seconds. Microhardness, fracture characteristics, and mechanical properties by the shear test were analyzed to inspect the quality of brazing.

The microstructure of the brazed joint was broadly classified into two regions: Isothermally Solidified Zone (ISZ) and Diffusion Affected Zone (DAZ) based on

granular structure and Ni content. The ISZ had hardness values varying in the range of 450-480 HV with 460 HV in the center of the joint. The DAZ had hardness peak values of 490 HV with a higher variability (the lowest hardness value was 390 HV) in the distribution.

Shear tests were conducted on brazed samples at room temperature resulting in a shear strength of 802 MPa which was about 77% of base metal. The results were validated by inspecting fracture morphology. Both dimples (associated with ductile fracture) and river pattern (representing brittle fracture) were present when viewed by SEM. The fracture schematic showed that the fracture initiated in DAZ with intermetallic compounds penetrated through ISZ and ended on the other side of DAZ. It showed a mixed ductile-brittle fracture characteristic.

2.4. Electron Beam Welding of Rolled IN718

Many attempts have been made to study various aspects of EBW of IN718. Huang et al. (2005) identified methods to determine the heat-affected zone (HAZ) in EBW by using specific etching and plotting of microhardness values as a function of distance from the weld center. The specimens were subjected to pre-treatment in two different methods, solution and precipitation treatments, along with as-received conditions. Although the HAZ of width 1.5 mm in solution pre-treated samples could be identified with microhardness measurement, the surrounding HAZ in as-received and precipitation treated samples could not be distinguished from the central weld zone. After metallographic etching, scanning electron microscopy could indicate HAZ that

was within 100 microns for solution and precipitation pre-treated samples. Anodically potentiostatic etching was recommended to identify HAZ in IN718 welds.

Two rolled IN718 plates of dimension 60 mm × 40 mm × 3 mm were welded along the length. Along with as-received plates, some plates were pretreated either by solution or precipitation treatment to produce three different conditions for welds. Pre-treatment process parameters are mentioned in Table 2.6. Two weld passes were exercised; the first with full penetration depth and the second as cosmetic welding with lower heat input. The process parameters for welding are listed in Table 2.7.

Table 2.6 Pretreatment process parameters (Huang et al., 2005)

Pretreatment Type	**Process Parameters**
Solution Treatment	950 °C (1 h) + water quenching
Precipitation Treatment	Solution Treatment + 760 °C (4 h) + water quenching

Table 2.7 EBW welding process parameters for rolled IN718 (Huang et al., 2005)

Welding sequence	**Voltage (kV)**	**Current (mA)**	**Focus Depth from the top surface (mm)**	**Feed (mm/s)**
First Pass	50	100	3.46	36.22
Second Pass	50	60	3.42	25.4

The hardness values for solution pretreated samples measured with an indentation load of 300 and 500 gf was 230 HV on average. Observing hardness values trends, solution pretreated samples showed an indicative drop of 40 HV in hardness value towards the base metal from about 1.5 mm of distance from the weld center. The

same drop in hardness value was smaller going from the weld center to the fusion zone (FZ)/HAZ interface with the base metal. An abrupt change in hardness values was recorded for a precipitation pretreated sample. Hence, the hardness distribution curve serves can be used to measure the width of the HAZ only in the case of solution pre-treated samples. It was claimed to have the presence of γ' and γ" in solution pretreated IN718 samples which led to having a higher hardness in the HAZ. From the study above the importance of the microhardness test to evaluate weld geometry, validation by microscopy, relevant information of IN718 EBW heat input for particular penetration depth can be obtained as a reference.

It was stated by Reddy et al. (2009) that Nb segregation and Laves formation deteriorate the mechanical properties of IN718 welds. It was depicted that an introduction of electron beam oscillations during EBW reduced Nb segregation keeping finer, less continuous Laves phase compared to continuous, network-like morphology. The latter showed a poor response to solution treatment and hence a lower improvement in mechanical properties after welding. The beam oscillations introduced during EBW create smaller weld pools for solidification and hence rapid cooling of the same. Such a phenomenon further helped to have increased fluid flow and reduced thermal gradient in solidifying the weld pool which leads to a better microstructure in the weld fusion zone. A post-weld solution treatment further helped to dissolve (more in a case with elliptical oscillations compared to unoscillated case) Laves formation to improve the mechanical properties of the EBW weld of IN18.

Their experimental IN718 specimens (205 × 105 × 3.1 mm, solution pre-treated) were first welded at heat inputs of 48.4 J/mm in oscillated conditions and then subjected to three different post-weld heat treatments. The EBW setup was equipped to produce different oscillation patterns within frequency up to 2000 Hz in steps of 1 Hz. The least Nb segregation was observed in the range of 15 Hz-20 Hz and hence a frequency of 15 Hz was kept constant in the experiment. Figure 2.5 shows different scanning patterns used to understand their effect on tensile and material properties. For different patterns, the amplitude of beam oscillation was kept constant. The details of the process parameters of EBW with and without oscillations are mentioned in Table 2.8.

Table 2.8 EBW process parameters for rolled IN718 with and without beam oscillation (Reddy et al., 2009)

Parameters	With Oscillations	Without Oscillations
Gun to work distance (mm)	275	275
Accelerating voltage (kV)	55	55
Beam Current (mA)	25 (elliptical), 24 (other)	22
Focus	On the surface	Slightly above the surface
Speed (m/min)	1.5	1.5
Vacuum Level (mbar)	10^{-4} and less	10^{-4} and less
Heat Input (J/mm)	55 (elliptical), 53 (other)	48.4

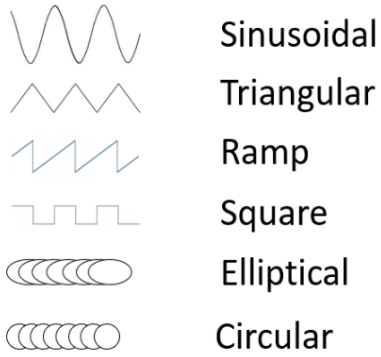

Figure 2.5 Different electron beam oscillation patterns (adapted, Reddy et al., 2009)

After EBW weld, the following two solutionizing treatments were considered: 980 °C per 1-hour air cooling and 1080 °C per 1 h air cooling. After these treatments, a dual aging treatment was performed as follows: 720 °C 8 h furnace cooling and then 620 °C 8 h air cooling. Scanning Electron Microscopy (SEM), electron probe microanalysis, Vickers hardness, and tensile test were performed on the welded samples. A standard tensile test conforming ASTM E8 standards with the INSTRON testing system having the crosshead speed of 2 mm/min was incorporated.

The microstructure analysis showed that solution treatment at 1080 °C resulted in coarse grains and complete dissolution of delta phases compared to fine spheroidal delta phase close to grain boundaries and around carbide particles in the case of solution treatment at 980 °C. Typical fusion zone SEM results concluded the presence of coarser, highly interconnected, and the highest amount of Laves particles in case of unoscillated beam condition compared to other cases of oscillated beam condition. Elliptical oscillations revealed a fusion zone with minimum Laves particles in a dispersed fashion. Table 2.9 below shows vol.% of Laves particle in each case. The elliptical oscillation

pattern was claimed to be the most effective to reduce Nb segregation and Laves formation refining fusion zone microstructure for better mechanical properties of welds.

Table 2.9 Volume fraction of Laves particles in different weld oscillation patterns (Reddy et al., 2009)

Weld Oscillation Type	Volume fraction of Laves (Vol.%)
Unoscillated	12 ± 1.2
Triangular	7 ± 0.1
Circular	5.5 ± 0.1
Elliptical	4 ± 0.8

Vickers hardness test results are mentioned in Table 2.10 below. The 980 °C solution treatment and aging increased the base metal and weld hardness for both unoscillated weld and elliptical weld. The 1080 °C solution treatment significantly increased the hardness of the weld, but the increase was found lesser compared to the 980 °C treatment on the base metal. A wise selection of heat treatment should be based on application requirements. The results of the tensile test performed at room temperature on EBW tensile specimens under the different conditions are listed in Table 2.10 below. The samples treated at 1080 °C fractured through the base metal outside weld. All the results mentioned with different conditions for EBW and heat treatment fractured through the weld zone. Although base metal tensile strengths could not be achieved after welding, the 980 °C solution treatment + aging and direct aging showed

better results with elliptical beam oscillation introduced during EBW of rolled IN718 compared to the unoscillated condition.

Table 2.10 Vickers hardness test results for rolled IN718 (Reddy et al., 2009)

Condition	Base Metal	Unoscillated Weld	Elliptical Weld
As Welded	333	285	325
Direct Aging	521	480	510
980 °C Solution Treatment + Aging (980 °C STA)	522	495	520
1080 ˚C Solution Treatment + Aging (1080 °C STA)	485	530	540

Table 2.11 Tensile properties of EBW samples of rolled IN718 (Reddy et al., 2009)

Condition	Oscillation	Yield Strength (MPa)	UTS (MPa)	Elongation at Fracture (%)
Base Metal	NA	1280	1500	25
EBW + 980 ˚C ST + Aging	Unoscillated	1035	1200	12
	Elliptical	1220	1390	20
EBW + Direct Aging	Unoscillated	1075	1180	10
	Elliptical	1235	1375	16

The effect of heat input in EBW of rolled IN718 sheets on weld geometry, the microstructure of HAZ and fusion zone, and tensile characteristics was studied by Agilan et al. (2014). Weld width at different weld depths, grain boundary liquation

intensity, presence of microfissuring in HAZ, and microstructure of fusion zone were found to be significantly related to heat input of the welding process. Bead on the plate runs with different heat inputs were made across rolling direction on 2 mm-thick cold-rolled IN718 sheets using EO PATON, an EBW machine. The 2 mm-thick rolled sheets were EB welded without pre or post-weld heat treatment. In each trial, different heat inputs were obtained varying only the beam current. Beam voltage and welding speed were kept constant at 60 kV and 30 mm/s respectively. Other process parameters and resulting heat input for corresponding samples are mentioned in Table 2.12.

Table 2.12 EBW process parameters for cold-rolled IN718 sheets (Agilan et al., 2014)

Sample ID	Welding Current, I (mA)	Heat Input (J/mm)
S-1	18	36
S-2	36	72
S-3	56	112
S-4	72	144
S-5	90	180

Weld geometry, observed in the transverse section of the weld bead, showed variation in the width and shape of the weld zone. The width of the weld was measured at the top, middle, and bottom locations. Moving towards higher heat input (from sample identification S-1 to S-5), the width of the weld at the top increased as the higher beam current melted more material having more energy. As shown in Figure 2.6, only S-1 and

S-5 samples had a higher weld width in the middle of the weld compared to the bottom of the weld. All other samples (S-2, S-3, S-4) showed opposite results.

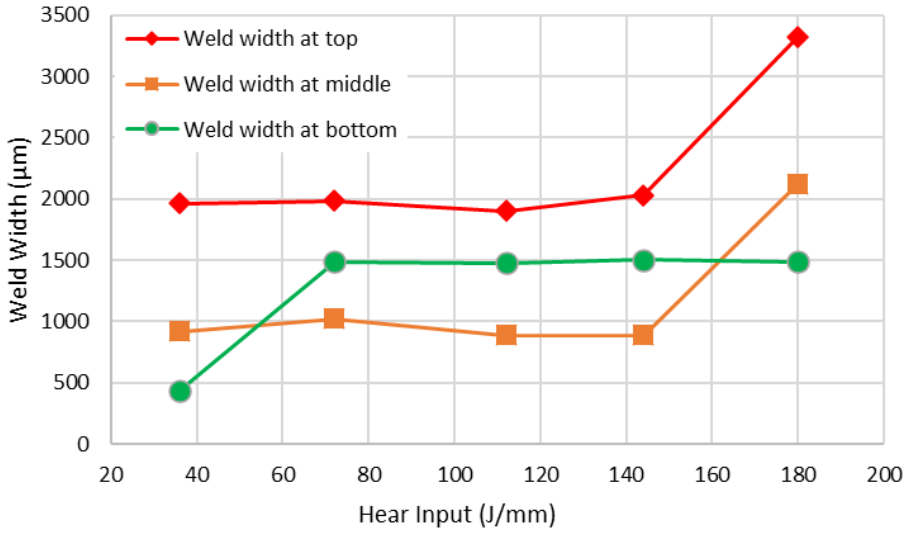

Figure 2.6 Weld width at different weld depths for EBW of cold-rolled IN718 (adapted, Agilan et al., 2014)

Some of the weld quality aspects such as microstructure and micro-segregation of alloying elements within the fusion zone were found to be affected by the heat input amount as it is a time-dependent phenomenon and the cooling rate is related to the heat input. Table 2.13 shows different cooling rates at applied heat input levels. At a higher heat input, a lower cooling rate was measured with a higher interdendritic distance. It was discussed slow cooling can further promote unfavorable segregation in the fusion zone. At the same time, it was reported that at the lowest heat input with the highest cooling rate (sample S-1), microfissuring was observed in HAZ while other samples were free from any cracks in HAZ. Although the change in the segregation amount with

respect to heat input was not significant; Nb, Ti, and Mo segregations were towards interdendritic regions whereas most of Cr, Fe, Al segregated into dendritic core regions.

Table 2.13 Measured interdendritic distance and the cooling rate at different heat input for EBW of rolled IN718 (Agilan et al., 2014)

Sample ID	S-1	S-2	S-3	S-4	S-5
Interdendritic Spacing (µm)	3.5	3.8	4.8	5.1	6.0
Cooling Rate (K/s)	10300	8386	4676	4019	2677

The heat input influenced weld geometry, microstructure, and chemical composition of the weld. Variation in lower values of heat inputs had minimal effect on the mechanical properties of the weld. The best mechanical properties of welded specimens (average UTS of 884 MPa and 0.2% yield strength of 489 MPa) were obtained when subjected to the lowest heat input of 36 J/mm. The details of the mechanical properties of EBW samples S-1 and S-5 are listed in Table 2.14.

Table 2.14 Mechanical properties of EBW of rolled IN718 (Agilan et al., 2014)

Sample ID	Heat Input (J/mm)	Average UTS, S_u (MPa)	Average 0.2% YS, S_y (MPa)	Elongation, ε_f (%)
S-1	36	884	489	37
S-2	180	874	479	39

Similarly, Sharma et al. (2017) experimented with the EBW on 3 mm thick uniformly cold-rolled and solutionizing heat-treated (980 °C for 1 h followed by water quenching) IN718 plates. The beads on the plate were formed using the process parameters mentioned in Table 2.15 with sample labeling. Three process parameters: accelerating voltage, beam current and welding speed were varied to produce three different combinations all with the same heat input of 120 J/mm. The transverse sections of the beads were cut and aged at 720 °C for 8 hours followed by cooling at 50 °C/h to 620 °C, holding at 620 °C for 8 hours, and then were quenched using water. The quenched samples were polished and etched with a concentrated acid mixture of HNO_3, HCl, and HF in the ratio of 2:2:1. The microstructure, weld geometry, and chemical composition of EBW samples were analyzed by optical microscopy, field emission scanning electron microscopy, and X-Ray Diffraction (XRD) techniques.

Table 2.15 Process parameters for EBW of cold-rolled IN718 plates (Sharma et al., 2017)

Sample No.	Accelerating Voltage, V (kV)	Current, I (mA)	Weld Speed, S (mm/s)	Heat Input (J/mm)
A	As-received Inconel 718 base metal			
B	50	64	26.67	120
C	60	60	30	120
D	70	57.14	33.33	120

Fusion zone microstructure, weld section width, and shape were analyzed by optical microscope. Sample C showed an optimum weld profile with a better weld

penetration depth to width ratio with no defects in the microstructure of the fusion zone when observed at low magnification. A very narrow HAZ was observed under high magnification separating columnar grains of fusion zone and large grains of base metal in all samples. A better trade-off among voltage, weld speed, and beam current was observed (sample C). At the same heat input; increasing accelerating voltage, weld speed and, decreasing beam current widened the weld zone.

X-ray diffracted pattern showed similar peak positions for all samples, but the magnitude of peaks and hence the quantity of phases present differed in each sample. Along with austenitic γ – Ni, precipitated γ' – $Ni_3(AlTi)$, and major hardening phase γ"– Ni_3Nb; Laves and δ precipitates were commonly found.

Gao et al. (2011) attempted EBW of hot rolled thick IN718 plates (100 × 120 × 12 mm thick), using two weld passes to study the microstructure and mechanical properties variation at different weld depths. The process parameters of the respective EBW passes are mentioned in Table 2.16. Electron beam welding equipment KL110 was used to produce butt weld along the length of the plates. A special fixture was used for the assembly alignments keeping a close distance of less than 0.1 mm between the surfaces of the plates before welding. After EBW, welded plates and thick base metal plates were subjected to solution treatment followed by dual aging processes (920 °C for 1 hour with air cooling for solution treatment, 720 °C for 8 hours followed by cooling at 50 °C/h for the first aging process and 620 °C for 8 hours followed by air cooling for the second aging process). The welded plates were cut into slices perpendicular to the welding direction. The metallographic specimen was corroded by an

acid mixture of 2 ml HF, 20 ml HNO_3, 100 ml HCl and 76 ml of H_2O after grinding and polishing. A microscope of LEXT-OLS3000 was used to examine the microstructure of transverse sections. From each welded and un-welded plate, slices at different sections (top, middle, and bottom) were cut to produce tensile specimens to examine tensile characteristics at 650 °C by Instron5500R testing system.

Table 2.16 Process parameters for EBW of hot-rolled thick IN718 plates (Gao et al., 2011)

Welding sequence	Voltage (kV)	Focus Current (mA)	Beam Current (mA)	Feed (mm/s)	Heat Input (J/mm)
First Pass (full penetration)	60	700	120	11	654
Second Pass (cosmetic penetration)	60	700	30	11	164

The results from the tensile test carried at an elevated temperature of typical IN718 usage are shown in Figure 2.7. Mechanical properties of the welded tensile specimen as a whole and tensile specimens from different slices along the weld depth were compared against the base metal properties. The tensile strength of the welded specimen as a whole was above 1100 MPa close to that of the strength of the top section. This value was about 90% of the base metal strength of 1240 MPa. The tensile strength improved going from the top to the bottom position of the weld section. The maximum

value of the tensile strength (close to 1200 MPa) was reported at the bottom section. The yield strength characteristics also presented a similar trend to that of the tensile strength, but only about 80% of the yield strength of base metal was shown by the welded specimen as a whole. It was noticed that the strength properties of the welded specimen as a whole were closely related to the lowest properties at the top. However, elongation of the whole join observed to be 80% of the base metal, was significantly higher than that of the lowest elongation at the top. It was claimed that the middle and bottom sections with better mechanical properties helped the whole join to attain higher elongation. The results of this study showed the feasibility of having two weld passes and corresponding elevated temperature mechanical properties at different weld depths.

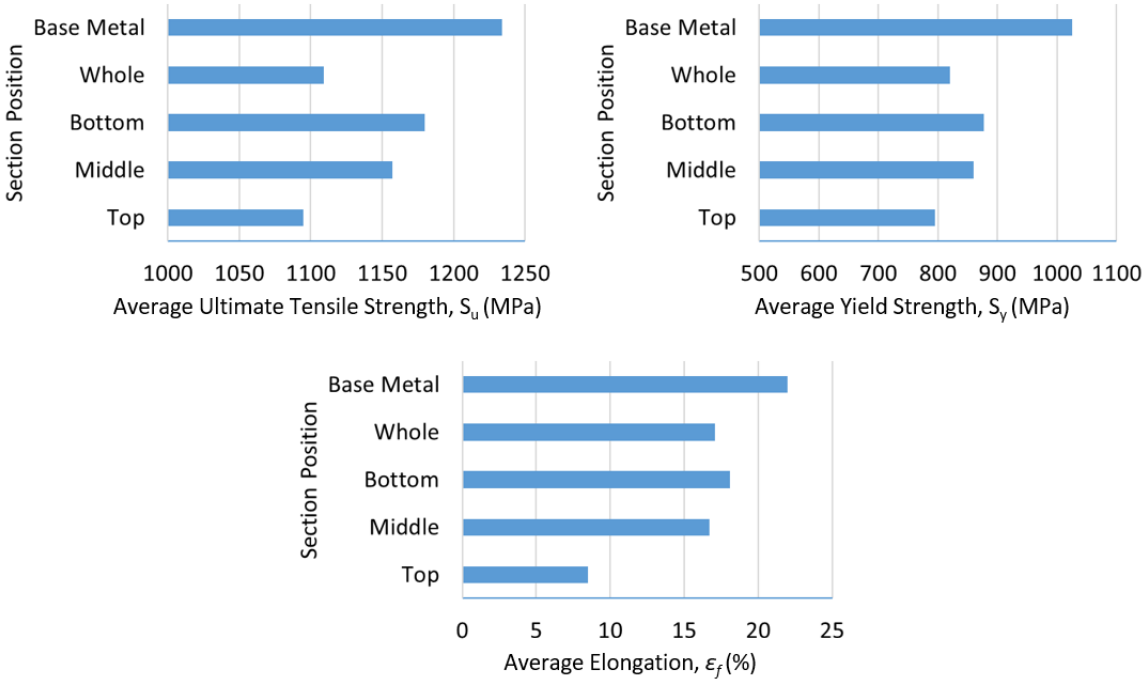

Figure 2.7 High temperature (650 ˚C) mechanical properties of IN718 weld sections, whole and base metal specimens (adapted, Gao et al., 2011)

The microstructure of a thick EBW after the heat treatment as mentioned above with a full penetration depth of 12 mm in a transverse section to the welding direction was inspected. The analysis was carried by dividing the section into three planes: top, middle, and bottom. The weld-center on the surface was exposed to both a full penetration pass and cosmetic pass. As the cosmetic pass was performed on the join weld and the location is close to the surface, the cooling rate was higher. This resulted in the recrystallization of dendrites crystals at the same location. At the HAZ on the top surface location, the grain size was grown compared with the primitive grains. In the middle section, at the weld center, the number of dendrites became lesser and the columnar grains became larger. Similarly, at HAZ in the middle plane, grains grew in size from the center but were smaller compared to the top plane. The reason for the typical microstructure in the middle plane was due to a slower cooling rate compared to the top plane. The recrystallization dendrites were observed (same as the top plane) in the bottom plane as the cooling is much faster in the bottom plane compared to the middle plane. The HAZ grains did not grow as expected at the bottom location because of the limited effect of the heat at the bottom.

The microhardness analysis was carried out at three planes: top, middle, and bottom. In each plane, the spacing between indentations was kept 0.5 mm. The indentation load was 1000 gf and dwell time was set 15 s on HVS-1000Z. In general, the hardness values in the fusion zone were lower compared to those in HAZ and base metal. In the weld fusion zone, the microhardness values were higher in the middle plane compared to those in other planes. The distribution of hardness in HAZ and

base metal among the three planes were not uniform. Although the hardness is related to the grain size, a lower hardness in the fusion zone was claimed due to higher inter-crystalline precipitates (δ – phase) and lower intragranular precipitated phases (γ' – phase and γ" – phase).

The effect of base metal conditions or pre-heating of the base metal on the weld geometry and chemical composition was studied by Mei et al. (2016). The study also analyzed the microhardness of EBW samples and the effect of welding speed on microstructure and ensuing cracks. As-received 1.6 mm thick IN718 plate was cut to dimension 165 mm × 26 mm by wire-cut Electrical Discharge Machining (EDM). These plates were subjected to different heat treatments before welding and given the corresponding base metal label as mentioned in Table 2.17. Three welding speeds were used only on sample B and all other parameters were kept constant (accelerating voltage = 125 kV, beam current = 65 mA, high vacuum). To understand the effect of welding speed and base metal condition on weld-cracking susceptibility, a Varestraint weldability test was performed for each parameter combination. It is an effective method to evaluate the hot-ductility, weldability of nickel alloys in terms of resistance to hot cracking. The test setup incorporates a standard welding procedure with radius blocks and bending bars to produce desired strain. The details of the experiment matrix are listed in Table 2.17. The transverse sections of welded specimens were mounted with epoxy in a 25 mm diameter cylinder. After mechanical grinding and polishing, the samples were etched using a mixture of 5 g $CuCl_2$, 100 ml, HCl, and 100 ml C_2H_5OH (Kalling's reagent) to reveal the microstructure. Vickers microhardness test was carried out with a diamond

pyramid indenter, 200 gf of load, and 10 s of dwell time. OLYMPUS optical microscope for microstructure and weld profile evaluation, scanning electron microscope with energy dispersive spectroscopy system for micro-cracks and quantitative element analysis, X-ray diffraction analysis for phase identification as well as microhardness tests were used for a detailed inspection of welded specimens.

Table 2.17 Pre-welding heat treatment and base metal labels (Mei et al., 2016)

Base Metal Label	Pre-welding Heat Treatment
A	1100 °C/1 h, air-cooled
B	1040 °C/1 h, air-cooled
C	950 °C/1 h, air-cooled
D	untreated

The effect of base metal condition (pre-weld treatment) and welding speed on the weld geometry was inspected. Weld geometry was mainly characterized by the shape and penetration depth to width ratio in the transverse section of the weld bead. Going from base metal condition D to A (untreated to increasing temperature pre-weld treatments), changed the weld shape from a stemless wine glass shape to a nail head shape with a narrower bead and higher penetration depth. The weld section profile sketches are schematically attached in Figure 2.8. The change in the matrix and chemical composition of the base metal led to having different melting temperatures for different conditioned base metals. The penetration depth to width ratio changed from 0.72 to 1.58 moving from condition D to condition A. The different welding speeds tried on base metal condition B (N3, N5, N6) were very close and hence the difference in the

penetration depth to width ratio was not substantial but the same increased by a small amount for the slowest welding speed (N6) as expected.

Table 2.18 Experiment matrix for EBW of rolled IN718 plate (Mei et al., 2016)

Specimen ID	Base Metal Label	Welding Speed S, (mm/s)	Condition	Heat Input (J/mm)
N1	D	21.17	Normal welding	384
N2	C	21.17		384
N3	B	21.17		384
N4	A	21.17		384
N5	B	20.12		404
N6	B	19.05		427
N7	D	21.17	Varestraint welding	384
N8	C	21.17		384
N9	B	21.17		384
N10	A	21.17		384
N11	B	20.12		404
N12	B	19.05		427

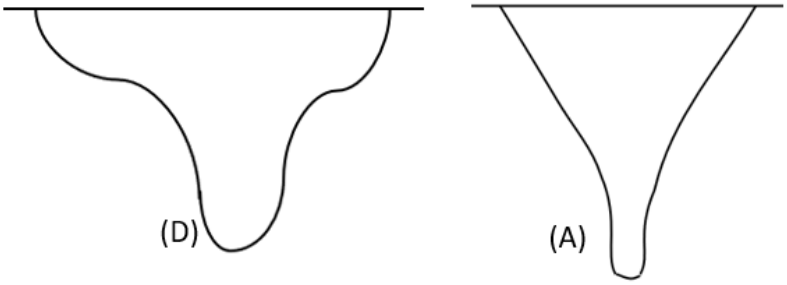

Figure 2.8 Schematic sketch of weld section profile (D) base metal condition D showing stemless wine glass shape (A) base metal condition A showing nail head shape (not to the scale, adapted, Mei et al., 2016)

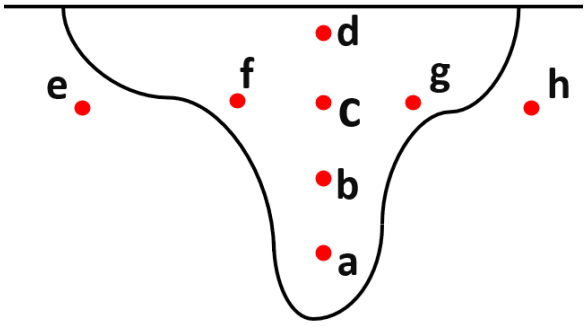

Figure 2.9 Schematic representation of microhardness measurement points on a typical transverse section of EBW sample (adapted, Mei et al., 2016)

The initial hardness study was carried out on discrete points on the transverse section as shown in Figure 2.9. The lowest hardness was recorded on point c due to the presence of more large size Laves compared to other regions. It was accepted that Laves used up Nb from strengthening γ'and γ" phases in turn allowing more plastic deformation on point c. Points a, f, and g were found free from Laves. Other regions along the weld line and top surface/HAZ showed higher hardness values compared to point c (see Table 2.19).

Table 2.19 Measured microhardness at different points (Mei et al., 2016)

Point ID	a	b	c	d	e	f	g	h
Hardness (HV)	282.3	247.3	230.6	267.9	242.5	256.2	258.7	246.1

An attempt was also made to understand the effect of base metal pre-weld heat treatment and welding speed on hardness values. On the same weld depth, the hardness of different samples was measured across the weld bead. The hardness distribution within the fusion zone was identical irrespective of the base metal condition. The hardness values deflected in a similar fashion within the fusion zone reaching the minimum point at the weld centerline. The base metal hardness values were different because of the grain size produced after different pre-weld heat treatment. On base metal condition B, the effect of different welding speeds was visible within the fusion zone – hardness increased as the welding speed increased from 19.05 mm/s to 21.17 mm/s. The variation in the hardness was mainly due to the microstructure and observed segregation within the weld. It was observed that the area fraction of Laves formation did not relate directly to that base metal condition but it increased with a decrease in the welding speed (see Figure 2.10). As the welding speed decreased, the molten metal cooling rate decreased giving more time for the segregation to happen within the fusion zone. This reflected both on hardness values and percentage Laves formation as discussed above.

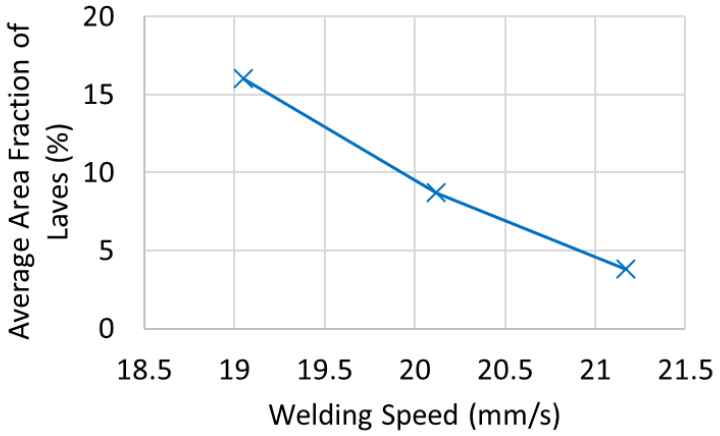

Figure 2.10 Area fraction of Laves with respect welding speed of EBW for rolled IN718 base metal condition B (adapted, Mei et al., 2016)

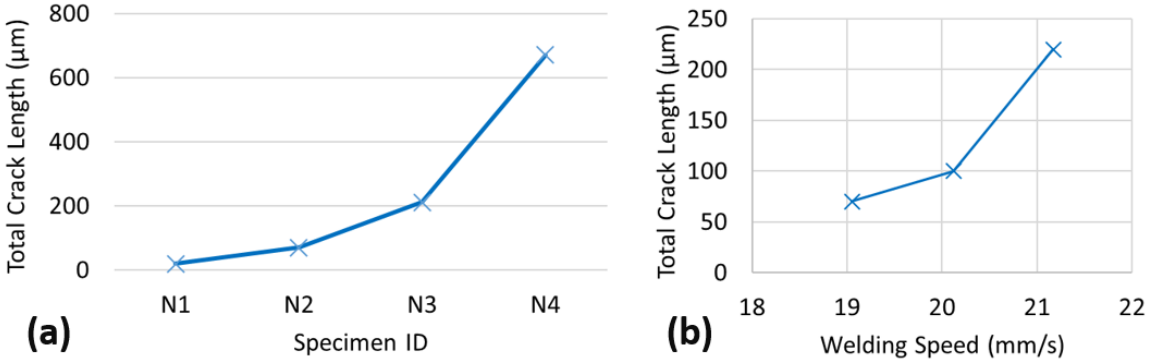

Figure 2.11 HAZ weld-crack susceptibility analysis with respect to (a) base metal condition (b) welding speed (adapted, Mei et al., 2016)

After the Varestraint test, SEM along with image analysis software was used to quantify average crack length and total crack length. Statistical analysis of the same was then used as a criterion for weld crack susceptibility around HAZ at the different base metal conditions and welding speed. At least 8 cracks were considered to compute average crack length. The average crack length changed from 20 μm to 38 μm whereas the total crack length increased significantly from 20 μm to 650 μm going from base

metal condition D to A (towards increasing grain size of base metal) as shown in Figure 2.11. That concluded moving from untreated base metal condition to high-temperature pre-weld heat-treated base metal condition increases the crack susceptibility of HAZ as far as EBW of rolled IN718 was concerned. The total crack length measured in HAZ increased considerably as the welding speed was increased from 19.05 mm/s to 21.17 mm/s due to the fact of having higher maximum thermal stresses and rate of extension exerted on the fluid film at a higher welding speed.

2.5. Formation of Keyhole Root Defects in Electron Beam Welding

EBW process can suffice the need to produce deep penetration in thick metal specimens but it is also prone to produce keyhole void (root-void) defects. The phenomenon that may lead to the formation of such defects related to EBW was studied (Liu & He, 2016). A 20 mm thick 2219 aluminum alloy plate was exposed to a controlled electron beam in a vacuum of 10^{-2} Pa with three combinations of parameters as mentioned in Table 2.20. The working distance for the EBW process was kept at 100 mm.

Table 2.20 Process parameters for EBW of thick aluminum alloy 2219 (Liu & He, 2016)

Case #	Accelerating Voltage (kV)	Focusing Current (mA)	Beam Current (mA)
1	60	730	65
2	60	730	45
3	60	730	35

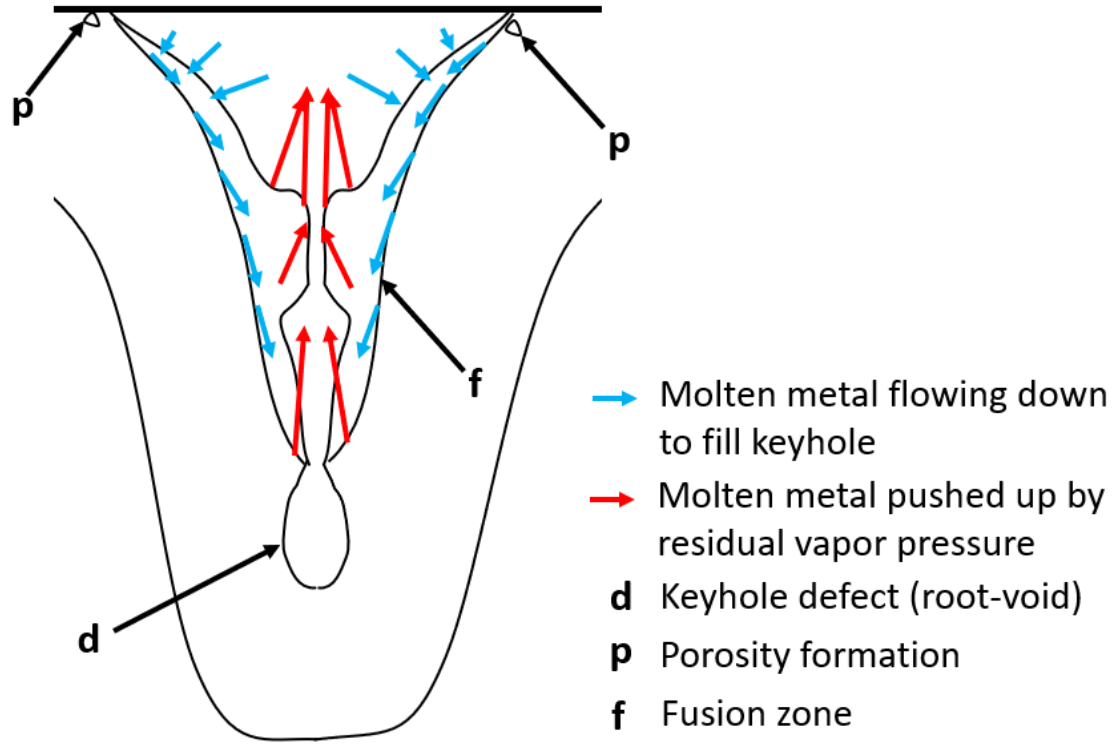

Figure 2.12 Mechanism for the formation of keyhole root-void defects and potential porosity in the nail head region for deep and narrow EBW (adapted, Liu & He, 2016)

The progression of weld geometry was analyzed by a microscope. As the beam current increased, the weld width and weld depth increased as expected. A keyhole formation and backfilling led to the formation of a nail-head-shaped fusion zone. Only case #1 with the highest beam current of 65 mA showed the keyhole root defect where a small freezing product was produced by residual vapor condensation once local exposure to beam heat from the top was cut off (ref. Figure 2.12). The spiking defects were claimed to be more prone in EBW where deep partial penetrations were achieved. After heat application and formation of the keyhole shape of the molten pool; surface tension, Marangoni shear stress (induced due to mass transfer of molten metal resulted by

differential surface tension and thermal gradient), and hydrostatic pressure pushed liquid metal inward and downward (blue arrows) to fill the keyhole. As time lapsed, due to having a deep penetration of about 11.24 mm in case #1, the vapor plumes took a longer time to escape single-channel and forced molten metal upwards (red arrows). A longer and thinner liquid sidewall, insufficient for liquid filling close to the weld-bottom, was formed which led to the formation of residual vapor-cavity defects at the bottom. A similar result was modeled numerically at time = 156 ms (local beam cut-off time = 150 ms) to explain the details of underlaying time and heat-dependent stresses as well as fluid flow. A crater found in the nail-head region was due to the falling of backfilled liquid metal from the top. This backfilling from the top might lead to the formation of porosity in the nail head region of the keyhole for very deep and narrow electron beam welds.

2.6. Special Post-weld Treatment

The research on EBW of rolled IN718 mentioned different approaches for the quality welds and the feasibility of the same in a practical sense. These approaches included pre-weld heat treatments such as solution and precipitation treatments, improvements in the process such as the inclusion of oscillations during welding, and post-weld heat treatments such as solutionizing followed by dual aging processes. The results showed considerable improvement in weld quality and mechanical properties. One of the studies inspected a comparison of base metal and weld properties after heat treatment. Ram et al. (2005) obtained improved mechanical properties of EBW weld of

IN718 after specific post-weld heat treatments; however, the results were still inferior compared to those of the base metal. The results of their test are shown in Table 2.21.

Table 2.21 Mechanical test results (Ram et al., 2005)

Sample Condition	Tensile strength at 650°C (MPa)	Hardness (HV)
Base Metal	1164	505
Dual Aging (8 h at 720 °C + furnace cooling to 620 °C + air cooling for 8 h)	1100	452
Solution heat-treated (20 min at 920 °C + air cooling to 25 °C + dual aging)	1125	478

A unique mechanical post-weld treatment known as Friction Stir Welding (FSW) was investigated by Song et al. (2013). FSW was performed on overlap-welded IN718 (to a heat-resistant steel plate) before post-weld heat treatment as an additional process to improve the mechanical properties. An overlap welded IN718 alloy on a heat-resistant steel plate was given surface modification treatment by FSW. A 1.8 mm long WC-Co tool with 15 mm shoulder diameter and 6 mm probe diameter was tilted at 3° forward from the vertical for the process. With Ar gas, FSW was performed at a tool rotation speed of 200 rpm, a downward force of 39.2 kN, and a feed rate of 1.67 mm/s. The microhardness and tensile tests were carried out after FSW and FSW + post-FSW heat treatment to understand the effectiveness of both processes. The tensile specimens were cut in the transverse section to the feed direction of the FSW tool.

The microstructure after the FSW process showed a uniform defect-free grain structure with refinement in a transverse section. The Vickers microhardness increased by >20% in the stir zone (260-300 HV) after FSW compared to the base metal microhardness values (210-240 HV). The prescribed post-FSW heat treatment substantially increased the microhardness in the stir zone by >70% compared to the base metal values and by >65% when compared to the results after just the FSW process. Hence, it was concluded that heat treatment can be used to improve microhardness significantly when introduced after the FSW process.

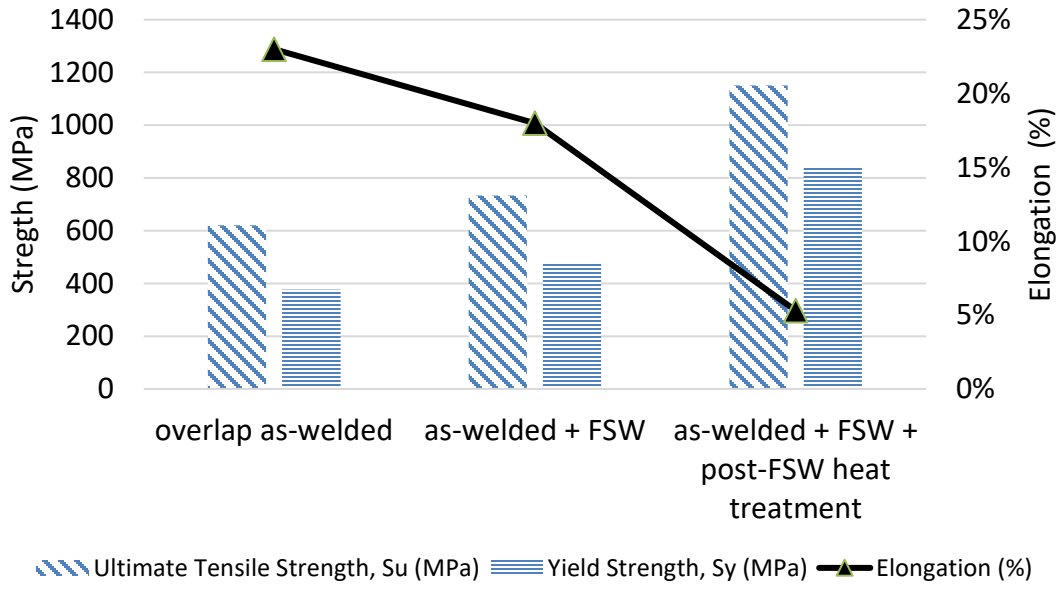

Figure 2.13 Mechanical properties of as-welded, as-welded+FSW, and as-welded+FSW+post-FSW heat-treated IN718 weld (Song et al., 2013)

The tensile test results were compared for three conditions: overlap as-welded, as-welded + FSW, and as-welded + FSW + post-FSW heat treatment. The tensile strength and yield strength increased by 18% and 26% compared to the overlap welded

sample, but the elongation decreased to 18% after FSW. After heat treatment, the strength values increased considerably, but at the same time, a significant decrease in elongation was observed. The results are shown in Figure 2.13.

2.7. Summary and Future Direction

Most of the literature focuses on the understanding of weld microstructure, microhardness, effects of welding parameters on Nb segregation, Laves formation, mechanical properties, microfissuring, and ensuing defects in weld and base metal. Considering the favorable consequences of different variables, it may be inferred that there exists a compromise in the selection of the process parameters to mitigate possible defects and achieve quality welds. Little has been studied on the mechanical properties of EBW of thick IN718 plates using a single weld pass. Variation in more than one process parameter is also worth studying to capture the effects over the feasible design spectrum of EBW. Although various methods such as GTAW and brazing have been explored for 3D printed IN718 parts, EBW has not yet been fully explored for this purpose. This research focuses on establishing references for EBW of IN718 using hot-rolled material and would provide benchmarks for a study on EBW of SLM'ed IN718 to be conducted in parallel by the author and another member of the research group.

3. EXPERIMENTS

3.1. Proposed Workflow and Procedures

The experiment was carried out in three major phases each included a series of activities in an organized order.

1. In the very first phase of the research, a full factorial Design of Experiments (DOE) was constructed. Beam Current and Welding Speed were treated as two parameters each having three levels.
2. The second phase included the production of different test specimens. To accomplish the second phase, a planned material procurement followed by process design for EBW and specimens' preparation methods were exercised. Successful preparation required cutting weld coupons by Electrical Discharge Machining (EDM), labeling the same, and systematic assembly of coupons with spacers. Test specimens included hardness coupons and standard tensile samples.
3. These specimens were produced to carry out various tests in the lab namely optical microscopy, microhardness test, tensile test, fractography, and energy dispersive spectroscopy. These tests were encompassed in the third phase that led to characterize important mechanical and material properties to ensure the reliability of the EBW process and quality of welds for IN718. In order to

---

1. The content of this section has been published under the reference – "Patel, V., Sali, A., Hyder, J., Corliss, M., Hyder, D., & Hung, W. (2020). Electron Beam Welding of Inconel 718 Electron Beam Welding of Inconel 718. *Procedia Manufacturing*, *48*(2019), 428–435. https://doi.org/10.1016/j.promfg.2020.05.065"
2. The authors retain full rights to the content for the academic dissertation. The details can be found: https://www.elsevier.com/about/policies/copyright#Author-rights

understand the effect of specific heat treatment on the hardness, after completing the first run of the microhardness test on all samples, a second run of the same test was performed on the heat-treated hardness coupons. Figure 3.1 illustrates a flow diagram of each phase of research with procedure details in each phase.

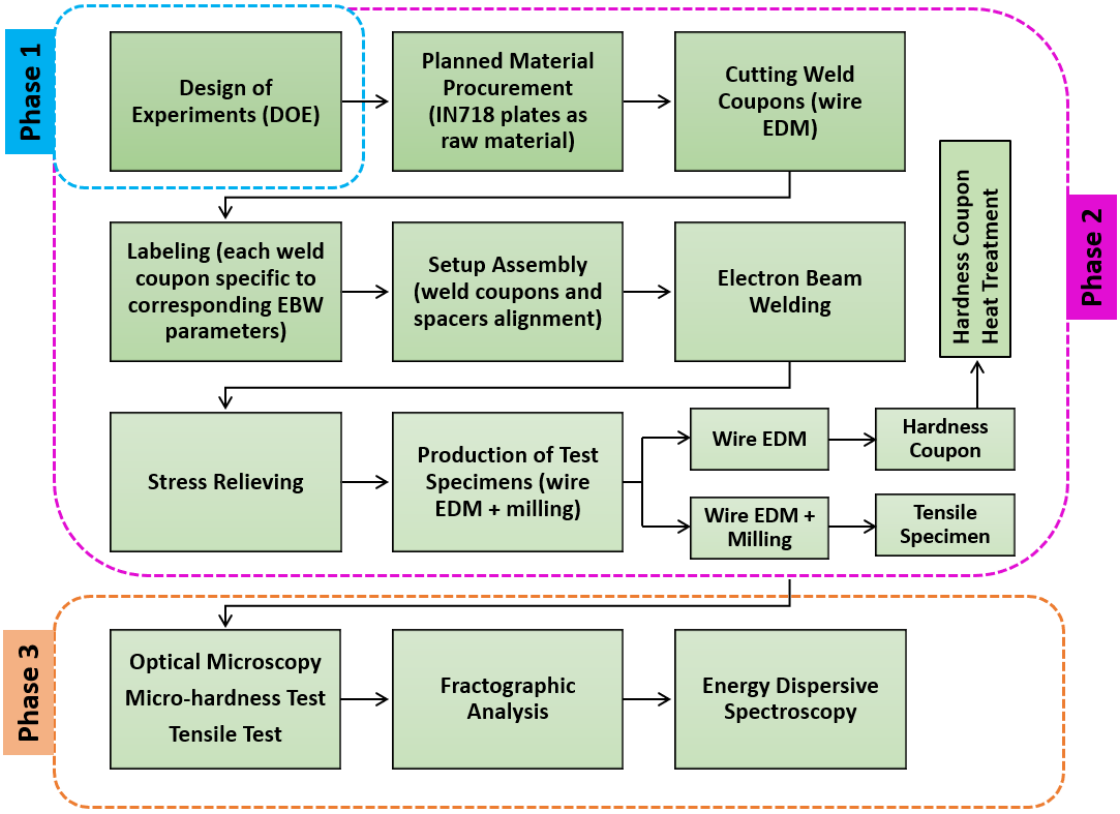

Figure 3.1 Flow diagram of experimental phases

3.2. Equipment and Software

The following equipment, machines, and/or tools were used to perform the tasks involved in the research activity:

1. Sciaky EBW System
2. Wire-EDM Machine
3. Wen Electric Engraver

4. Buehler Handimet grinder 1470-AB
5. Dremel Portable Hand Polisher 4300
6. Struers Metason 200 ultrasonic cleaner
7. MTS 810 Material Testing System
8. Olympus STM6 optical microscope
9. Wilson VH1102 Vickers Hardness Tester
10. Vega 3 Tescan Scanning Electron Microscope
11. Oxford Instruments x-act Energy Dispersive Spectroscopy system

The following software and/or computer program were used to perform the tasks involved in the research activity:

1. Olympus cellSens
2. Adobe Photoshop
3. ImageJ
4. MATLAB R2019a
5. MTS Station Manager
6. Aztec EDS software
7. VegaTC software

3.3. Design of Experiment (DOE)

To achieve the primary purpose of understanding the effect of various process parameters of EBW on weld quality (defects, penetration depth) and mechanical properties (hardness, tensile strength, ductility), it is important to construct the DOE. The objective is to check the feasibility of selected process parameters for desired weld

quality and properties in the range of 180 J/mm to 300 J/mm of heat input. From the literature survey and past EBW experiments, the above-mentioned approximate range of heat input from EBW was identified to achieve the weld penetration of at least 9 mm.

3.3.1. DOE Aspects

To suitably construct a DOE, it is required to have the following DOE aspects defined.

- Type of DOE
- Selection of variables and constants
- Selection of the number of levels for each variable, repetition for each combination
- Range and magnitude of each level for variables

3.3.2. EBW Process Parameters and DOE Characterization

For the EBW process, there are different process parameters that can be controlled such as:

1. Electron Beam Current
2. Electron Beam Speed
3. Electron Beam Voltage
4. Electron Beam Focal Plane Distance from the Gun
5. Focusing Current
6. Vacuum Pressure and Gas Used

$$\text{Heat Input } \left(\frac{\text{J}}{\text{mm}}\right) = \frac{\text{Beam Current (mA)} \times \text{Beam voltage (kV)}}{\text{Welding speed } \left(\frac{\text{mm}}{\text{s}}\right)} \quad (2)$$

From the above-mentioned EBW process parameters, beam current and welding speed were chosen as variables each having three levels. Heat input can be obtained from equation (1) and hence is a dependent variable in this case. All other process parameters were kept constant. With these settings, a full factorial DOE was suggested to cover the proposed design space entirely which would ultimately produce 9 identical combinations of beam current and welding speed and hence 9 identical heat input. One repetition was suggested for each heat input leading to a total of 18 iterations from the experiment.

Table 3.1 Rudimentary DOE for EBW of rolled IN718

Coupon Label	Welding Speed (mm/min)	Beam Current (mA)	Heat Input (J/mm)
A1	Low	High	Dependent on Welding Speed and Beam Current (Target range = 180 J/mm to 300 J/mm)
A2	Low	Intermediate	
A3	Low	Low	
A4	Intermediate	High	
A5	Intermediate	Intermediate	
A6	Intermediate	Low	
A7	High	High	
A8	High	Intermediate	
A9	High	Low	

Table 3.1 describes a preliminary outline of the DOE frame which was used to quantify each level of individual process parameters in a later stage to cover the desired range of dependent variable - Heat Input. The goal is to achieve heat input levels within the range of 180 J/mm to 300 J/mm to achieve full weld penetration when standard tensile specimens of thickness 6 mm are produced.

3.3.3. Numerical Optimization for Level Selection with Active Constraints

It was important to understand the design space constraints and interrelation between design variables which controls the distribution of dependent. As shown in Figure 3.2, maximum heat input was achieved at the highest beam current and the lowest welding speed and vice versa. Figure 3.3 shows uniform and cluster distribution of resulting heat input combinations observed at different maximum beam current levels with a constant range.

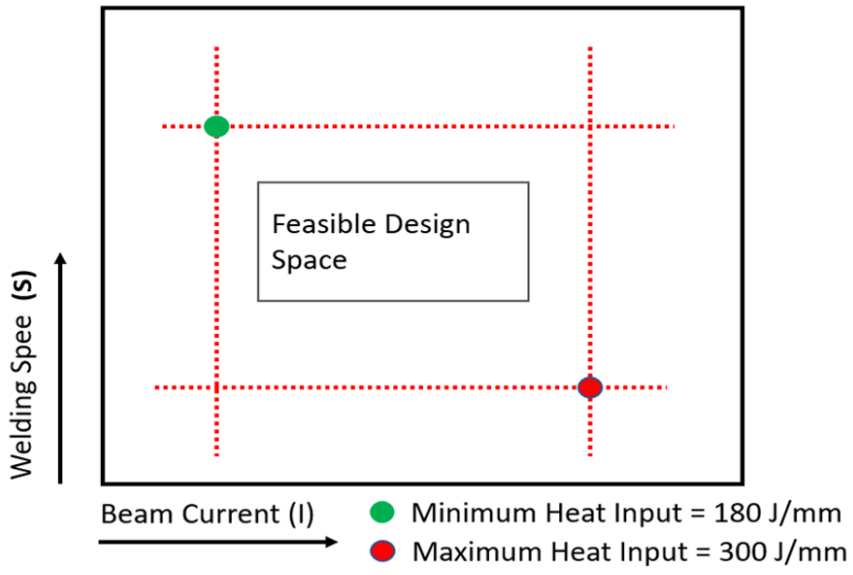

Figure 3.2 Experiment design space feasibility from variables

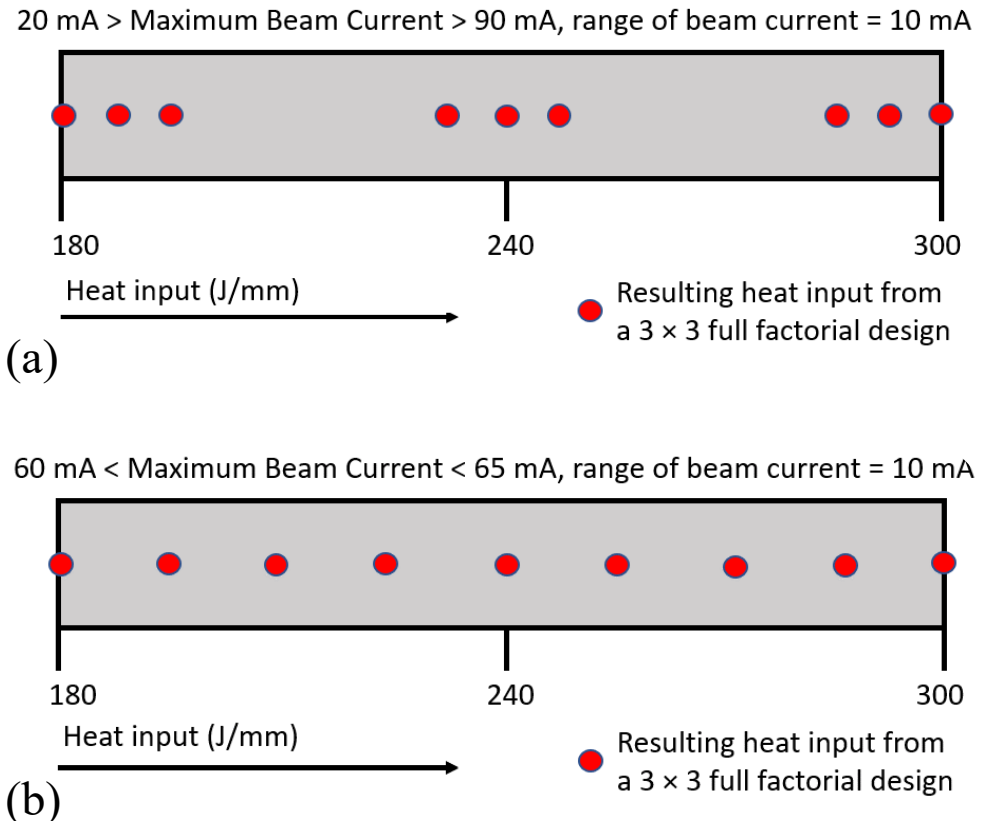

Figure 3.3 (a) Cluster distribution and (b) uniform distribution of heat input levels in design space

Other than achieving the requirement of the desired heat input range, conforming parameters within the capacity of the EBW machine and optimization of uniform distribution of heat input in the desired space while focusing on the range of the beam current and welding speed were considered for selecting specific values in DOE. For the same purpose, a numerical simulation was run for selecting the optimum beam current and corresponding welding speed with corresponding ranges for each. To determine the optimality of uniform distribution, the maximum spacing of the resulting heat input level was minimized for an equivalent 2 × 2 DOE. The spacing of 40 J/mm for 4 distinct heat input levels in the range of 180-300 J/mm represented uniform distribution

characteristics (see Figure 3.4). The higher current values required the higher values of welding speed. With reference to the numerical simulation results, maximum current = 65 mA with a range of beam current = 10 mA was selected for the finalized DOE discussed in the following section.

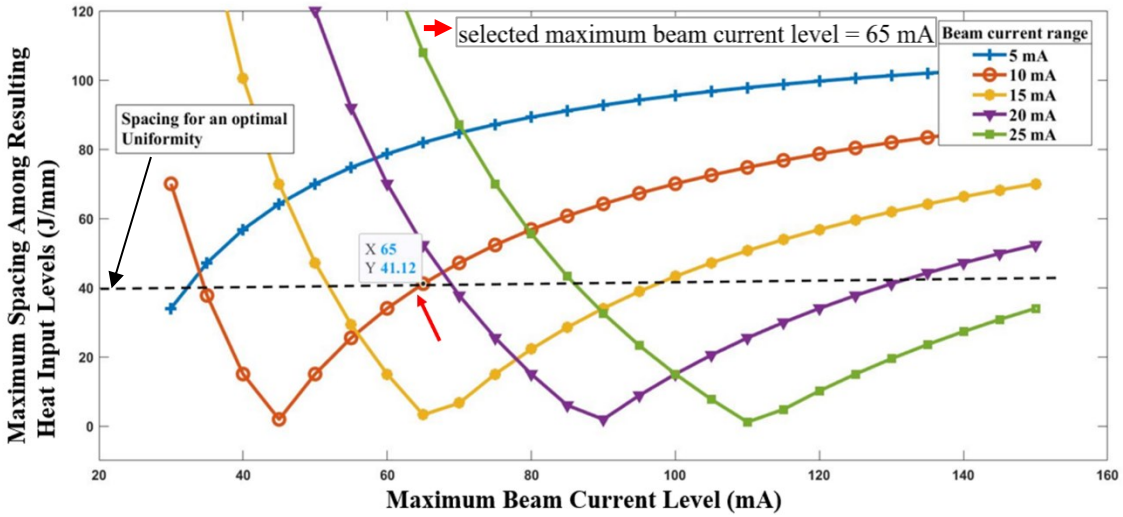

Figure 3.4 Numerical optimization for variable level and range selection from an equivalent 2 × 2 DOE

3.3.4. Finalized DOE

Table 3.2 Finalized DOE Characterization for EBW of Rolled IN718

Type of DOE	Full Factorial
Variables	Beam Current, Beam Voltage
Dependent variable	Heat Input
Number of levels for each variable	3
Total distinct combinations	9
Number of repeats for each combination	2
Total iterations of the experiment	18

With the help from the preliminary DOE framework and numerical optimization explained above, a finalized DOE with quantified process parameters was developed and executed as shown in Table 3.2 and Table 3.3.

The DOE executed for this study had the variables defined with corresponding coupon labels (labeling is discussed in section 3.4) as shown:

Table 3.3 Finalized Design of Experiments for EBW at 50 kV beam voltage

Weld Coupon Label	Welding Speed (mm/min)	Welding Speed (mm/s)	Beam Current (mA)	Heat Input (J/mm)
A1	660.4	11.007	65	295.3
A2			60	272.6
A3			55	249.8
A4	787.4	13.123	65	247.6
A5			60	228.6
A6			55	209.6
A7	914.4	15.240	65	213.2
A8			60	196.8
A9			55	180.4

3.4. Procurement and Setup

From the preliminary DOE, it was required to have a total of 18 tensile specimens, out of which exactly 9 had a distinct set of parameters; the other 9 specimens

were used to take care of the repetition of each combination of parameters. Knowing the dimension of each standard tensile specimen, the IN718 plate of dimension 305 × 152.4 × 13.35 mm thick was procured from Huntington Alloys Corporation for this study. The dimension of the plate was selected taking into consideration of suitable clamping for alignment during welding. The as-received annealed hot rolled plate conforming to the SAE AMS 5596M / ASTM B670-07 standards had rolling direction (RD) along the plate length (305 mm) and grain size of 40 μm (ASTM #6.5). Its chemical composition (wt%) is mentioned in Table 3.4.

Table 3.5 lists the material specification.

Table 3.4 Nominal chemical composition (wt%) range of as-received IN718 (Huntington Alloys Corporation, USA, 2019)

Ni	Cr	Fe	Nb	Mo	Ti	Al	Co	Cu	Si	Mn	C
53.48	18.15	17.88	5.17	3	0.98	0.53	0.18	0.14	0.09	0.07	0.03

Table 3.5 Mechanical properties of as-received annealed hot-rolled IN718 (Huntington Alloys Corporation, USA, 2019)

YS (MPa)	UTS (MPa)	Elongation (%)	Hardness (HRB)
381	837	57.2	90.2

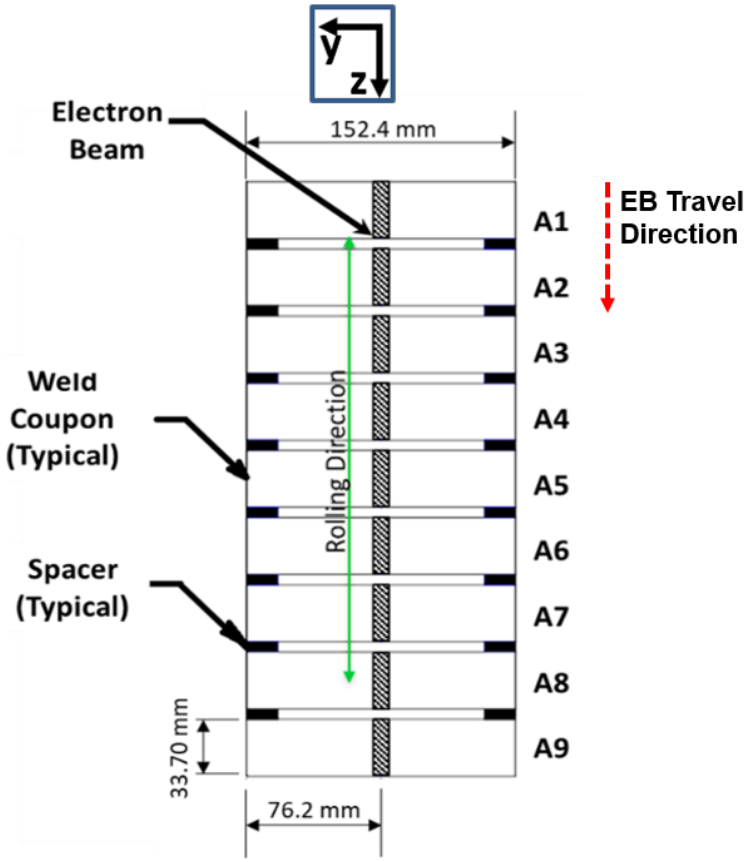

Figure 3.5 Schematic of weld coupons assembly with spacers

The as-received plate was sectioned using wire-type Electrical Discharge Machining (wire-EDM) across the length into nine equal welding coupons (152.4 × 33.7 × 13.35 mm thick). EDM was used to mitigate material properties alteration during machining, to achieve a good surface finish and hence a fine alignment for the assembly in a later stage. Each weld coupon was cleaned with acetone and labeled with the corresponding coupon label (ref. Table 3.3 for label value) at three specific locations for ease of identification of test specimens using an electric engraver before welding. The location of labels for a hardness coupon and tensile specimens for individual weld

coupon is shown in Figure 3.6 (top view of a weld coupon). The coupons were assembled for welding with uniform spacers to mitigate heat propagation amongst the assembled coupons. The assembly (as shown in Figure 3.5) was held together on the EBW machine bed with special clams and fixtures to keep the alignments intact.

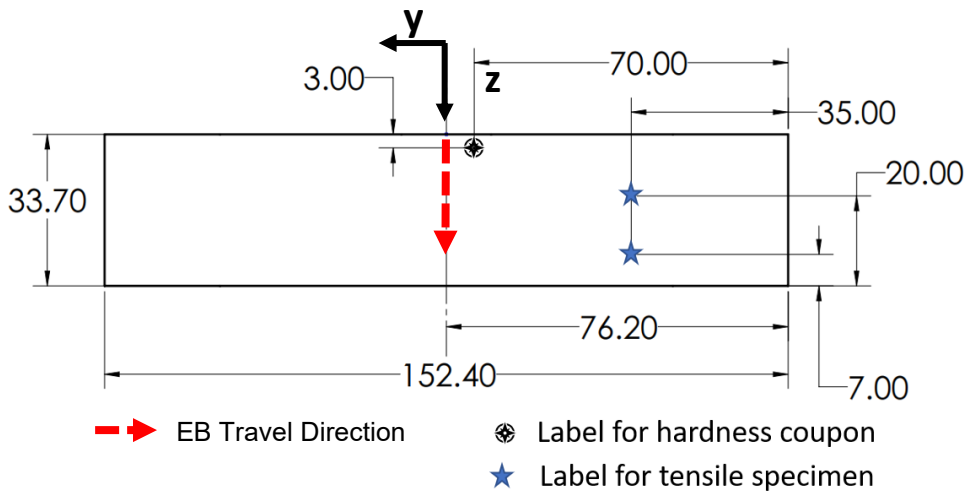

Figure 3.6 Test specimen labeling location when individual weld coupon observed from the top before EBW

3.5. Electron Beam Welding

Electron beam weld beads were produced (bead on metal) without beam oscillations on the coupons along the rolling direction using the Sciaky EBW system having a maximum capacity of 30 kW. Section 3.3 discussed the process parameters selected as variables. The specific EBW parameters corresponding to each weld coupon label were controlled by an integrated computer system of the machine meaning designated beam current and beam voltage were selected at the specified reference distance by the computer control. All beads were produced by a single pass of the

electron beam in the order over the assembly stated in the previous section. Performing the same experiment in a randomized arrangement of iterations is preferred where each tensile specimen is cut from a separate weld coupon set apart by spacers. A schematic of a typical weld coupon, EBW gun, and test specimen orientation is shown in Figure 3.7. Except for beam current and beam voltage, the EBW parameters were kept constant as mentioned in Table 3.6.

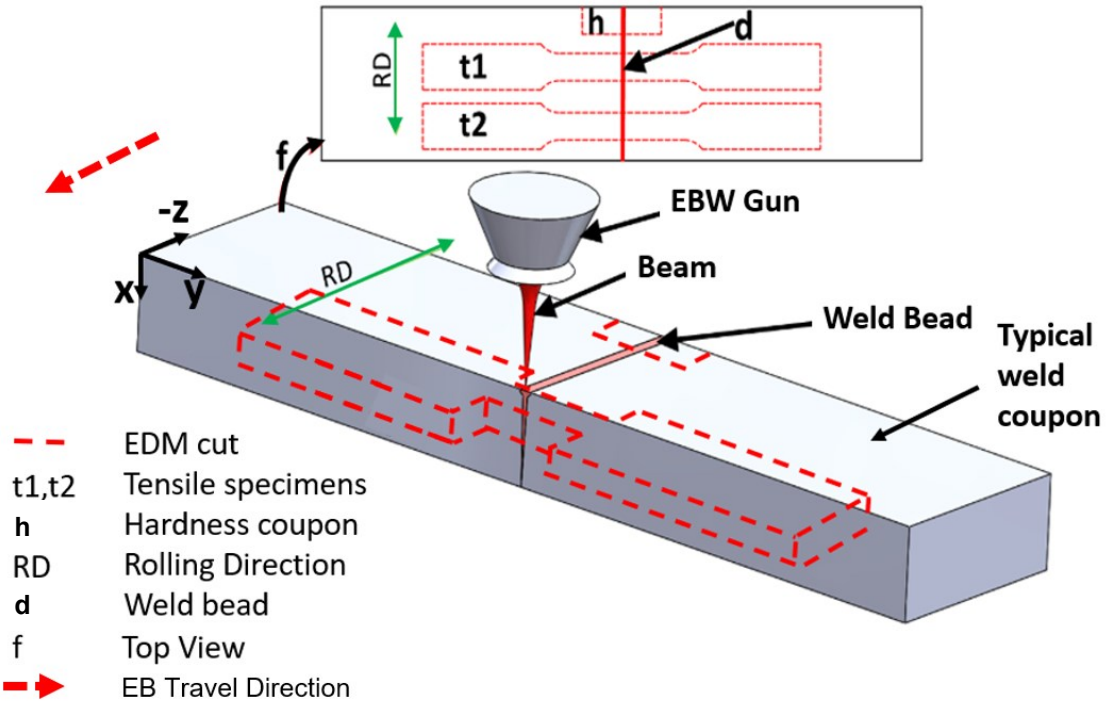

Figure 3.7 Welding and EDM setups

Table 3.6 EBW parameters kept as constants for the experiment

Parameter	Value
Electron Beam Voltage (kV)	50
Electron Beam Focus location	On the surface of the coupon
Vacuum level (μTorr)	~22
Number of Beam Pass	1
Beam Oscillation Type	No oscillations (straight)

3.6. Stress-relieving

After EBW, all weld coupons were stress-relieved at 970 ˚C for 1 hour to minimize the effect of residual thermal stresses which can distort tensile specimens while machining or induce bending stresses in the tensile testing process.

3.7. Production of Test Specimens

Each coupon, having a distinct but constant set of EBW parameters, was then used to produce one hardness coupon (20 × 6 × 13.35 mm) in a transverse cross-section and two tensile specimens (ASTM E8 standard sub-size specimens) as shown in Figure 3.8. To produce the hardness coupons wire-EDM was used; to produce the tensile specimens milling (to reduce the thickness of each weld coupon to 6 mm by removing 2 mm from the top and the rest from the bottom) followed by wire-EDM was exercised.

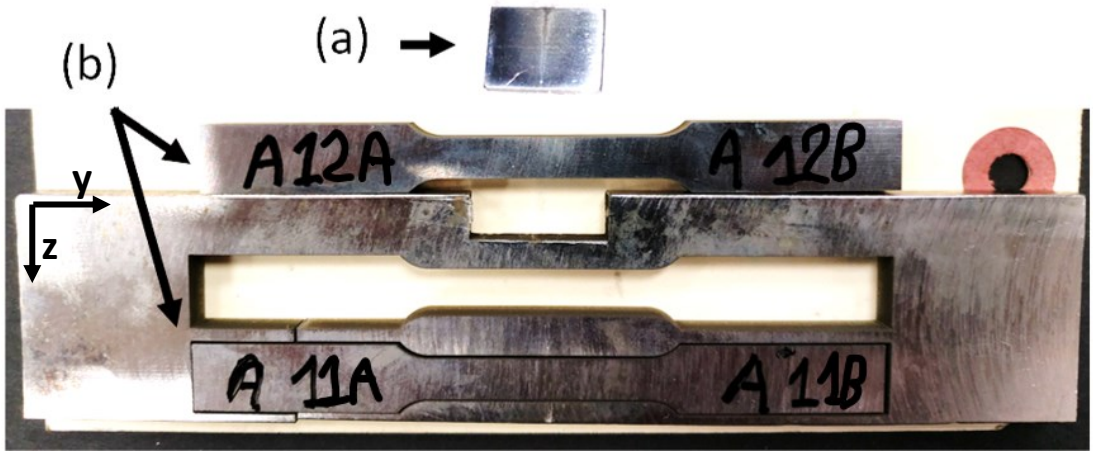

Figure 3.8 Actual test specimens' production from individual weld coupon when viewed from top (a) one transverse cross-section hardness coupon and (b) two tensile specimens top view

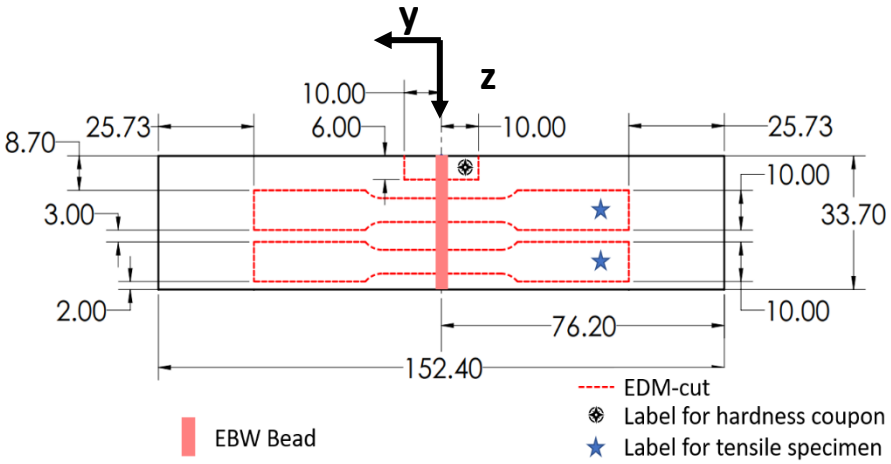

Figure 3.9 Schematic of test specimens' production from individual typical weld coupon when viewed from the top

To further understand the relative orientation of cut test specimens, weld coupon, and EBW bead; schematics are attached in Figure 3.9 (context: weld coupon observed from the top after EBW). and Figure 3.10 (context: weld coupon cross-section observed

from the front after EBW). A standard ASTM E8 sub-size tensile specimen (for thickness <= 6 mm) geometry is attached in Figure 3.11.

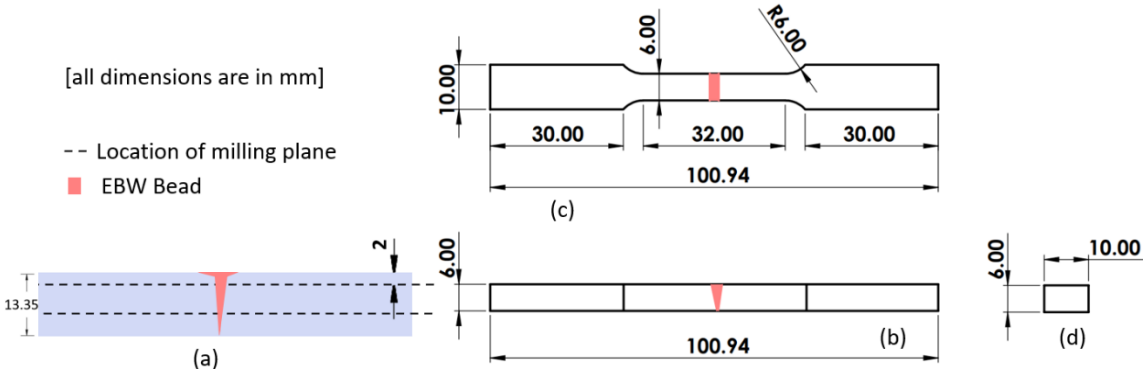

Figure 3.10 Schematics of typical tensile specimen production (a) when each weld coupon cross-section viewed from the front (milling planes location before cutting out individual tensile specimen), EDM-cut tensile specimen (b) front, (c) top (ASTM E8), (d) side view

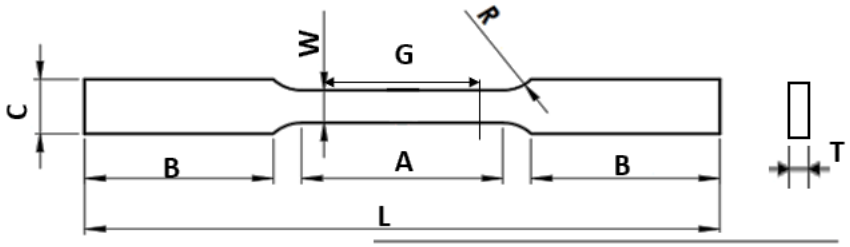

	6 mm < T ≤ 19 mm	T ≤ 6 mm
		Subsize Specimen
	Sheet-Type, 12.5 mm [0.500 in.] Wide	6 mm [0.250 in.] Wide
	mm [in.]	mm [in.]
G – Gage Length	50.0 ± 0.1 [2.000 ± 0.005]	25.0 ± 0.1 [1.000 ± 0.003]
W – Width	12.5 ± 0.2 [0.500 ± 0.010]	6.0 ± 0.1 [0.250 ± 0.005]
T – Thickness	thickness of material	
R – Radius of fillet, min	12.5 [0.500]	6 [0.250]
L – Overall length, min	200 [8]	100 [4]
A – Length of reduced section, min	57 [2.25]	32 [1.25]
B – Length of grip section, min	50 [2]	30 [1.25]
C – Width of grip section, approx.	20 [0.750]	10 [0.375]

Figure 3.11 ASTM E8/E8M standard tensile specimen geometry as per specimen thickness (adapted and refined)

3.8. Pre-test Sample Preparation

After receiving test samples, it was required to follow some prerequisite activities before testing to minimize possible sources of errors in the test observations and to produce reliable test results. They were performed in order as explained below.

3.8.1. Labeling

As mentioned in the previous section, the labeling of individual weld coupons was done before welding to designate corresponding welding parameters to each. The locations of labels were selected to have at least one label on each test specimen. After the production of test specimens, old labels were verified and new labels were produced for the tensile specimens on the surface being cut by EDM. The tensile specimens were expected to be clamped at the location of old labels and it was equally important to code each end of the tensile specimen to avoid mismatch for future fractographic analysis. An electric engraver was used to produce a specific labeling scheme as mentioned in Table 3.7. The table shows labeling for the weld coupon A1 and generated test specimens from it. The same scheme was implemented for the other weld coupons. The labels on each end of a typical tensile specimen are mentioned in Figure 3.12.

Table 3.7 Labeling scheme for test specimens produced from the weld coupon A1

Part	Weld Coupon	Hardness Coupon	Tensile Specimen #1 ends	Tensile Specimen #2 ends
Label	A1	1	A11A	A12A
			A11B	A12B

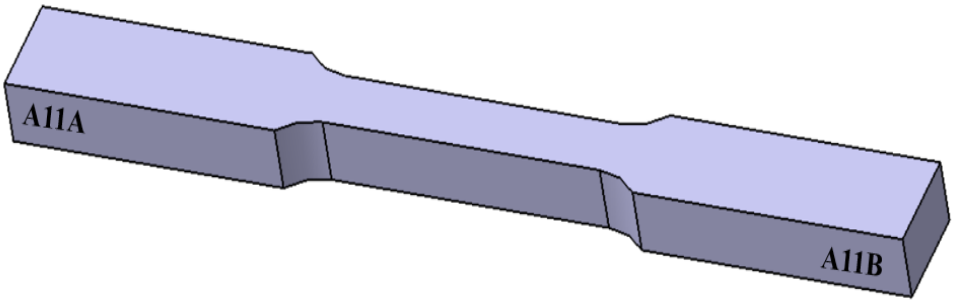

Figure 3.12 Implementation of labeling scheme on tensile specimen #1 from the weld coupon A1

3.8.2. Metallurgy Sample Preparation

- **Grinding**

Figure 3.13 Handimet grinder with different grit size abrasive papers

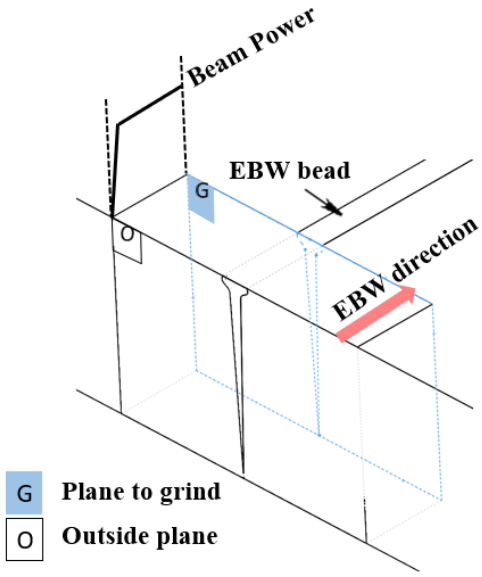

Figure 3.14 Location of the plane to grind on typical hardness coupon

All hardness coupons were ground using SiC abrasive papers of 240, 320, 400, and 600 grits on the Buehler Handimet grinder. The equipment is shown in Figure 3.13 which had a provision to accommodate and replace the papers with different grit sizes as needed as well as to provide water-flow to remove the debris. The coupons were ground on the surface with the transverse weld profile where EDM-cut was exercised (marked as plane "G" in Figure 3.14). The outside plane "O" was briefly ground to just break sharp corners and eliminate possible convexity as it would serve the support to stabilize the coupon during hardness testing. The grinding process of plane "G" followed a systematic sequence of abrasive papers (in the increasing order of grit size) and specific orientation on each as mentioned in Figure 3.15. The corresponding grinding

marks, their spacing, direction, and resulting surface irregularities schematics are mentioned in the same figure after each grinding cycle on a particular paper. The characteristics of orientation helped to determine the adequacy of each grinding cycle. After grinding, macro-finish was obtained on the plane "G" (ref. Figure 3.16) further was finely polished as explained in the next section.

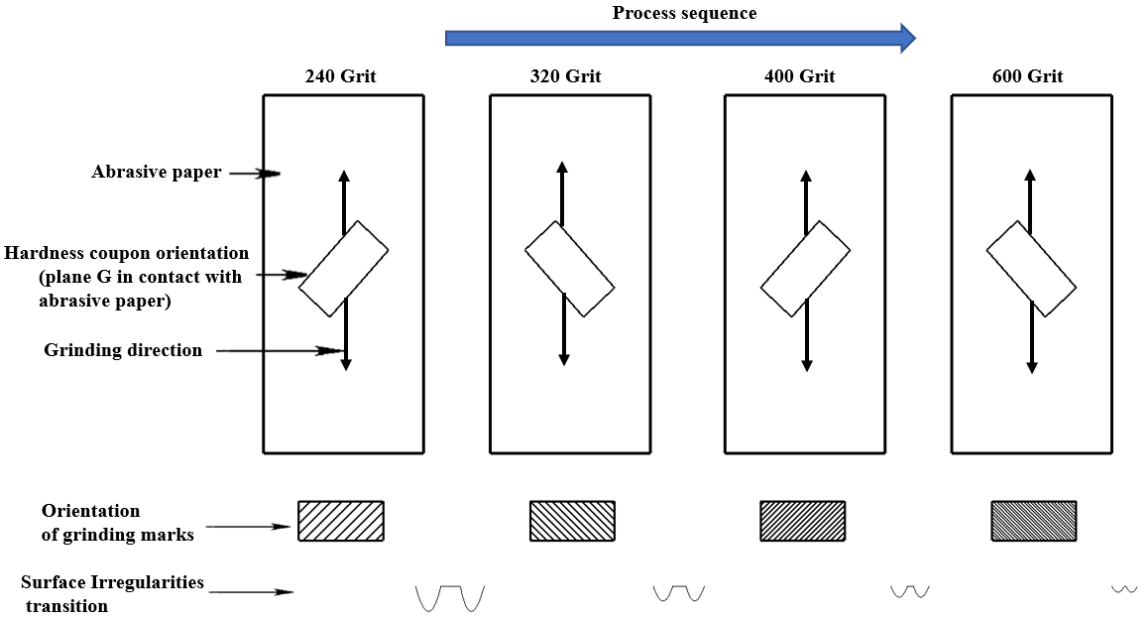

Figure 3.15 Sequence of grinding process, resulting grinding marks orientation and surface irregularities transition schematics

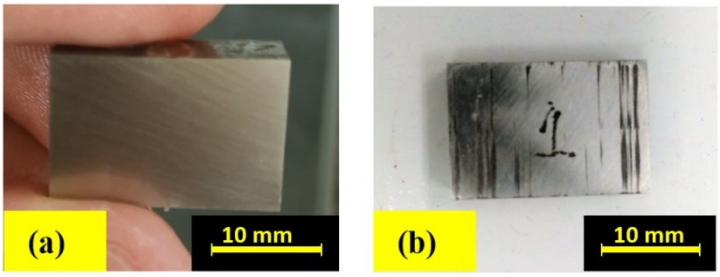

Figure 3.16 Typical hardness coupon after finishing grinding process (a) plane "G" (b) plane "O"

- **Polishing**

The ground surfaces of hardness coupons were further polished using the diamond paste of different sizes to obtain a micro-finish. The 7/5-micron, 1-micron, and 0.5-micron diamond pastes are shown in Figure 3.17(a). The coupons were polished in two steps: first with 7/5-micron paste and then 1-micron paste. For the polishing, Dremel 4300 portable hand polisher with a cotton wheel attached to the front was used. Q-tip cotton swabs were used to evenly spread the diamond paste on the wheel. The polishing station with a glass shield and clamp is shown in Figure 3.18. Before changing the diamond paste to different sizes; the cotton wheel was changed, and ultrasonic cleaning was used to clean any remnant particles on the polished surface in between the steps of polishing. Isopropyl alcohol was used as a medium to clean the surface for ultrasonic cleaner (see Figure 3.19). The polished and cleaned samples were stored in a dust-free air-tight enclosure to avoid any possible contamination before testing.

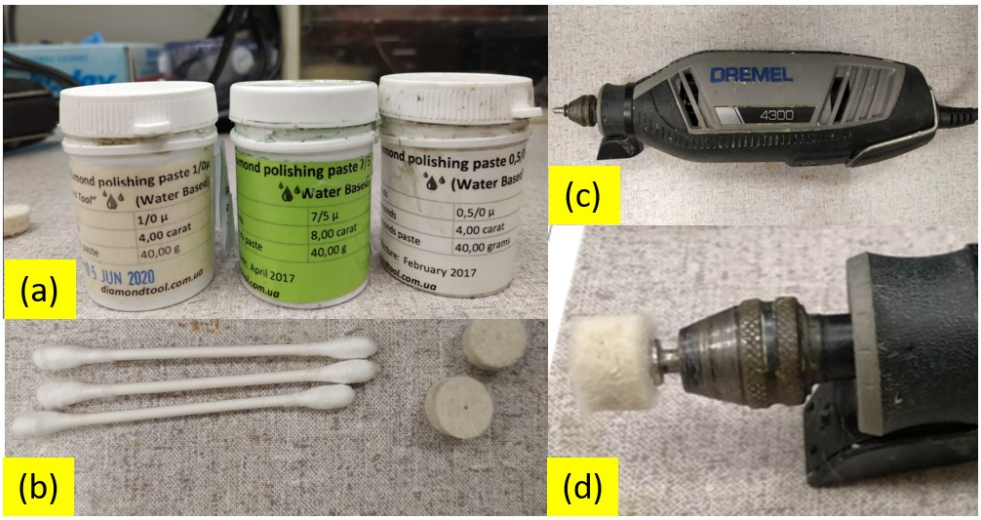

Figure 3.17 (a) Diamond polishing pastes (b) Q-tip cotton swabs and cotton wheels (c) Dremel 4300 hand polisher (d) Cotton wheel attached to the portable polisher front

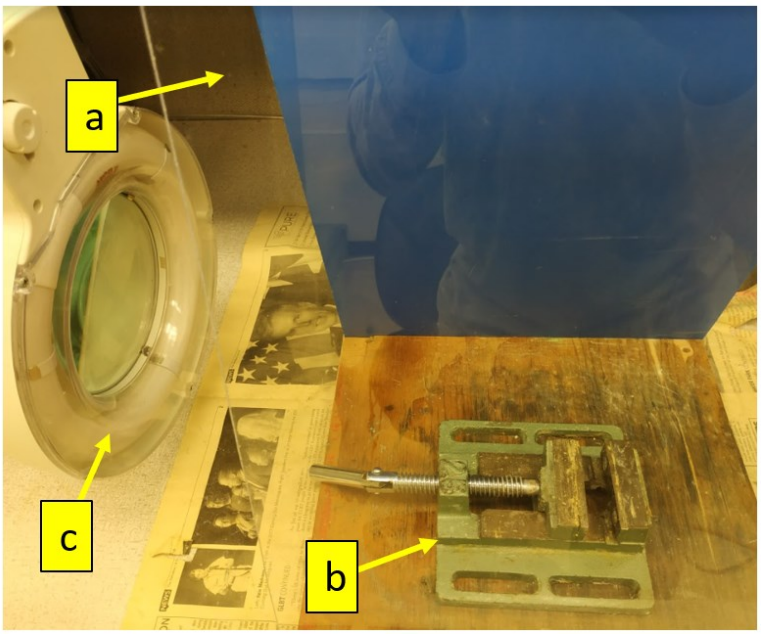

Figure 3.18 Polishing station used in the lab. Legends a: glass shield, b: clamp, c: light

Figure 3.19 Struers Metason 200 ultrasonic cleaner

- **Etching**

The polished surfaces were chemically corroded by the etching process to reveal the transverse section weld profile, microstructure surface defects such as microfissuring as well as keyhole root-void defects, and inclusion defects such as possible surface contamination. The etching was executed conforming to ASTM E407-07 by rubbing the Aqua Regia etchant (a mixture of concentrated HC*l* (33%) and HNO_3 (67%) in volume proportion of 4:1) over the polished surface using cotton swabs. Two droppers each for specific acid were used to take out 4 ml of HC*l* and 1 ml of HNO_3. A Petri dish was used to mix both acids and easily use the mixture with the cotton swabs. A trial etching was done on a corner with 15 sec followed by increments of 10 sec until the fusion zone interface and the grain boundaries were visible. It was observed that 15-sec etching was safe without any possibility of over-etching. All the fusion zone etching time was set to 25 sec for satisfactory results. After etching, the specimens were carefully cleaned with water and blow-dried using compressed air.

3.9. Heat Treatment

As mentioned before, stress-relieving heat treatment was performed for all weld coupons before cutting out test specimens. After completing the first run of all tests, standard solution treatment and dual aging cycle as per ASM Specialty Handbook (see Table 3.8) was performed only on hardness coupons to evaluate the change in the hardness values.

Table 3.8 Standard heat treatment (solution treatment+dual aging) for IN718 as per ASM standards

Temperature (˚C)	Holding time (hour)	Cooling Temperature (˚C)	Cooling method
980	1	Room Temperature	Air cooling
720	8	620	Furnace cooling
620	8	Room Temperature	Air cooling

3.10. Calibration and Measurements

In order to validate the test results, build trust in the outcomes, and verify repeatability; it was required to perform certain calibrations and measurements on test equipment and specimens.

- **Hardness Tester Calibration**

The Wilson microhardness tester was calibrated using trial indentations on an aluminum 6061 sample. The known value of hardness for the sample was 60 HRB. The recorded observation with 100 gf load and 15 s dwell time for the same sample are mentioned in Table 3.9. The indentations were made in a completely random order far from each other on the sample surface. The average value from 4 indentations was 107.4 HV which was very close to the expected value of 107 HV (accuracy validation). The precision was validated with an observed sample standard deviation of 0.74 HV.

Table 3.9 Calibration of Wilson microhardness tester

Material	Known Hardness (HRB and HV)	Trial 1 (HV)	Trail 2 (HV)	Trial 3 (HV)	Trial 4 (HV)	Average (HV)
Aluminum 6061	60 and 108	106.6	108.1	107.9	106.9	107.4

- **Weld Area Calibration**

The weld profile in a transverse section was observed by an optical microscope. The results of weld geometry were calibrated by knowing the actual dimension and profile of sample A1 measured with a caliper (Figure 3.20).

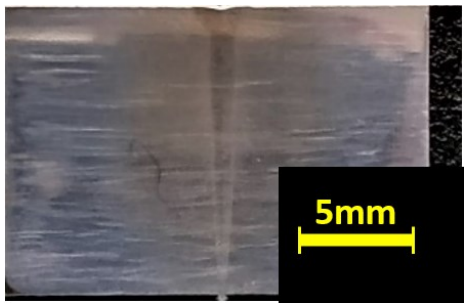

Figure 3.20 Weld transverse section of the sample A1 measured by a caliper (polished and etched)

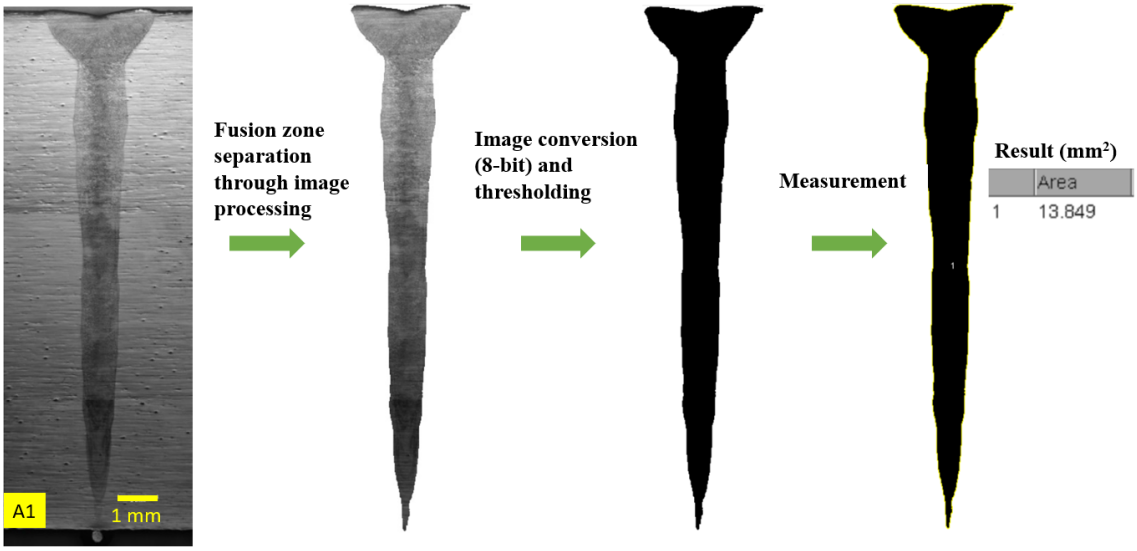

Figure 3.21 Image processing and fusion zone area measurement result for the sample A1

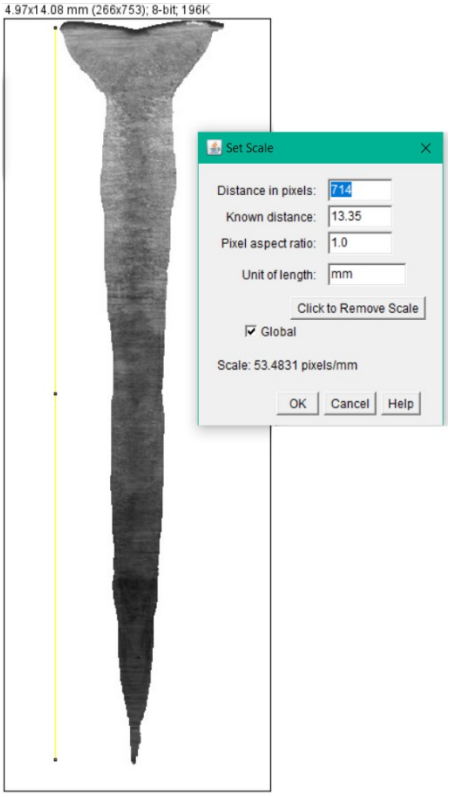

Figure 3.22 A global uniform image scale setup for the sample A1

For the measurements of the area of fusion zone cross-section and penetration depth, microscopic images obtained from Olympus cellSens were used. The image processing and calibration were done using photoshop and ImageJ software. As shown in Figure 3.21 for sample A1, the first fusion zone area was separated through masking and controlling contrast. The obtained image was then converted to 8-bit pictures using ImageJ. A global uniform scale for the picture was set referring to microscopy results (see Figure 3.22). An optimum level of the threshold was selected until the boundary of the fusion zone was identifiable. The targeted zone was captured by the software and the measurement of the area was set as output. The same process was followed for all samples.

- **Calibration for Tensile Testing**

The calibration certificate of the MTS tensile system was checked, and a trial run was made with a steel specimen of known strength. To account for possible machining errors, the cross-section dimensions of the gage section and both grip ends of each tensile specimen were measured with a calibrated Vernier caliper. This helped to produce accurate tensile test results. The gage section width and thickness were measured at sections M1, M2, and M3 to find an average gage cross-section area for each specimen and to see a major variation in the section. The grip end sections' width

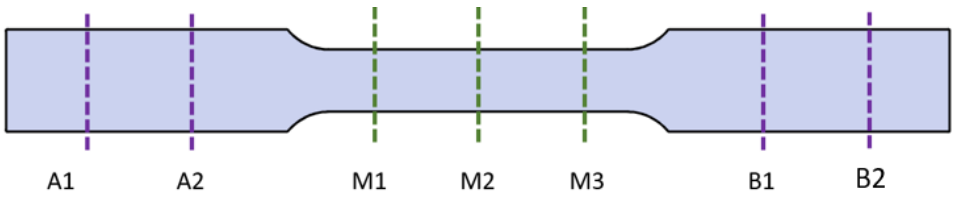

Figure 3.23 Cross-sectional measurements on the indicated location on each tensile specimen

and thickness were measured at sections A1, A2, B1, and B2 as shown in Figure 3.23. At sections A1, A2, B1, and B2; the width was 10.08, 10.09, 10.08, and 10.08 mm whereas the thickness was 6.03, 6.03, 6.03, and 6.03 mm for the sample A11. There was no major change found in measured cross-sectional dimensions of any section that might lead to misalignment of samples during testing and hence inaccurate test results.

3.11. Testing and Analysis Methods

To meet the objective of the research work, the following testing procedures were performed:

1. Microscopic analysis by an OM was performed on the polished and etched surfaces to analyze weld geometry and characterize surface defects such as cracks, voids, and possible contaminations.
2. Microhardness testing by a Vickers hardness tester was exercised to evaluate hardness distribution in the weld zone and base metal at different weld depths.
3. Tensile testing was executed on a universal tensile tester to measure the UTS, 0.2% YS, Young's modulus, toughness, and elongation at fracture of tensile specimens.
4. Microstructure analysis by SEM and attached EDS equipment to understand material matrix morphology on the fracture surfaces and corresponding material composition.

The description of the testing equipment used, and procedure followed is mentioned in the following sections.

3.11.1. Microscopic Analysis

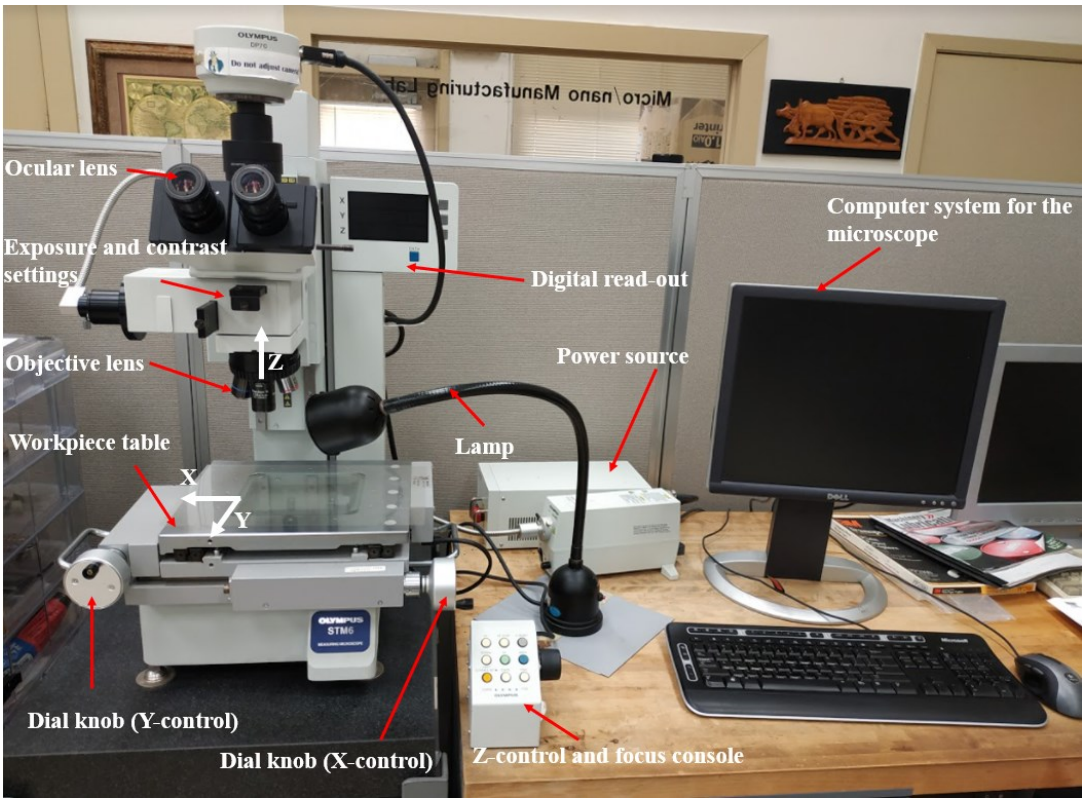

Figure 3.24 Olympus optical microscope used in the lab

Both microscopic analysis of the weld profile and initial fractographic analysis of the fractured surfaces after the tensile test were performed on the Olympus optical microscope (ref. Figure 3.24) integrated with Olympus cellSens software. The samples to be observed were placed under objective lenses of different magnifications (1.25x, 5x, 10x, 20x, 50x). The workpiece table can be moved in two mutually perpendicular axes by dial knobs. With help from Z-control and focus console, lenses can be controlled along Z-axis to tune a fine focus. The exposure and contrast settings can be tweaked to improve the visibility of details. A lamp can be used to improve avoid any shades which can't be eliminated otherwise. A lower magnification lens was used to observe an

overall profile and to locate the defects whereas higher magnification lenses were used to further investigate cracks and other defects in detail. The images were captured from the computer system and can also be seen from ocular lenses. The captured images were then be processed to calculate penetration depth, fusion zone cross-section area, and maximum weld width. Microscopy results were also useful to understand the weld profile in general, evident cracks, porosity, and key-hole defects at different heat input levels.

3.11.2. Microhardness Testing

Microhardness test on the polished surface was carried out using the Vickers hardness tester (Wilson VH1102) at 100 gf load and 15 s dwell time. The parameters and indentation cycle can be controlled by a digital read-out scale as shown in Figure 3.25. The indentations on the IN718 hardness coupon were made from the weld center through HAZ to the base metal in both directions at two different weld depths of each sample (x = 0.3 and 4.8 mm). At each depth, the distance between two successive indentations was kept at least 0.18 mm (greater than 3 × major indentation diagonal) to avoid possible work hardening effect from adjacent indentations. Too close indentations tend to show plastic deformation effects on the hardness distribution. Care was taken to maintain the same criterion between an indentation and the closest boundary of the material. Between the two depths, four equally spaced indentations (at weld depths, x = 1.2, 2.1, 3.0, and 3.9 mm) were made along with the penetration depth on the weld centerline. The indentation, axis, and minimum spacing criterion on a sample are represented by a schematic attached in Figure 3.26.

Figure 3.25 Wilson VH1102 microhardness tester (source: Buehler Materials, https://www.buehler.com/wilson-VH1102-1202-micro-hardness-tester.php)

Few trial indentations were taken to obtain the maximum diagonal distance (d_{max})of a diamond indentation. d_{max} was found to be 30 µm for the samples with no heat treatment. While meeting the spacing criterion, it was important to have at least a few indentations within the fusion zone. For the same, the following calculation was made to obtain the maximum number of indentations (n) in the fusion zone. The minimum fusion zone width of 860 µm was considered. 9 indentations in the fusion zone width at x = 4.8 mm were enumerated within the limit agreeing to constraints. For the study, the distance between two successive indentations was kept at least 0.18 mm. The same microhardness test on all of the samples was performed before and after the heat

treatment (ref. section 3.9) to understand variations in the hardness at different weld depths due to the heat treatment.

$$(n-1)3dmax + dmax = 860 \quad (3)$$

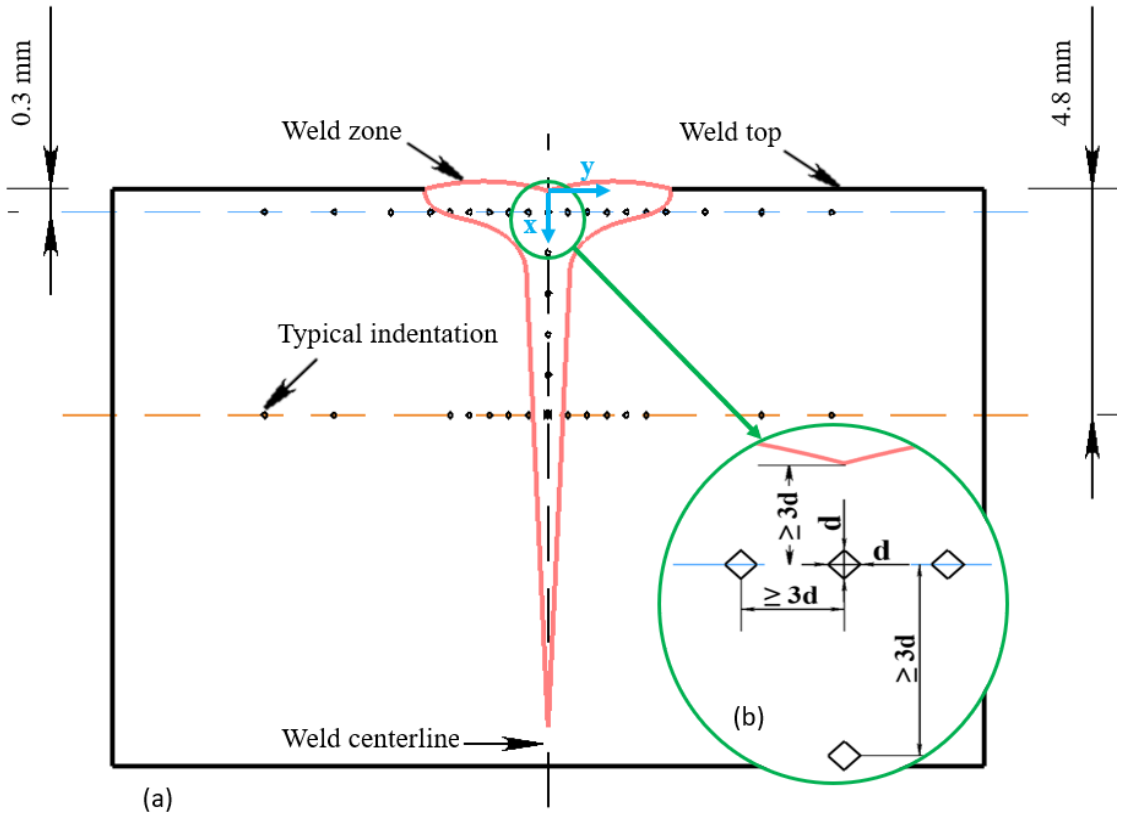

Figure 3.26 Indentation schematic on a test sample with (a) set coordinate system (b) minimum spacing criterion

3.11.3. Tensile Testing

Tensile tests were carried out on the MTS 810 material tester as shown in Figure 3.27. The test was conducted at room temperature. The loading direction was perpendicular to the rolling direction as illustrated in section 3.5. The machine was hydraulically powered. The displacement of the crosshead can be controlled by the

computer or manually with the help of a remote console (picture attached in Figure 3.29(a)) or a pressure release mechanism on the frame. The displacement-control approach was adopted with a crosshead speed of 0.5 mm/min and a load-cell of 100 kN following ASTM E8 standards. Other test parameters are mentioned in Table 3.10. The data acquisition frequency was set at 5 Hz. A 3D printed spacer (see Figure 3.28) made from ABS plastic was incorporated to ensure repeatability of the true alignment of the tensile specimen in the grip. The thickness of the spacer was kept less than 6 mm so that it did not affect the loading on the test specimen. The mechanical grips of size 0-6 mm (0-0.25 in) were used. As shown in Figure 3.29, the grips were tightened using levers. The upper grip-head can be moved up and down while the lower grip-head was stationary. Enough care was taken during clamping to eliminate preloading and slipping of the grips over the surface of a specimen. A procedure was created with designated settings before running the test. After each fracture, the broken samples were carefully stored to analyze fracture surfaces at a later stage. Force-displacement data was obtained from the computer system. Knowing the average gage length and gage cross-section area of each specimen, stress-strain curves were produced to analyze mechanical properties at different heat inputs.

Table 3.10 Tensile test parameters

Parameter	Value
Implemented standard	ASTM E8/E8M
Control method	Displacement controlled
Maximum permissible crosshead speed (mm/min)	0.05 per unit gage length
Gage section length (mm)	32
Load cell (kN)	100
Set strain rate by crosshead speed (mm/min)	0.5
Test temperature (° C)	22
Data Acquisition frequency (Hz)	5

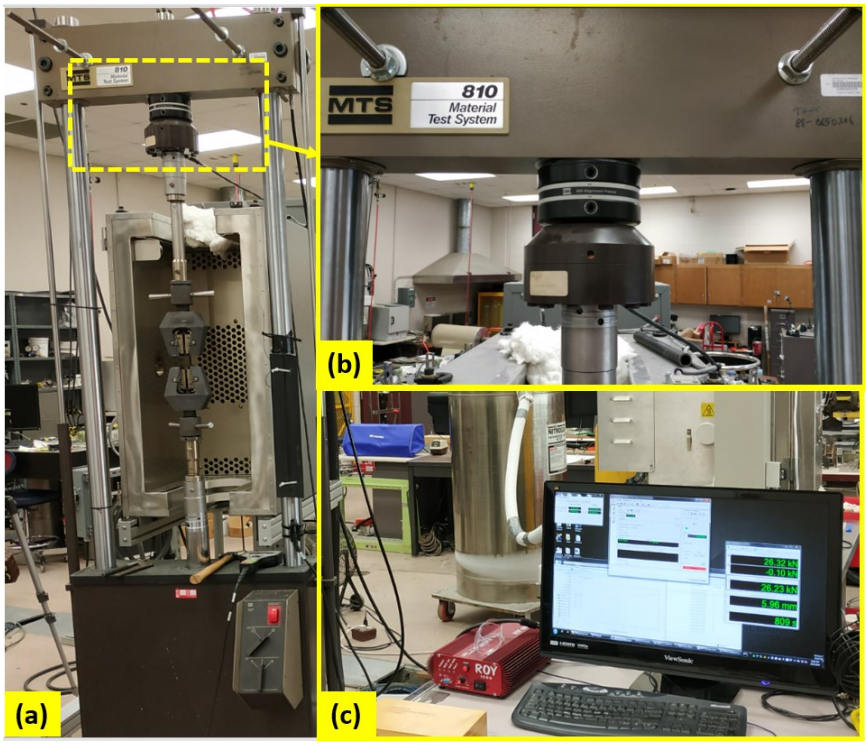

Figure 3.27 (a) MTS 810 tensile tester (b) crosshead with 100 kN load cell and alignment fixture (c) computer system with MTS Station Manager software

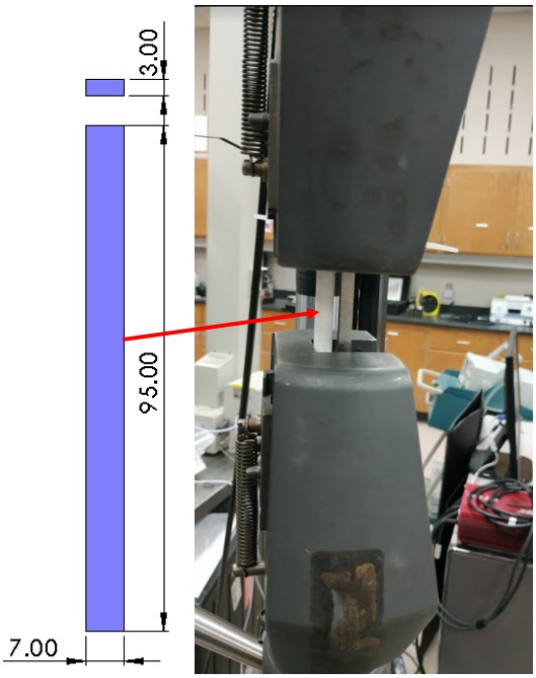

Figure 3.28 3D printed spacer used for vertical alignment setup

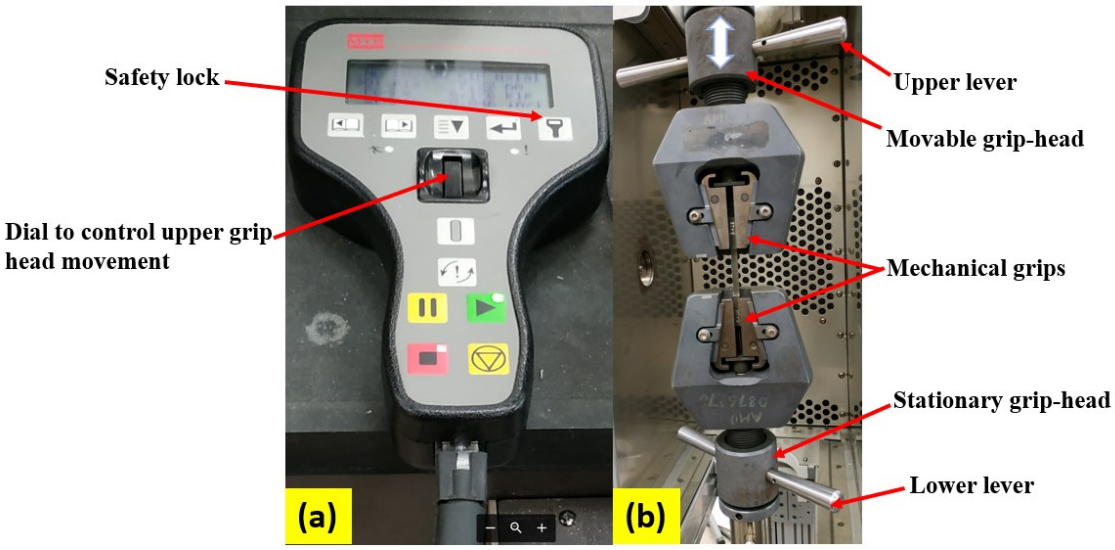

Figure 3.29 (a) Remote console to control crosshead manually (b) mechanical grips with locking levers

3.11.4. Fractographic Analysis

Initial fractographs were produced with the help of an optical microscope to get a collective understanding of the fracture behavior of welds for selected heat input levels. To inspect fracture characteristics and chemical composition of EBW welds in detail, Scanning Electron Microscopy (SEM) and Energy Dispersive Spectroscopy (EDS) were performed on the fracture surface. Before conducting the study, fractured tensile specimens were polished and etched over the width along the gage length to find the relative location of the weld. Vega 3 Tescan microscope (ref. Figure 3.30) and Oxford Instruments x-act instrument were used for SEM and EDS respectively. SEM was performed by fixing the fractured tensile specimen in the sample holder inside the vacuum chamber. A minimum vacuum of 10^{-2} Pa was required to run SEM. A conducting copper tape was used to set the specimen on the holder while keeping no non-conductive entity in direct contact with the test specimen surface (as it might lead to inaccuracies in SEM results). A high voltage of magnitude 15 kV was initially selected for SEM which can be increased to get better results. The site of interest can be brought down under the beam by a controller and the computer interface options. The distance between the test sample surface and the electron beam was changed until a clear image was obtained on the computer screen. The brightness and contrast levels can be changed to get a quality result.

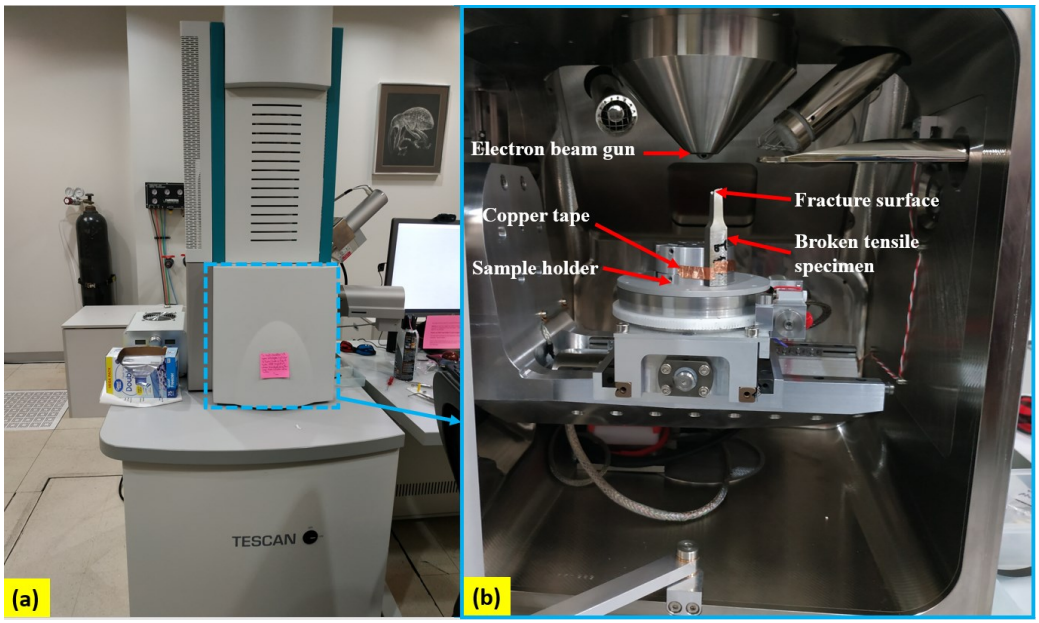

Figure 3.30 (a) Vega 3 Tescan SEM (b) inside vacuum chamber with test specimen clamped

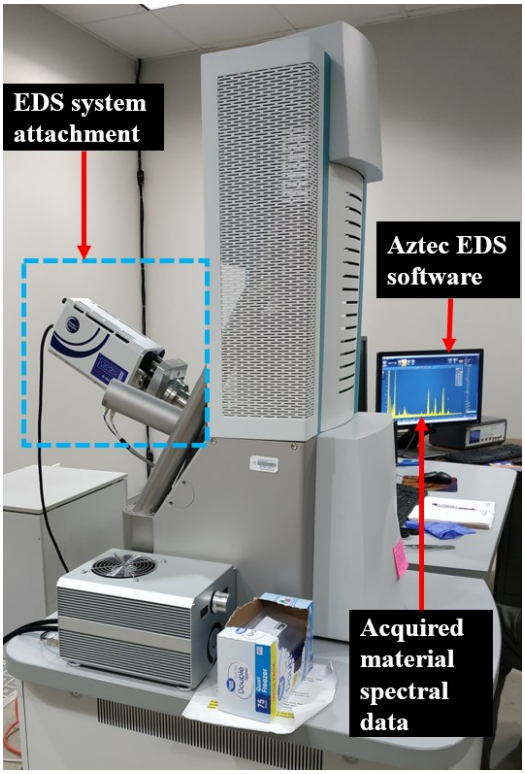

Figure 3.31 Oxford Instruments x-act EDS system attachment to SEM

EDS equipment was attached to the SEM setup as shown in Figure 3.31. An energy level of 10 keV was incorporated for the EDS data acquisition system. Aztec EDS software was used to check the current location on the fracture surface, to initiate the process, and to store the resulting spectral data. The sem software can be operated in two different modes: Analyzer mode and Point&ID mode. The Analyzer mode detected spectral data for the entire site of interest on the SEM screen while the Point&ID mode detected characteristic material composition by spectral data specifically on a selected spot on the screen.

4. RESULTS AND DISCUSSION

Various tests were conducted on the EBW'ed rolled samples to analyze weld quality and characteristics. Analysis from the optical microscope helped to characterize the weld profile, ensuing defects, and changes in the weld geometry. From the microhardness analysis, the distribution of hardness in a transverse section of the welded specimen was obtained. The tensile test described the strength of the welds and important mechanical properties. The fracture characteristics were first depicted based on OM observation of the fractured surfaces and were further analyzed based on microstructure and material analysis with SEM and EDS system. The detailed analysis by EDS was performed by selecting distinctive locations on the fractured surface. The changes in the observed properties were analyzed with respect to change in the process parameters and heat input to draw meaningful interpretations.

4.1. Weld Geometry

The EBW produced deep and narrow welds at different heat inputs as shown in Figure 4.1. A typical "nail shape" weld was seen for all samples. A similar weld profile was seen previously for EBW of IN718 by Huang et al. (2005) and Liu & He (2016). The large "nail-head" shape was seen at the beam entrance (top region of the weld). The slender and sharp "nail point" shape was seen in the deepest region of the weld. The

1. The content of this section has been published under the reference – "Patel, V., Sali, A., Hyder, J., Corliss, M., Hyder, D., & Hung, W. (2020). Electron Beam Welding of Inconel 718 Electron Beam Welding of Inconel 718. *Procedia Manufacturing*, *48*(2019), 428–435. https://doi.org/10.1016/j.promfg.2020.05.065"
2. The authors retain full rights to the content for the academic dissertation. The details can be found: https://www.elsevier.com/about/policies/copyright#Author-rights

width of the transition section from the “nail-head” shape to “nail point” decreased as it approached the bottom of the weld. As the energy from the beam melted the alloy on the top; surface tension, hydrostatic pressure, and Marangoni shear stress pushed the material down growing in a narrower channel to form the typical fusion zone shape.

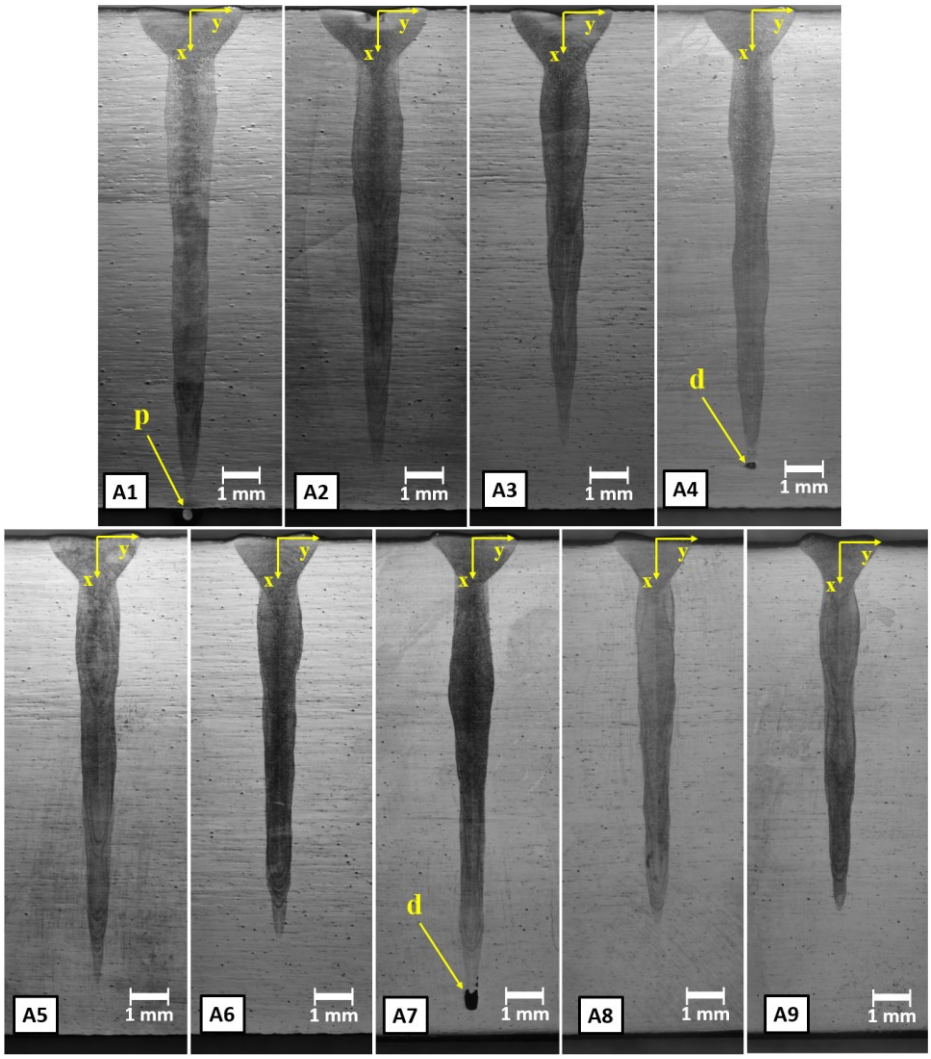

Figure 4.1 Deep penetration by EBW on rolled IN718 specimens at different heat input. Label “p” shows molten metal at the exit end, and label “d” shows void at the weld bottom (keyhole defect)

Different penetration depths, fusion areas, and defects were found depending on the heat input. Simulation of pore formation was reported for the selective laser melting process when a laser beam reacts with metal powder (Khairallah et al., 2016). The scanning laser formed a trench filled with the molten metal below the beam. The dynamic molten metal flowed rapidly upward on both sides of the trench, then collapsed and trapped pores after the laser beam passed by. Assuming similar pore-forming mechanisms for energy beams such as laser or electron beam, a pore could be formed in the EBW fusion zone due to either solidification shrinkage or trapping of pore from rapidly flowing and collapsing of molten metal. The deep electron beam welds with partial penetration are likely to have keyhole root-void defects. The numerical simulations and validation experiments on EBW of thick aluminum showed similar results (Liu & He, 2016). Only at a higher beam current of 65 mA, spiking defect causing root-void was observed. The vapor plumes at the bottom pushed the molten metal pool upwards and insufficient liquid sidewalls were insufficient to fill the void generated at the bottom. A low viscous molten metal would fill all pores if time permits, but a molten metal with high viscosity would flow slowly and might solidify too quickly thereby preventing the pores in the weld from being filled. Pores were seen only at the weld bottoms of the samples A4 (247.6 J/mm), and A7 (213.2 J/mm) which were processed at relatively high scanning speeds (787.4 and 914.4 mm/min) and the highest beam current (65 mA). Such conditions would promote fast cooling rates. The formation of high viscous molten metal that fails to fill the large pores at the welded bottom in limited time formed the keyhole root-void defect (as shown by “d” in Figure 4.1).

Except for samples A4 (247.6 J/mm), and A7 (213.2 J/mm) where voids existed at the welded bottom, all other samples were free from any visible defects when observed with the highest magnification on the optical microscope.

Statistical analysis by Analysis of Variance (ANOVA) was performed to identify significant factors depicting penetration depth. Both the beam current and the welding speed (and hence the heat input) were considered potential factors. The analysis showed the effect of welding speed and beam current (hence heat input) was significant (higher than standardized effect value = 2.16 with 95% confidence as shown in Figure 4.2) to explain the behavior of the penetration depth. ANOVA results (Table 4.1) showed a significant change in the mean value of penetration depths as the factors changed.

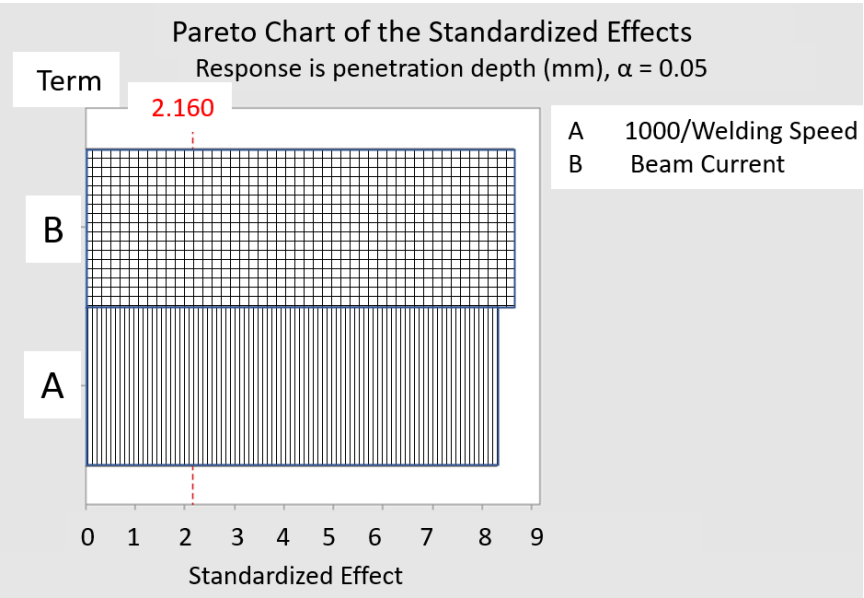

Figure 4.2 Parameter effect analysis for penetration depth

Table 4.1 ANOVA for penetration depth vs welding speed and beam current

Source	DF	Adj SS	Adj MS	F-Value	P-Value
Model	4	18.1981	4.54953	46.54	0.000
Linear	4	18.1981	4.54953	46.54	0.000
1000/Welding Speed (mm/min)	2	8.7594	4.37972	44.80	0.000
Beam Current (mA)	2	9.4387	4.71935	48.27	0.000
Error	13	1.2709	0.09776		
Lack-of-Fit	4	1.2653	0.31632	503.87	0.000
Pure Error	9	0.0057	0.00063		
Total	17	19.4691			

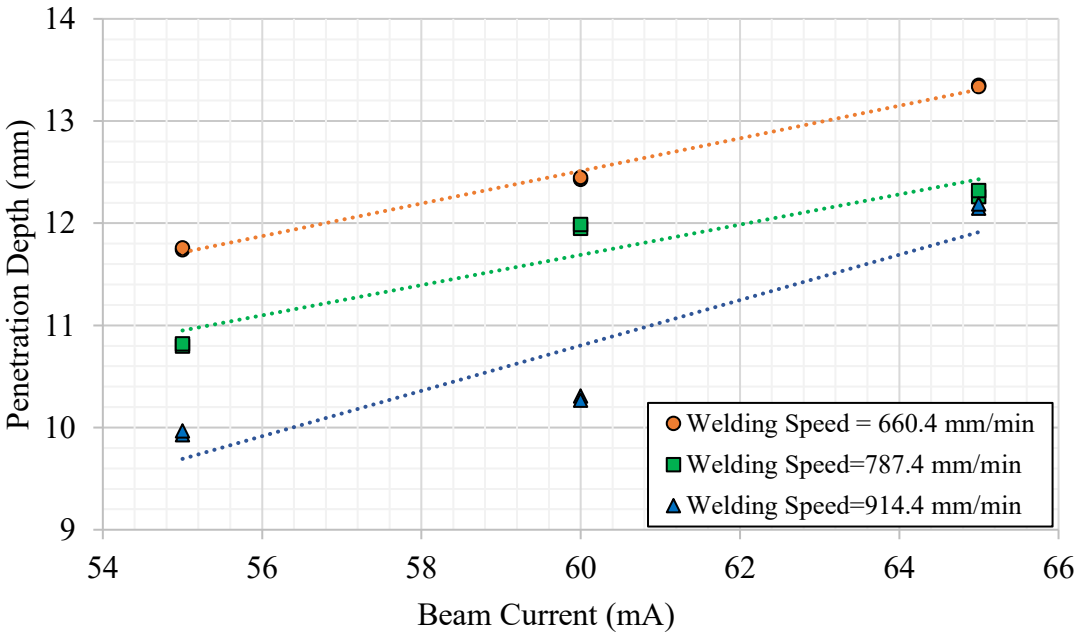

Figure 4.3 Variation in penetration depth at different beam current and welding speed

Sample A1 with a heat input of 295.3 J/mm showed full weld penetration through the thickness of 13.35 mm. At constant beam current, a higher penetration depth was observed as welding speed decreased (Figure 4.3). The penetration depth increased with an increase in the beam current at constant welding speed. Following these results, it was understood that penetration depth can be explained by heat input (combining the individual effects). The penetration depth was found to be directly related to heat input and can be explained by a linear relationship within the exercised range of parameters (Figure 4.4). The linear model explained an increase of 0.026 mm in penetration depth per 1 J/mm increase in the heat input with an R-squared value of 0.78.

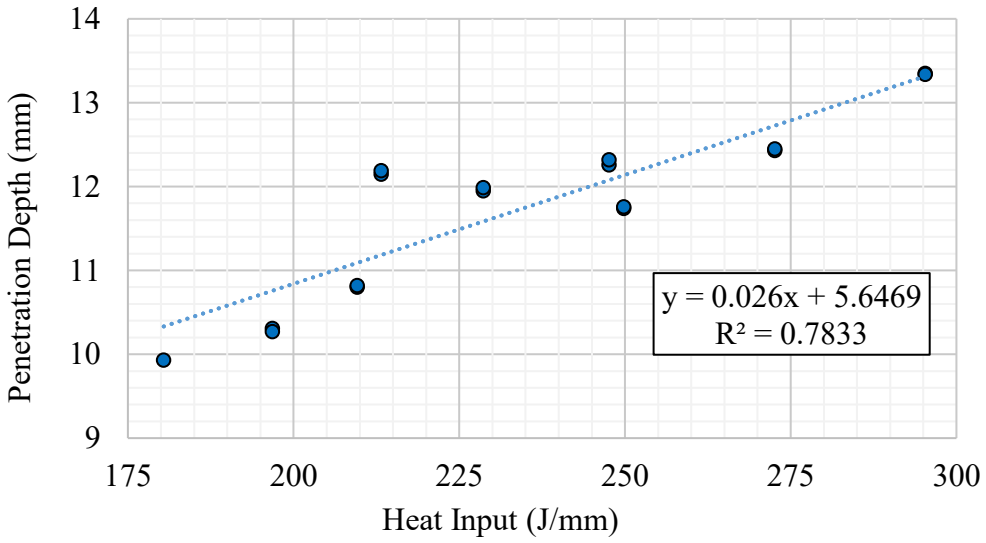

Figure 4.4 Variation in penetration depth with respect to heat input

The power of the beam translates into the weld profile in general. Increasing the beam current increases the number of electrons being exerted and increasing the voltage increases the energy of an electron. Weld profile characterization requires analysis of

width and penetration depth. The weld depth was found to increase slightly (as compared to penetration depth) with an increase in the heat input. An effort was made to analyze the fusion zone area. The statistical analysis (attached in Appendix B) was similar to the analysis of penetration depth. As expected, the fusion zone area was linearly proportional to the heat input within the range of the executed experimental parameters. As the fusion zone area reflected both the effective width and penetration depth of the weld cross-section, heat input explained the behavior of the variation in the fusion zone more accurately by a linear model. The variation in the fusion zone area by each parameter and by heat input can be understood from Figure 4.5 and Figure 4.6 respectively. The linear model explained an increase of 0.047 mm^2 in fusion zone area per 1 J/mm increase in the heat input with an R-squared value of 0.96. Appendix B can be referred for the assumptions of the normal distribution of the residuals and equal variance in the statistical analysis. Similar trends in weld width with heat input were observed by Agilan et al. (2014).

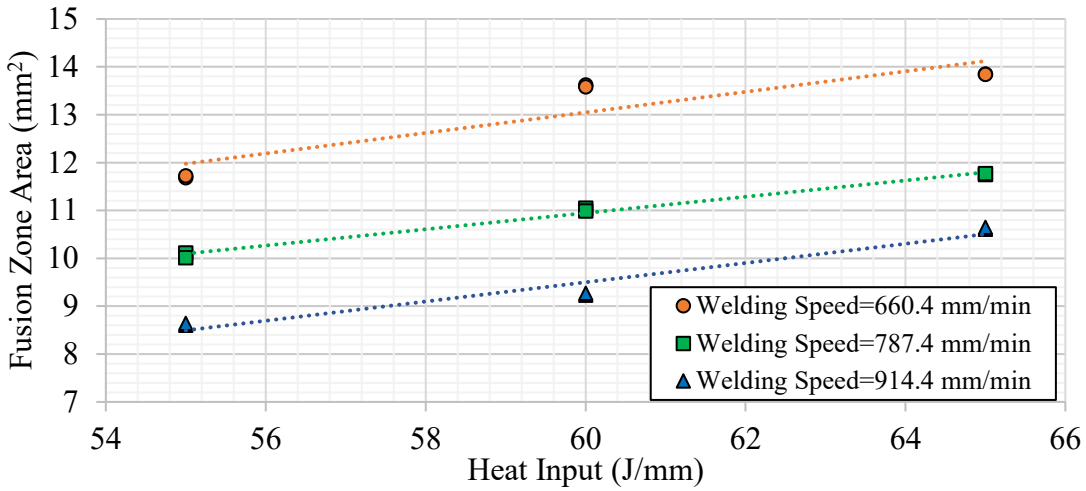

Figure 4.5 Variation in fusion zone area at different beam current and welding speed

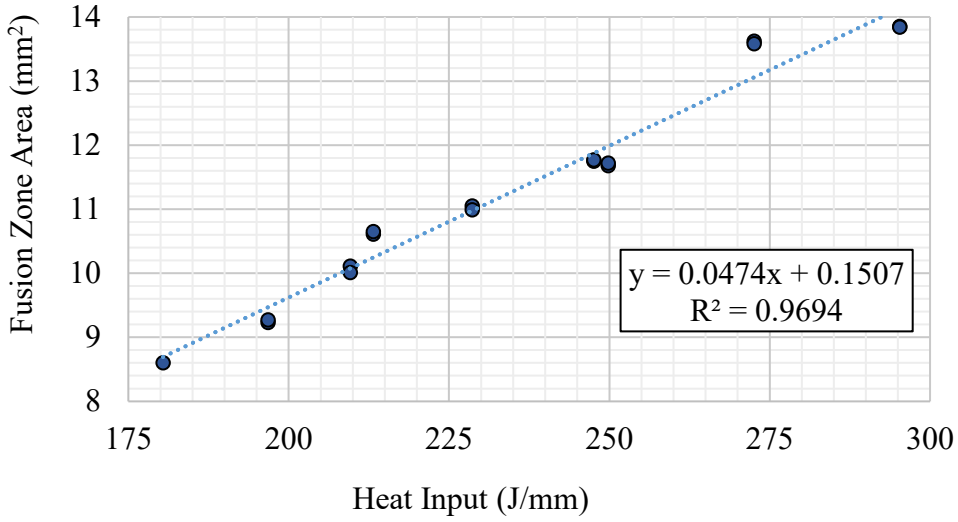

Figure 4.6 Variation in fusion zone area with respect to heat input

4.2. Microhardness

The microhardness distribution was analyzed before and after the heat treatment (solution treatment+dual aging) at different weld depths across the weld zone in a transverse section. A coordinate system shown in Figure 4.1 was implemented for each coupon. The coordinate origin was set at the beam entry point on the weld-top. The positive x-direction indicated the weld depth while the y-direction was kept along the weld width. A typical detailed microhardness distribution of sample A9 (180.4 J/mm) and sample A1 (295.3 J/mm) is attached in Figure 4.7. The figure also describes the hardness distribution before and after being aged. The weld zone and base metal interface are schematically represented by long-dashed and dotted lines at the weld depths of x = 0.3 mm and x = 4.8 mm respectively. The weld zone is wider at the "nail-head" location (at x = 0.3 mm level) compared to a narrower width at the "nail stem" (at x = 4.8 mm level). Table 4.2 compares the average microhardness and standard deviation measured inside and outside of the weld for the three samples A9 (180.4 J/mm), A3 (249.8 J/mm), and A1 (295.3 J/mm) at two different weld depths (0.3 and 4.8 mm) before solution treatment+aging. These samples were chosen to understand the possible change in hardness distribution with respect to the heat input. The bottom section of Table 4.2 lists the microhardness measured at the weld center along with the weld depth. The quantitative comparison of the average hardness values in different zones before and after heat treatment was made from a typical hardness distribution of sample A9 (180.4 J/mm) using the 95% confidence interval of the mean as shown in Figure 4.8.

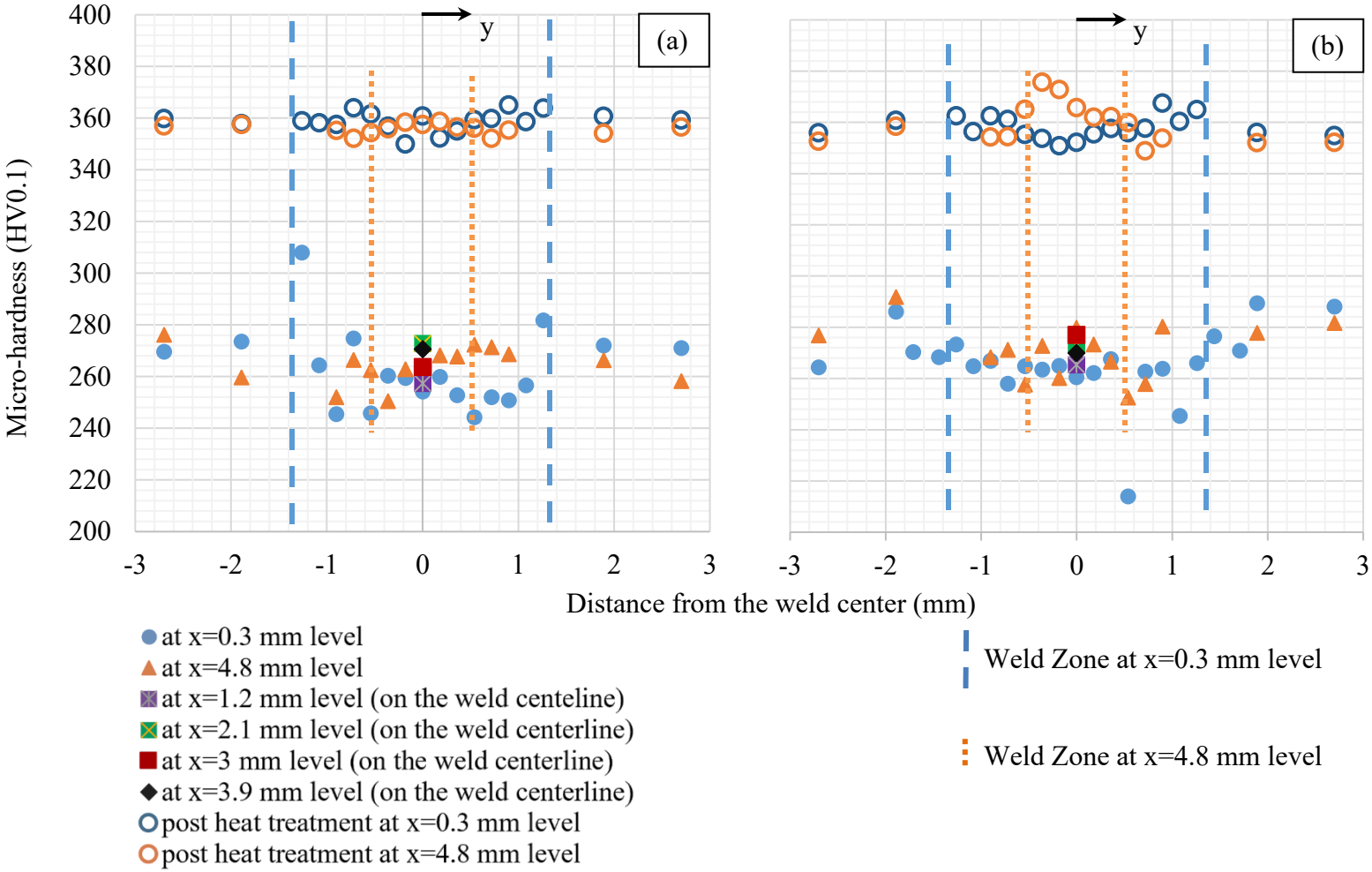

Figure 4.7 Microhardness distribution of EBW'ed samples before and after heat treatment (a) sample A9 (180.4 J/mm) (b) sample A1 (295.3 J/mm)

Table 4.2 Average hardness at different weld depth for three samples with low, medium, and high heat input of EBW before heat treatment

Location to the fusion zone	Sample	A9 (180.4 J/mm)		A3 (249.8 J/mm)		A1 (295.3 J/mm)	
	Depth (mm)	**0.3**	**4.8**	**0.3**	**4.8**	**0.3**	**4.8**
Outside	**Hardness (HV)**	268	265	265	264	277	276
	S. Deviation	17	8	23	12	10	10
Inside	**Hardness (HV)**	254	265	244	260	260	266
	S. Deviation	7	8	24	7	14	10
	Depth range (mm)	**0.3-1.2**	**2.1-4.8**	**0.3-1.2**	**2.1-4.8**	**0.3-1.2**	**2.1-4.8**
Weld Centerline	**Hardness (HV)**	256	270	249	253	263	275
	S. Deviation	2	4	5	3	3	4

From the results attached in Figure 4.7, Figure 4.8, and Table 4.2; the following was found:

- The average values of hardness were not statistically different (with 95% confidence) within the fusion zone, HAZ, and base metal at a given weld depth. The difference in the mean values of hardness inside the fusion zone and outside

the fusion zone was lesser at a depth greater than 1.2 mm before solution treatment+aging. Similar results were obtained by Huang et al. (2005) and Gao et al. (2011). At a deeper location in the fusion zone, the molten metal is not directly exposed to the beam and is surrounded by a colder base metal matrix. This promotes a higher cooling rate having lesser inter-crystalline precipitates (δ-phase) and more intragranular precipitates (γ' and γ"). This further increases the hardness within the fusion zone at a deeper location reducing the harness difference with the base metal.

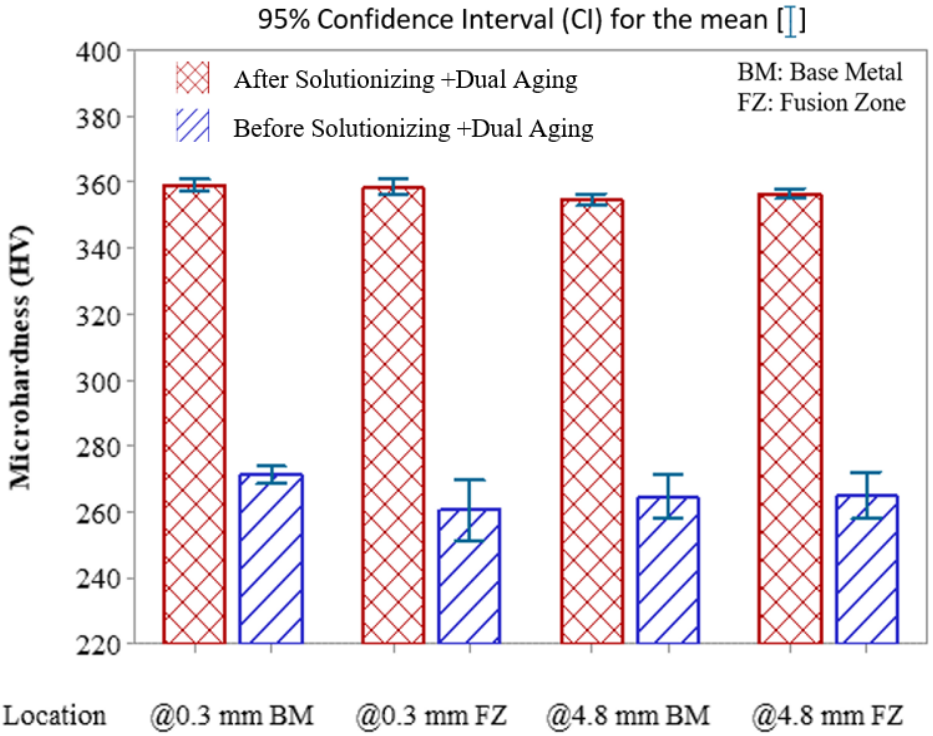

Figure 4.8 Hardness distribution comparison in different zones of rolled EBW'ed IN718 sample A9 (180.4 J/mm) pre and post heat treatment

- Microhardness at the weld center near the beam entrance (x = 0.3 mm) is lower than that at the deeper zone (x = 4.8 mm) before heat treatment. The difference

was more for sample A9 (180.4 J/mm) when compared with samples A3 (249.8 J/mm) and A1 (295.3 J/mm). This may result due to the fact that a higher heat input produced a bigger molten metal pool which transmitted heat at higher depth levels for a longer time which promotes Laves formation (Mei et al., 2016) and further reduce the hardness at a deeper level approaching to the weld-top. The hardness characteristics would be affected by both the microstructure and the resulting chemical composition of the weld. The material in the nail head region was (i) exposed to the beam for a longer time, and (ii) surrounded by a larger pool of molten metal in the weld. These factors would promote grain growth and a greater fraction of Laves resulting in a softer nail head region.

- Being 95% confident, the average hardness values were significantly higher after heat treatment irrespective of the weld heat input or the location in the test sample. The relevant results were reported by Reddy et al. (2009). The changes might be elucidated by resulting precipitates (γ' and γ") and dissolution of Laves due to heat treatment. Further, the variability in the hardness decreased after heat treatment indicating a uniform distribution.
- Similar hardness trends were observed regardless of the heat input values. The slight difference in hardness near the beam entrance and voids at the bottom of the weld zone would not affect the tensile test results since both the nail head region and voids were removed during machining to fabricate the tensile specimens.

The hardness distribution of all other samples is attached in Appendix A.

4.3. Tensile Test Results

Mechanical properties were obtained using the MTS system at room temperature. From the stress-strain curve ultimate tensile strength (UTS, S_u), 0.2% yield strength (YS, S_y), elongation at fracture (ε_f), toughness, and young's modulus were calculated for all samples including their replicates.

Selected fractured tensile specimens were polished over the width along the gage length and chemically etched to confirm the relative location of the fracture zone and the fusion zone. The fracture surface going through the fusion zone and base metal passed through HAZ at some point. All the samples with the lowest welding speed (660.4 mm/min) broke through the weld zone while the samples with the highest welding speed (914.4 mm/min) and medium welding speed (787.4 mm/min) fractured randomly (some away from the weld zone and other through the weld zone). The sample A9 (180.4 J/mm) and its replicate fractured away from the weld zone. The results elucidated the fact of forming unfavorable Laves and Nb segregation in the fusion zone when welded with a higher heat input which decreased the cooling rate and promoted fracture through the weld zone in those cases. The results agreed with a relevant study on the cooling rate and segregation performed by Agilan et al. (2014). Although pores were suspected to be at the weld-bottom of samples A4 (247.6 J/mm) and A7 (213.2 J/mm) as seen on the hardness coupon; however, these defects were machined away when fabricating the tensile specimens as discussed in section 3.7.

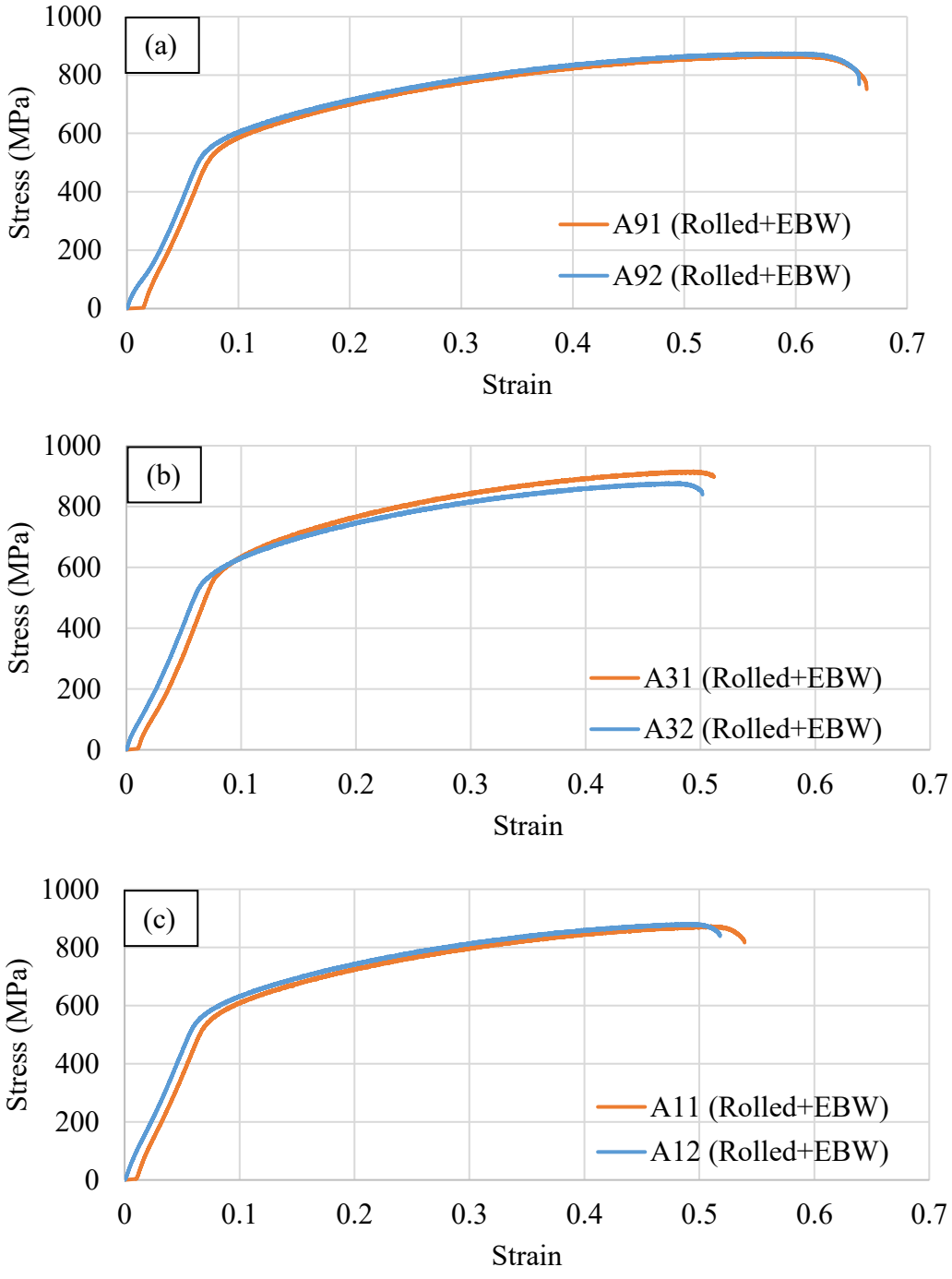

Figure 4.9 Tensile test stress-strain curves for (a) sample A9 (180.4 J/mm) (b) sample A3 (249.8 J/mm) (c) sample A1 (295.3 J/mm) and their replicates

Note: The curves are shifted horizontally for illustration purposes.

Table 4.3 Tensile properties (at room temperature) of rolled IN718 after EBW

Sample #	Heat input (J/mm)	Tensile strength (MPa)	Yield strength (MPa)	Young Modulus (GPa)	Elongation ε_f (%)	Toughness (J/mm^3 $\times 10^{-3}$)
A91	180.4	867	502	8.9	65	472
A92	180.4	875	517	8.8	66	478
A81	196.8	861	497	8.8	64	457
A82	196.8	857	488	8.9	61	435
A61	209.6	827	451	8.9	57	382
A62	209.6	846	470	9.2	61	431
A71	213.2	851	478	8.9	62	447
A72	213.2	852	485	9.0	61	431
A51	228.6	860	503	8.9	55	388
A52	228.6	846	470	9.0	58	405
A41	247.6	857	504	9.1	51	357
A42	247.6	876	511	8.9	52	365
A31	249.8	916	571	9.0	51	374
A32	249.8	878	544	8.8	50	357
A21	272.6	894	555	8.8	50	361
A22	272.6	885	540	8.9	51	368
A11	295.3	874	527	8.9	53	379
A12	295.3	881	534	9.0	52	373

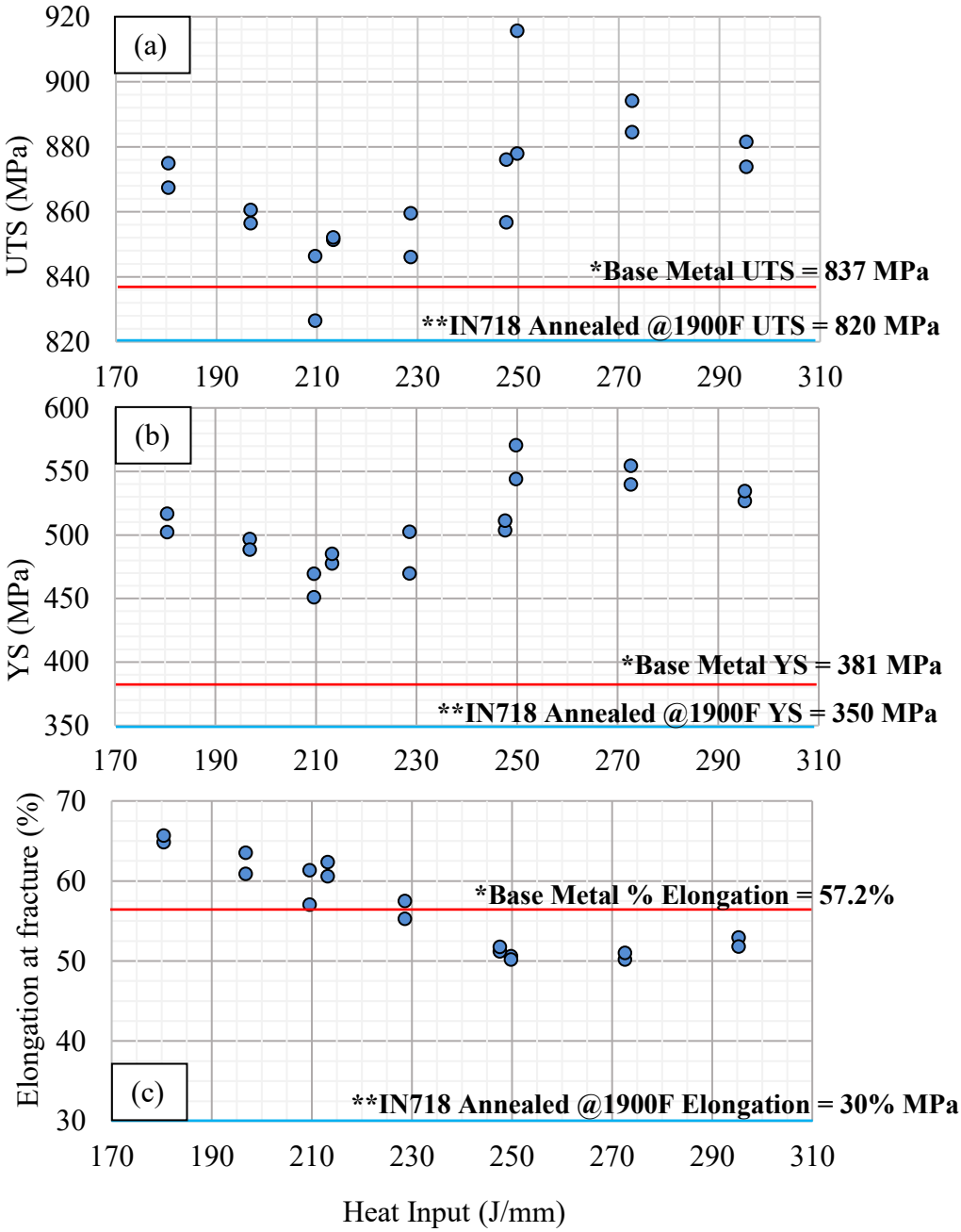

Figure 4.10 Effect of heat input on (a) ultimate tensile strength, S_u (b) 0.2% yield strength, S_y (c) elongation at fracture (ε_f)

*as-received material specification: Bolen WE. Certified Materials Test Report, Huntington Alloys Corporation, West Virginia; 2019 [4]

**Physical metallurgy of alloy 718, DMIC Report 217, 1965 [8]

Figure 4.9 shows consistent stress-strain curves for samples A9 (180.4 J/mm), A3 (249.8 J/mm), A1 (295.3 J/mm), and their replicates. Similar consistency was found for other identical pairs. Table 4.3 mentions the obtained mechanical properties of all tested EBW samples. The effect of heat input on UTS, YS, and % elongation at fracture can be understood through Figure 4.10. Although the experimental setup is different from the true welding of two separated parts, each tensile specimen is with a full penetration weld that separates the two halves of a specimen. The tensile test in this would represent an ideal case of welding with complete penetration, precise machining, and no misalignment of welded parts. The stress-strain curves of all other samples are documented in Appendix C.

From the results of the tensile test, it was observed that:

- Recorded ultimate tensile strength and yield strength values did not show a strong correlation with the heat input. With an exception of one sample (A61, 209.6 J/mm), the tensile strengths of all samples exceeded the material UTS specification of 837 MPa. The yield strengths of all samples were also more than the base metal YS specification of 381 MPa.
- The elongation of EBW specimens, however, decreased below the specification of 57.2% when the heat input values were higher than 225 J/mm. Perhaps a higher temperature and slow cooling rate associated with higher heat input promoted the Nb segregation and formation of brittle Laves particles in the

microstructure, therefore, degrading the ductility of welded samples. Similar facts were presented by Mei et al. (2016) and Agilan et al. (2014).

- Although the ductility of samples with heat input > 225 J/mm was lower than the material specification, the tensile strength for such samples was found to be more than the material specification. While it is suspected to have a higher % of brittle particles in the fusion zone at a higher heat input, lower thermal stresses within the fusion zone helped to maintain the strength in those cases.
- Material toughness, represented by the area under the stress-strain curve (ref. Figure 4.11), also reduced with increasing heat input (Table 4.3). This further supported the hypothesis that brittle particles might be the cause when welding at high heat input conditions.

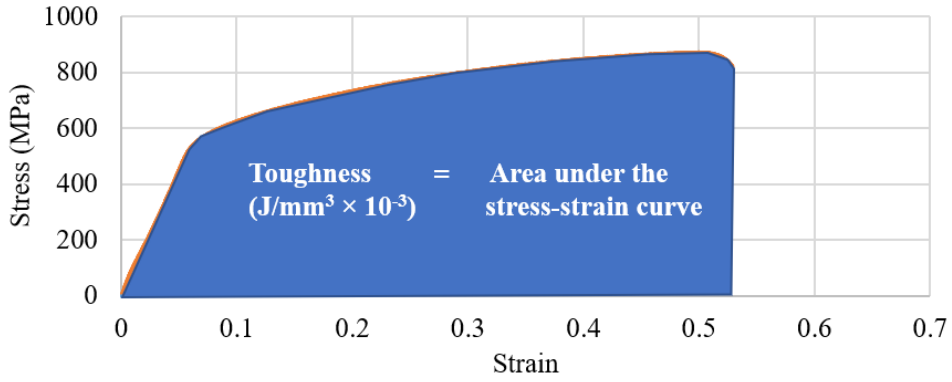

Figure 4.11 Toughness calculation from the stress-strain curve

4.4. Fractographs and Microstructure

The fracture surfaces were observed with both optical microscope and SEM. The microstructure and the quantitative element analysis (by EDS system) helped to explain

the measured ductility results. On each heat input level, two tensile specimens were labeled in the form AX1 and AX2 (for example, the A2 weld coupon was cut to produce two tensile specimens A21 and A22). The samples A21 (272.6 J/mm), A31 (249.8 J/mm) broke through the weld zone while samples A81 (196.8 J/mm) and A91 (180.4 J/mm) broke through base metal away from the weld zone after performing the tensile test. The fractured surfaces of samples A31 (249.8 J/mm) and A91 (180.4 J/mm) were observed under the optical microscope (ref. Figure 4.14, Figure 4.13). The fracture surface microstructure of samples A21 (272.6 J/mm) and A81 (196.8 J/mm) was examined by SEM (ref. Figure 4.15, Figure 4.16) and element composition analysis of distinctive sites on the fracture surfaces of A21 (272.6 J/mm) and A81 (196.8 J/mm) further explicated underlying fracture characteristics of each (ref. Figure 4.17, Figure 4.18). Figure 4.12 illustrates a typical tensile specimen with the orientation of coordinates.

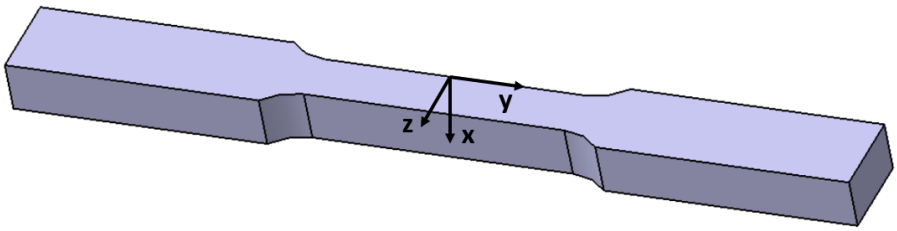

Figure 4.12 Typical tensile specimen with coordinates for illustration

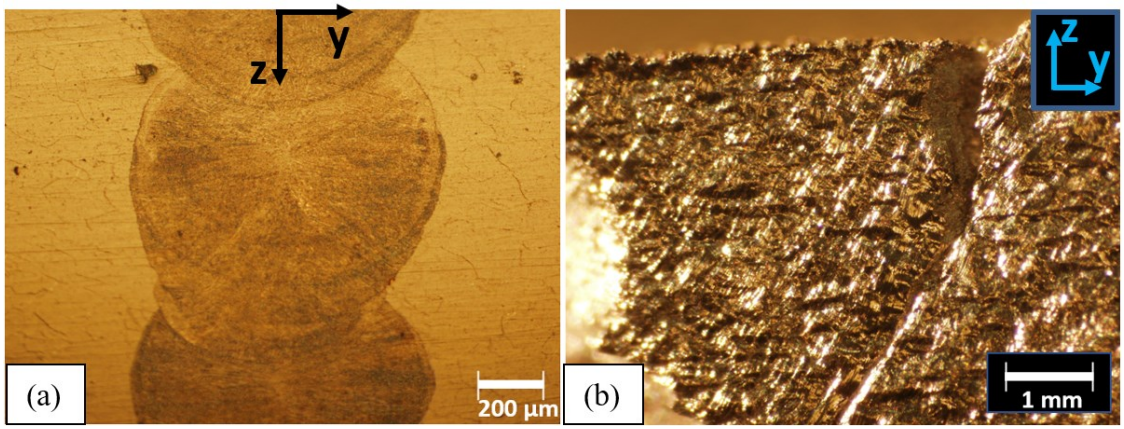

Figure 4.13 OM fractographs of the sample A91 (180.4 J/mm) after tensile testing (a) The crack-free EBW bead, away from fracture zone observed after etching (b) Ductile shear bands in fracture zone on sample A9, away from EBW bead

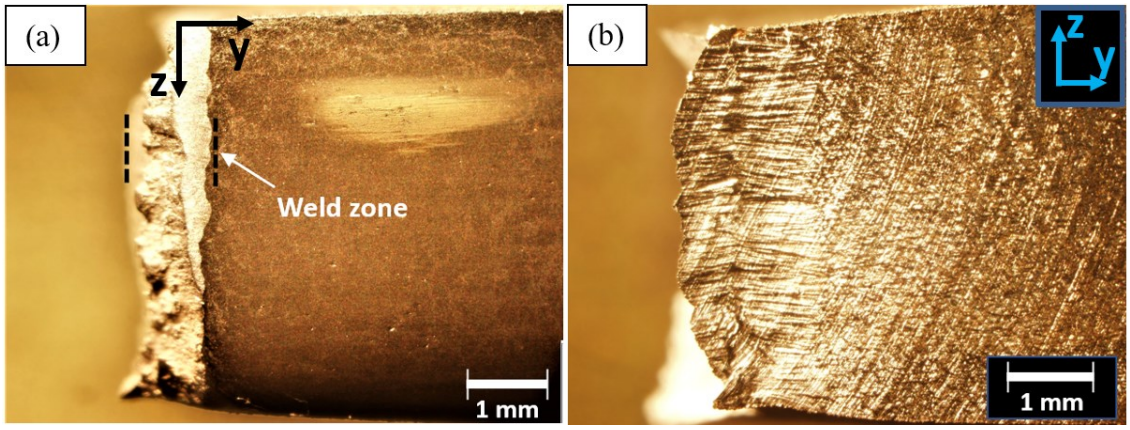

Figure 4.14 OM fractographs of the sample A31 (249.8 J/mm) after tensile testing (a) Fracture through the weld zone observed after etching (b) Fracture zone with secondary cracks perpendicular to loading direction

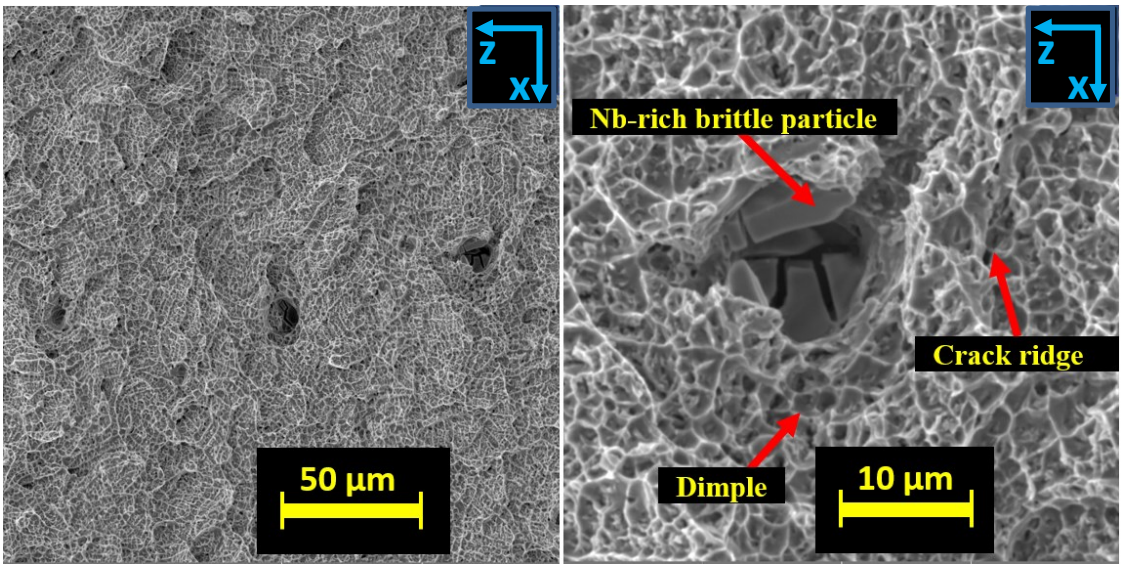

Figure 4.15 SEM fractography of the sample A21 (272.6 J/mm) that broke through the weld zone

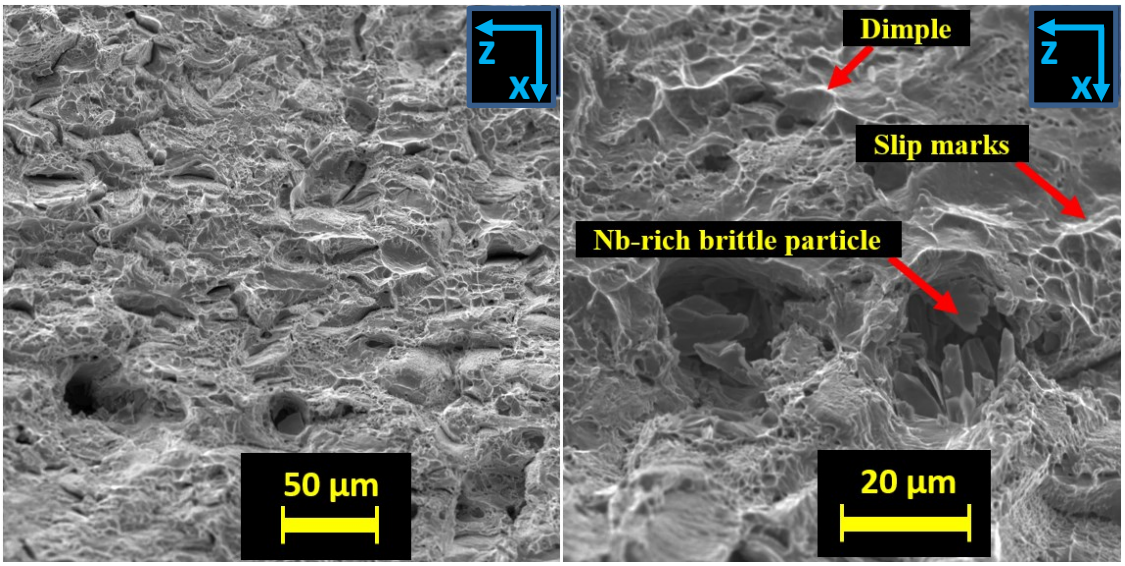

Figure 4.16 SEM fractography of the sample A81 (196.8 J/mm) that broke through the base metal outside weld zone

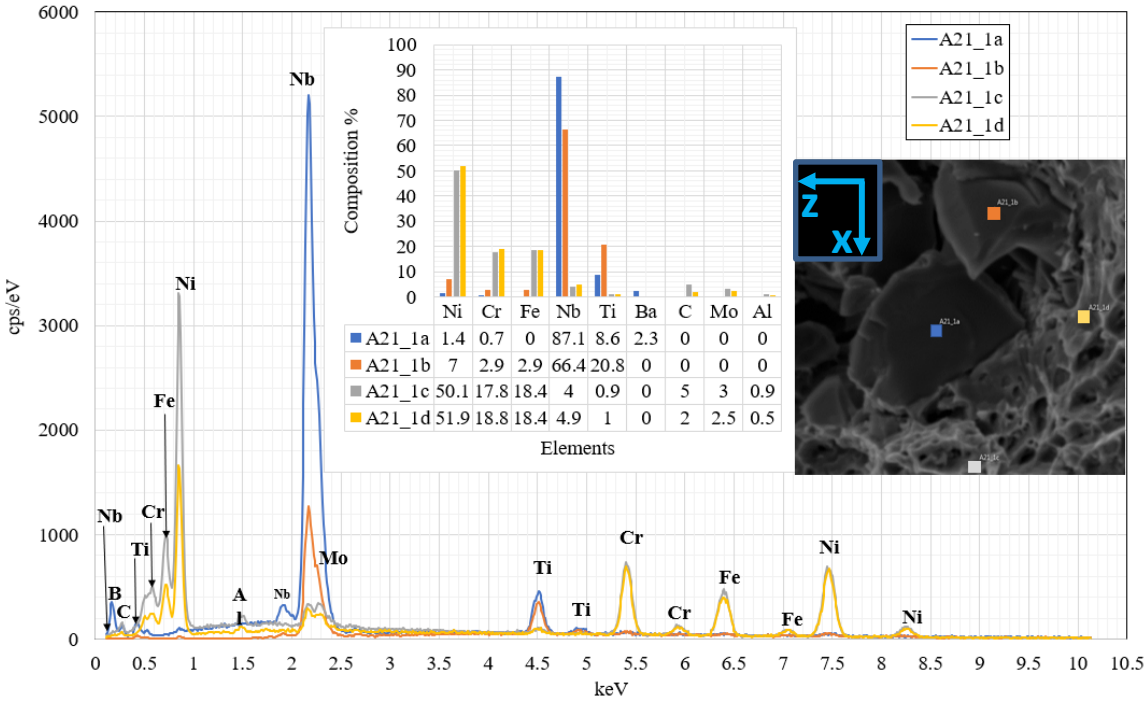

Figure 4.17 Energy Dispersive Spectroscopy of distinctive locations on the fracture surface of the sample A21 (272.6 J/mm) that broke through the weld zone

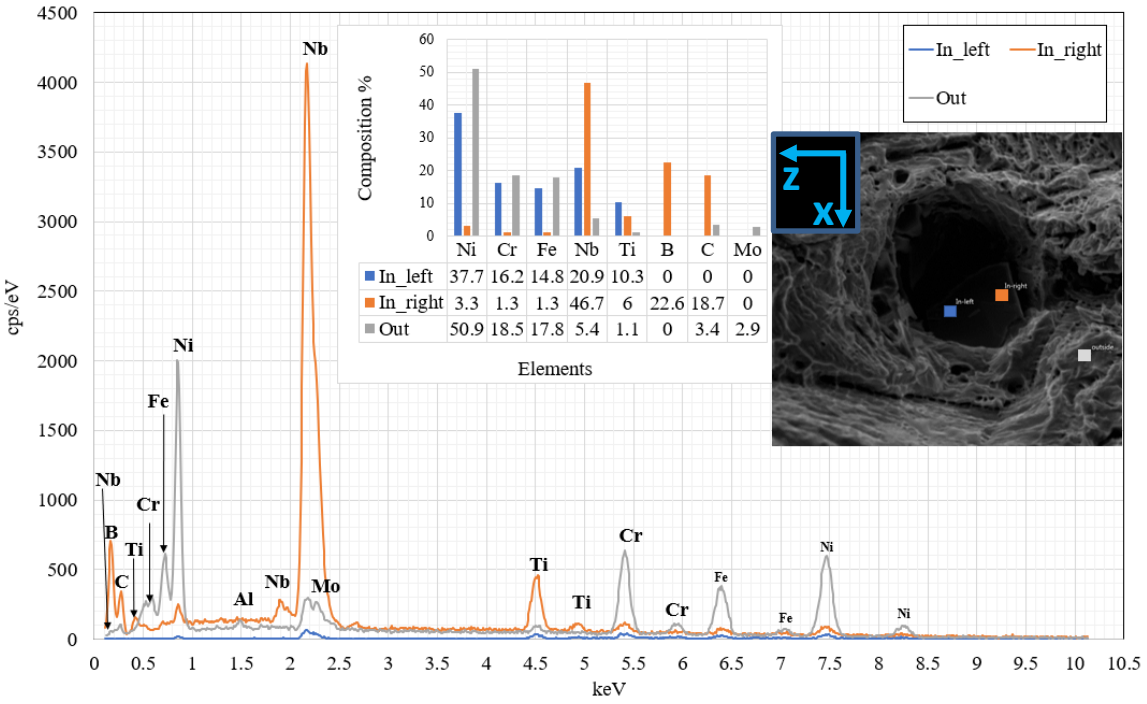

Figure 4.18 Energy Dispersive Spectroscopy of distinctive locations on the fracture surface of the sample A81 (196.8 J/mm) that broke through the base metal outside weld zone

From the results of fractographic analysis mentioned above, the following was observed:

- Relatively brittle sample A31 (249.8 J/mm, ε_f =50%) fractured at the weld while the more ductile sample A91 (180.4 J/mm, ε_f =65%) fractured away from the weld. The weld bead of sample A91 (180.4 J/mm) contains no visible cracks even when viewing at a high magnification which shows good weld strength. A series of shear bands near the fractured surface, located away from the weld zone and oriented about 45° to the tensile loading direction, suggested ductile fracture. The results validated the high ductility observed for sample A91 (180.4 J/mm) in the tensile testing.
- The opposites were found on sample A31 (249.8 J/mm) where cracks were initiated in the fusion zone and propagated through the HAZ. Other secondary cracks, oriented about 90° to the tensile loading direction, were also visible which supported comparatively less ductile behavior for the sample A31 (249.8 J/mm). These facts explain the low ductility of samples when EBW'ed at high heat input greater than 225 J/mm.
- Recall that cooling of IN718 leads to:

  Liquid IN718 → gamma (γ, γ', γ") + NbC + Laves (4)

  The EDS quantitative spectral analysis revealed Nb-rich particles for both sample A81 (ε_f =64%) and A21 (ε_f = 50%). The presence of carbon suggested the formation of carbide at distinctive sites on the fracture surfaces. The observed carbon composition on the base metal matrix of sample A81 (196.8 J/mm)

showed a spike of 18.7% which indicates possible carbon impurities. The carbon composition in the fusion zone of sample A21 (272.6 J/mm) was found in the range of 2-5%. Nb concentration in the fusion zone of sample A21 (272.6 J/mm) was considerably higher than the base metal of sample A81 (196.8 J/mm) which on average were 70% and 30% respectively. In EBW and selective laser melting, the melting and cooling of molten IN718 forms the dendrite solid solution γ phase, niobium carbide (NbC), and the Laves phase [13,21,28,29,30]. The Nb-rich interdendritic Laves phase, forming due to slow cooling of molten IN718 were present in the weld zone when cooled from a higher weld temperature due to high heat input. Such brittle phases would be responsible for comparatively less ductile fracture characteristics of sample A21. This supports the arguments presented by Mei et al. (2016) and Agilan et al. (2014). Excess of boron (22.6%) found at one of the locations on the fracture surface of sample A81 indicates probable impurities in the base metal. Zhou et al. (2008) stated that boron present in the range of 0.003-0.024% in conventionally manufactured IN718 is beneficial to rupture life, while boron concentration >0.024% negatively affects the rupture life.

- The microstructure of fracture surfaces by SEM showed distinctive sites of brittle Nb-rich carbides for both sample A81 (196.8 J/mm) and A21 (272.6 J/mm). Dimple morphology and slip marks in the base metal matrix for the sample indicated ductile behavior for sample A81 (196.8 J/mm). Although fine grains and dimples were observed for the sample A21 (272.6 J/mm); crack ridges and

heavy Nb concentration (found in EDS analysis) signified comparatively less ductile characteristics.

Additional optical microscope fractography results for samples A91 (180.4 J/mm) and A31 (249.8 J/mm) are documented in Appendix D. It also contains SEM fractographs of sample A91 (180.4 J/mm).

5. CONCLUSIONS AND RECOMMENDATIONS

Single-pass electron beam welding of thick rolled Inconel 718 (bead on the plate) without oscillations was performed. This study showed:

1. Voids can be formed at the EBW bead bottom for deep, narrow, and partial penetrations when welded at high beam power at high welding speed. The only two EBW'ed samples A4 (247.6 J/mm) and A7 (213.2 J/mm) contained root-voids out of nine samples in this study. They were welded at beam power of 3250 W (65 mA, 50 kV) and welding speed > 780 mm/min. At high welding speed and high power beam; faster cooling rates, and inadequate molten metal sidewalls promote such defects at the bottom of the weld.
2. All samples but one exhibited higher tensile strength than the specification for rolled IN718 (837 MPa). The yield strength results were above the base metal specification (381 MPa). The ductility also exceeded the specification except when joining at heat input above 225 J/mm. At high heat input, a slower cooling in the molten puddle allows weakening phases to form and degrade material ductility.
3. The heat inputs dictate the fracture behavior of EBW'ed IN718. A low heat input resulted in strong welds since the ductile fracture surface occurred in the base

---

1. The content of this section has been published under the reference – "Patel, V., Sali, A., Hyder, J., Corliss, M., Hyder, D., & Hung, W. (2020). Electron Beam Welding of Inconel 718 Electron Beam Welding of Inconel 718. *Procedia Manufacturing*, *48*(2019), 428–435. https://doi.org/10.1016/j.promfg.2020.05.065"
2. The authors retain full rights to the content for the academic dissertation. The details can be found: https://www.elsevier.com/about/policies/copyright#Author-rights

material and outside of the weld zone. In contrast, a high heat input resulted in (comparatively) brittle fracture inside the weld zone. The brittleness was perhaps caused by the presence of the Nb-rich Laves phase formed in the weld.

3. For single-pass unoscillated EBW of rolled IN718, practical trade-offs include the selection of heat input level according to the penetration depth requirement. In the case of EBW of rolled IN718, a heat input in the range of 180-300 J/mm can produce the corresponding weld penetration in the range of 9.9-13.4 mm. Performing EBW on both sides can help to weld thicker samples, but the re-melting of the base metal affects desired grain structure and reduces hardness. Heat input in the range of 180-225 J/mm can result in better ductility for rolled IN718. A lower welding speed close to 660 mm/min can reduce thermal stress and cracks in the weld zone but it can promote the segregation of weakening phases in the weld zone and hence reduced ductility. The ultimate tensile strength of the EBW'ed rolled IN718 was found in the range of 820-910 MPa with heat input in the range of 180-300 J/mm. The strength didn't show any relation with heat input in the stated range. Selection of beam current and welding speed can be made based on the requirements of strength, ductility, and weld depth.

The future work can be directed towards improving the weld quality further and extending the research to implement deep EBW on IN718 SLM parts. The following recommendations are proposed:

1. Executing EBW on the SLM'ed IN718 samples with the same EBW process parameters used in this study to compare the results in both cases.
2. Implementing elliptical or circular oscillations while exercising EBW on the surface. It can help to improve strength and ductility. The oscillations can reduce thermal gradients in the weld zone and dissolve Nb segregation with a higher cooling rate at the same heat input. The reduction in thermal stresses might reduce microfissuring as well at a given heat input thus improving the weld quality.

REFERENCES

[1] Agilan, M., Venkateswaran, T., Sivakumar, D., & Pant, B. (2014). Effect of Heat Input on Microstructure and Mechanical Properties of Inconel-718 EB Welds. *Procedia Materials Science*, *5*, 656–662. https://doi.org/10.1016/j.mspro.2014.07.312

[2] Akca, E., & Gürsel, A. (2015). A Review on Superalloys and IN718 Nickel-Based INCONEL Superalloy. *Periodicals of Engineering and Natural Sciences (PEN)*, *3*(1). https://doi.org/10.21533/pen.v3i1.43

[3] ASM Specialty Handbook: Nickel, Cobalt, and Their Alloys J.R. Davis, editor, p 230-234, DOI:10.1361/ncta2000p230

[4] Bolen WE. Certified Materials Test Report, Huntington Alloys Corporation, West Virginia; 2019

[5] Devaux, A., Nazé, L., Molins, R., Pineau, A., Organista, A., Guédou, J. Y., Uginet, J. F., & Héritier, P. (2008). Gamma double prime precipitation kinetic in Alloy 718. *Materials Science and Engineering A*, *486*(1–2), 117–122. https://doi.org/10.1016/j.msea.2007.08.046

[6] Gao, P., Zhang, K. F., Zhang, B. G., Jiang, S. S., & Zhang, B. W. (2011). Microstructures and high-temperature mechanical properties of electron beam welded Inconel 718 superalloy thick plate. *Transactions of Nonferrous Metals Society of China (English Edition)*, *21*(SUPPL. 2). https://doi.org/10.1016/S1003-6326(11)61598-7

[7] Gao, Y., Zhang, D., Cao, M., Chen, R., Feng, Z., Poprawe, R., Schleifenbaum, J. H., & Ziegler, S. (2019). Effect of δ phase on high-temperature mechanical performances of Inconel 718 fabricated with SLM process. *Materials Science and Engineering A*, *767*. https://doi.org/10.1016/j.msea.2019.138327

[8] H.J. Wagner and A.M. Hall. (1965). Physical Metallurgy of Alloy 718. Defense Metals Information Center, Report 217.

[9] Hong, J. K., Park, J. H., Park, N. K., Eom, I. S., Kim, M. B., & Kang, C. Y. (2008). Microstructures and mechanical properties of Inconel 718 welds by CO2 laser welding. *Journal of Materials Processing Technology*, *201*(1–3), 515–520. https://doi.org/10.1016/j.jmatprotec.2007.11.224

[10] Huang, C. A., Wang, T. H., Lee, C. H., & Han, W. C. (2005). A study of the heat-affected zone (HAZ) of an Inconel 718 sheet welded with electron-beam welding (EBW). *Materials Science and Engineering A*, *398*(1–2), 275–281. https://doi.org/10.1016/j.msea.2005.03.029

[11] Janaki Ram, G. D., Venugopal Reddy, A., Prasad Rao, K., & Madhusudhan Reddy, G. (2005). Microstructure and mechanical properties of Inconel 718 electron beam welds. *Materials Science and Technology*, *21*(10), 1132–1138. https://doi.org/10.1179/174328405X62260

[12] Khairallah SA, Anderson AT, Rubenchik A, King WE. Laser powder-bed fusion additive manufacturing: Physics of complex melt flow and formation mechanisms of pores, spatter, and denudation zones; 2016, 108:36-45

[13] Knorovsky GA, Cieslak MJ, Headley TJ, Romig AD, and Hammetter WF. Inconel 718: A Solidification Diagram. Metallurgical Transactions A; 1989: 20A, 2149-2158
[14] Liu, C., & He, J. (2016). Numerical analysis of fluid transport phenomena and spiking defect formation during vacuum electron beam welding of 2219 aluminum alloy plate. Vacuum, 132, 70–81. https://doi.org/10.1016/j.vacuum.2016.07.033
[15] Luo, X., Yoshihara, S., Shinozaki, K., Kuroki, H., & Shirai, M. (2000). Theoretical analysis of grain boundary liquation in the heat-affected zone of Inconel 718 alloy. Study of laser weldability of ni-base superalloys (3rd report). *Welding International*, *14*(11), 865–873. https://doi.org/10.1080/09507110009549284
[16] Madhusudhana Reddy, G., Srinivasa Murthy, C. v., Srinivasa Rao, K., & Prasad Rao, K. (2009). Improvement of mechanical properties of Inconel 718 electron beam welds-influence of welding techniques and post-weld heat treatment. *International Journal of Advanced Manufacturing Technology*, *43*(7–8), 671–680. https://doi.org/10.1007/s00170-008-1751-7
[17] Mei, Y., Liu, Y., Liu, C., Li, C., Yu, L., Guo, Q., & Li, H. (2016). Effect of base metal and welding speed on fusion zone microstructure and HAZ hot-cracking of electron-beam welded Inconel 718. *Materials and Design*, *89*, 964–977. https://doi.org/10.1016/j.matdes.2015.10.082
[18] Muralidharan, B. G., Shankar, V., & Gill, T. (1996). *It 19800144 into r-« en Weldability of Inconel 718-A Review*.
[19] Norrish J. Advanced Welding Processes. *Cambridge: Woodland Publishing Limited*; 2006, 157-164
[20] OdabaşI, A., Ünlü, N., Göller, G., & Eruslu, M. N. (2010). A study on laser beam welding (LBW) technique: Effect of heat input on the microstructural evolution of superalloy Inconel 718. *Metallurgical and Materials Transactions A: Physical Metallurgy and Materials Science*, *41*(9), 2357-2365.https://doi.org/10.1007/s11661-010-0319-y
[21] P.J. Zhou, J.J. Yu, X.F. Sun, H.R. Guan, Z.Q. Hu. The role of boron on a conventional nickel-based superalloy, Materials Science and Engineering: A, Volume 491, Issues 1–2, 2008, Pages 159-163, ISSN 0921-5093, https://doi.org/10.1016/j.msea.2008.02.019.
[22] Radavich JF. Electron metallography of alloy 718. Superalloys 718, 625, 706, and Various Derivatives. The Minerals, Metals & Materials Society; 1997, 17-26.
[23] Rahim, E., Warap, N., & Mohid, Z. (2015). Thermal-Assisted Machining of Nickel-based Alloy. In *Superalloys*. InTech. https://doi.org/10.5772/61101
[24] Raza, T., Andersson, J., & Svensson, L. E. (2018). Varestraint weldability testing of additive manufactured alloy 718. *Science and Technology of Welding and Joining*, *23*(7), 606–611. https://doi.org/10.1080/13621718.2018.1437338
[25] Sajun Prasad, K., Panda, S. K., Kar, S. K., Sen, M., Murty, S. V. S. N., & Sharma, S. C. (2017). Microstructures, Forming Limit and Failure Analyses of Inconel 718 Sheets for Fabrication of Aerospace Components. *Journal of Materials Engineering and Performance*, *26*(4), 1513–1530. https://doi.org/10.1007/s11665-017-2547-4

[26] Sharma, S. K., Agarwal, P., & Majumdar, J. D. (2017). Studies on Electron Beam Welded Inconel 718 Similar Joints. *Procedia Manufacturing*, *7*, 654–659. https://doi.org/10.1016/j.promfg.2016.12.097
[27] Song, K. H., Kim, W. Y., & Nakata, K. (2013). Investigation of microstructure and mechanical properties on surface-modified Inconel 718 Alloy. *Materials Transactions*, *54*(10), 2032–2036. https://doi.org/10.2320/matertrans.M2013096
[28] Trosch T, Strößner J, Völkl R, Glatzel U. Microstructure and mechanical properties of selective laser melted Inconel 718 compared to forging and casting. Materials Letters; 2016, 164: 428-431. 164
[29] Tucho WM, Cuvillier P, Sjolyst-Kverneland A, and Hansen V. Microstructure and hardness studies of Inconel 718 manufactured by selective laser melting before and after solution heat treatment. Materials Science and Engineering A; 2017, 689: 220-232
[30] Wang Z, Guan K, Gao M, Li X, Chen X, and Zeng X. The microstructure and mechanical properties of deposited-IN718 by selective laser melting; Journal of Alloys and Compounds; 2012, 513: 518-523
[31] Xia, C., Zhao, M., Sun, W., Li, H., & Liu, P. (2018). microstructure and properties of 3D printed Inconel 718 joint brazed with BNi-2 amorphous filler metal. *Materials Research*, *22*(1). https://doi.org/10.1590/1980-5373-MR-2018-0348

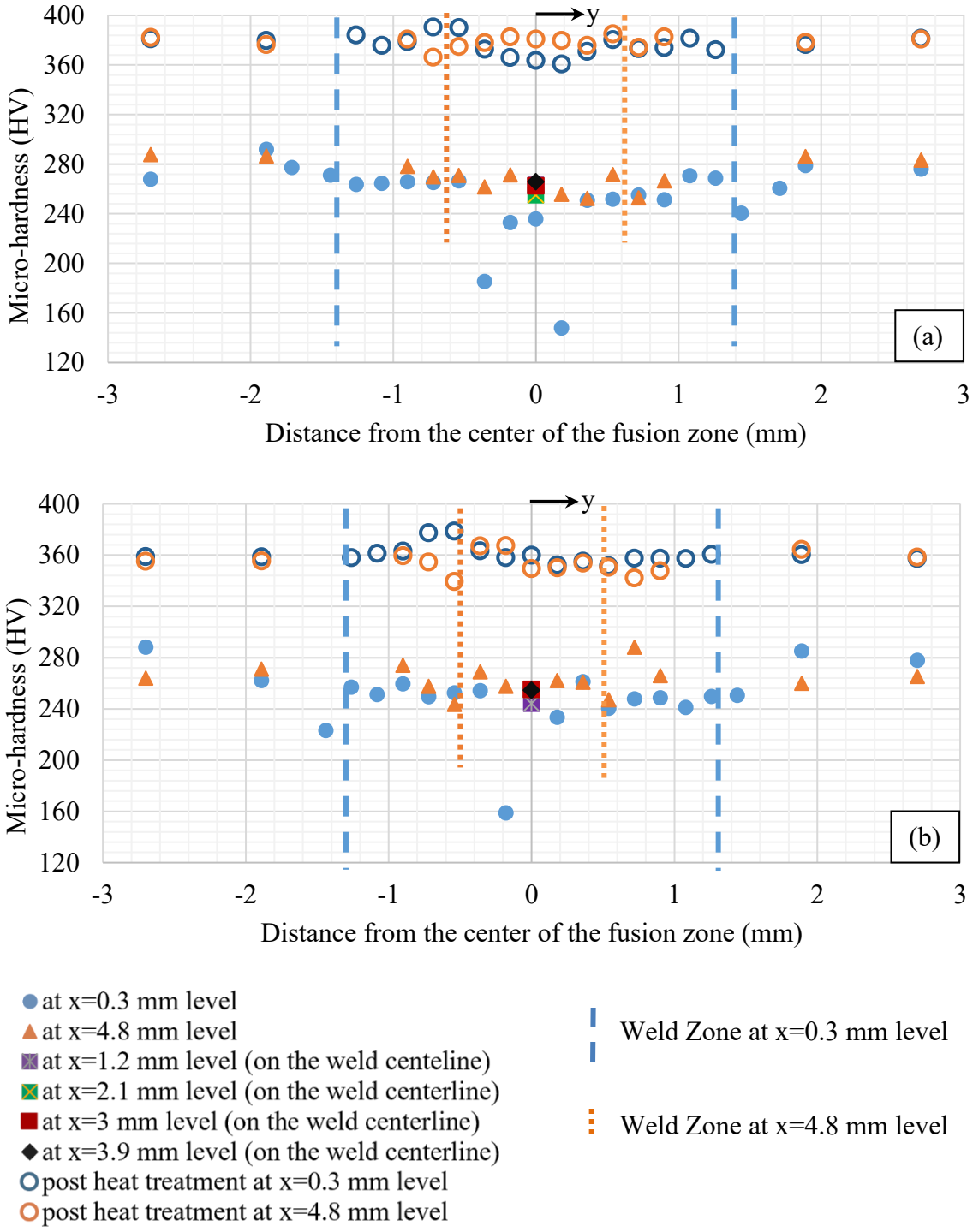

Figure A.1 Microhardness distribution of EBW'ed sample before and after heat treatment (a) sample A2 (272.6 J/mm) (b) sample A3 (249.8 J/mm)

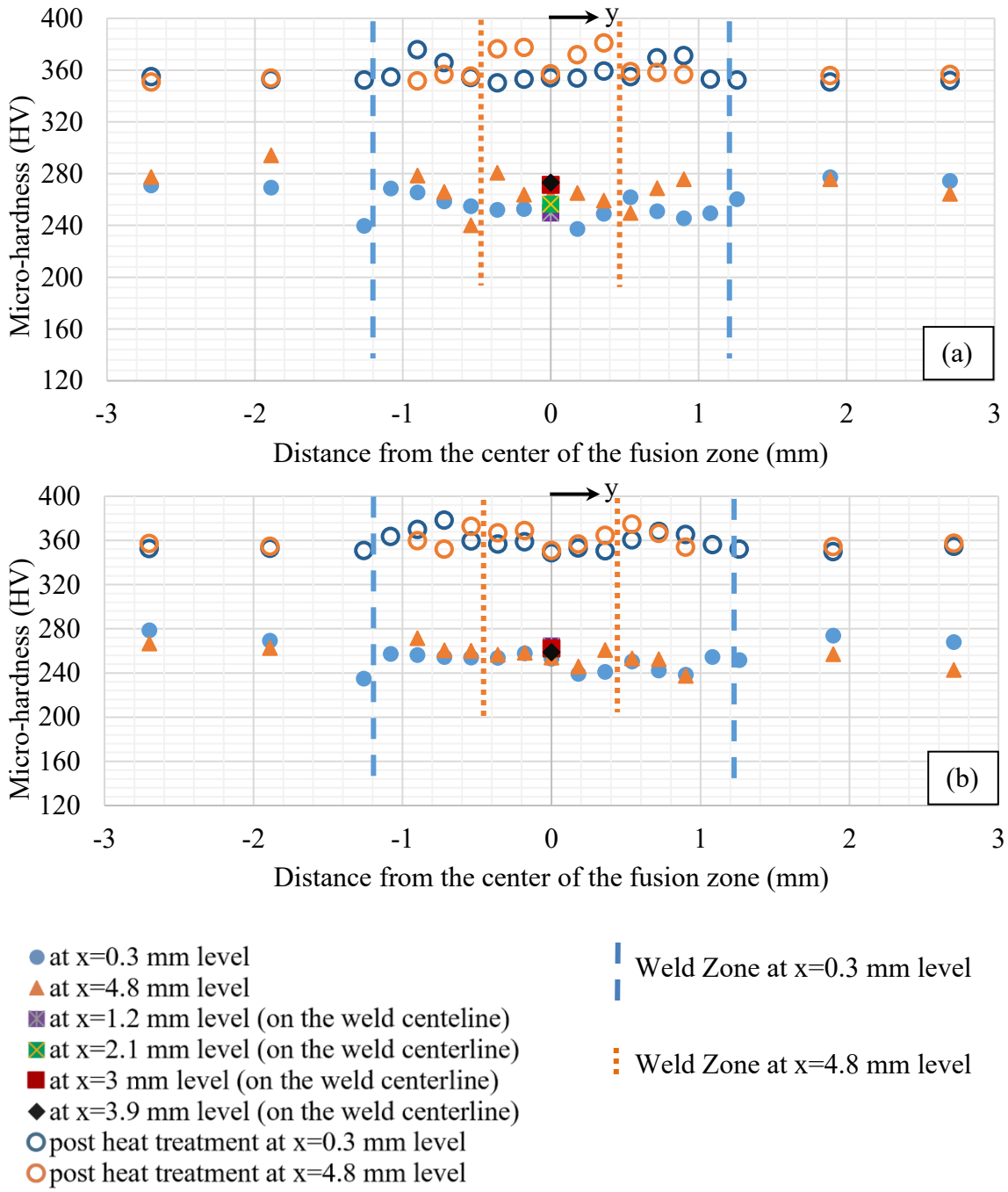

Figure A.2 Microhardness distribution of EBW'ed sample before and after heat treatment (a) sample A4 (247.6 J/mm) (b) sample A5 (228.6 J/mm)

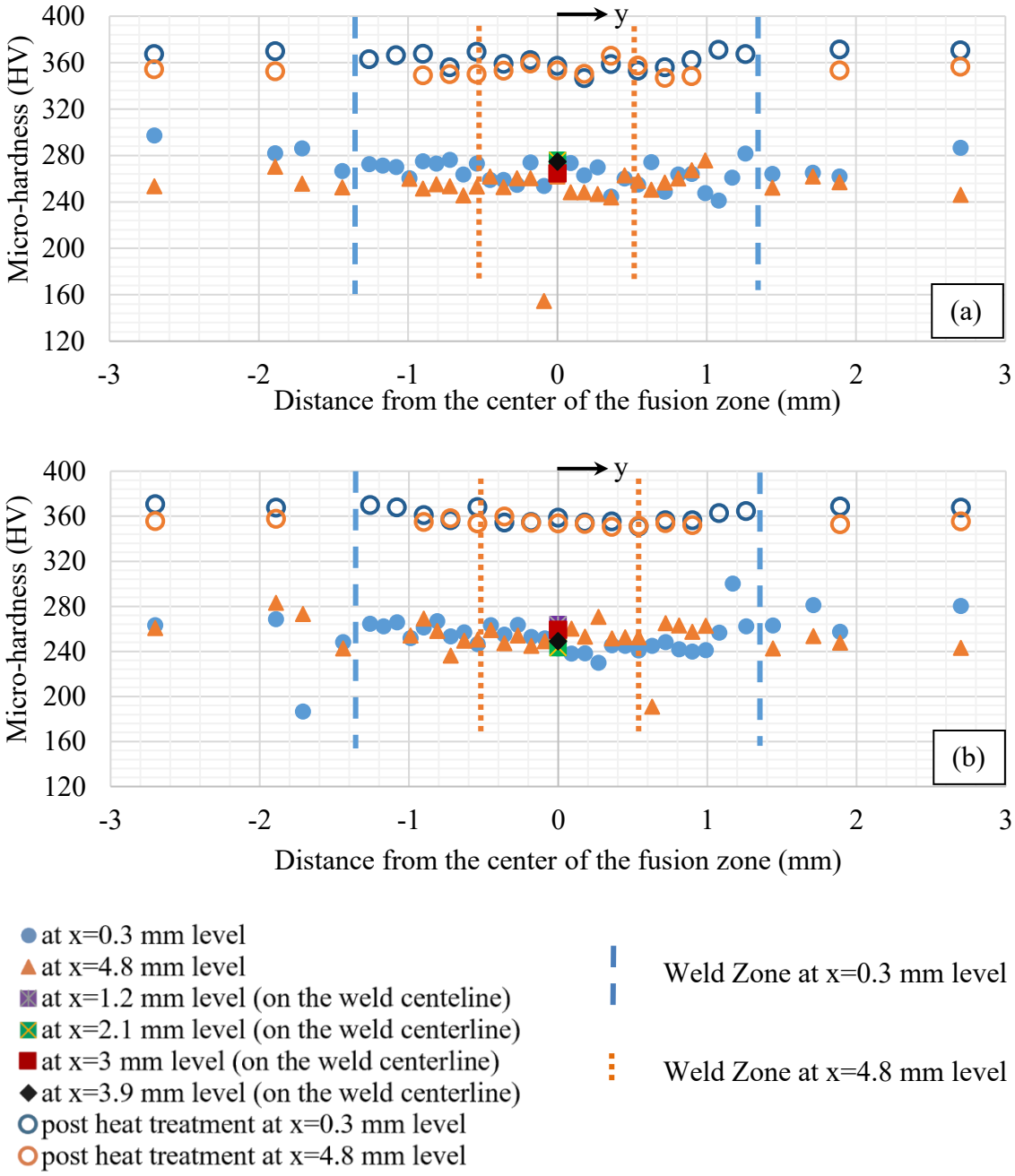

Figure A.3 Microhardness distribution of EBW'ed sample before and after heat treatment (a) sample A7 (213.2 J/mm) (b) sample A8 (196.8 J/mm)

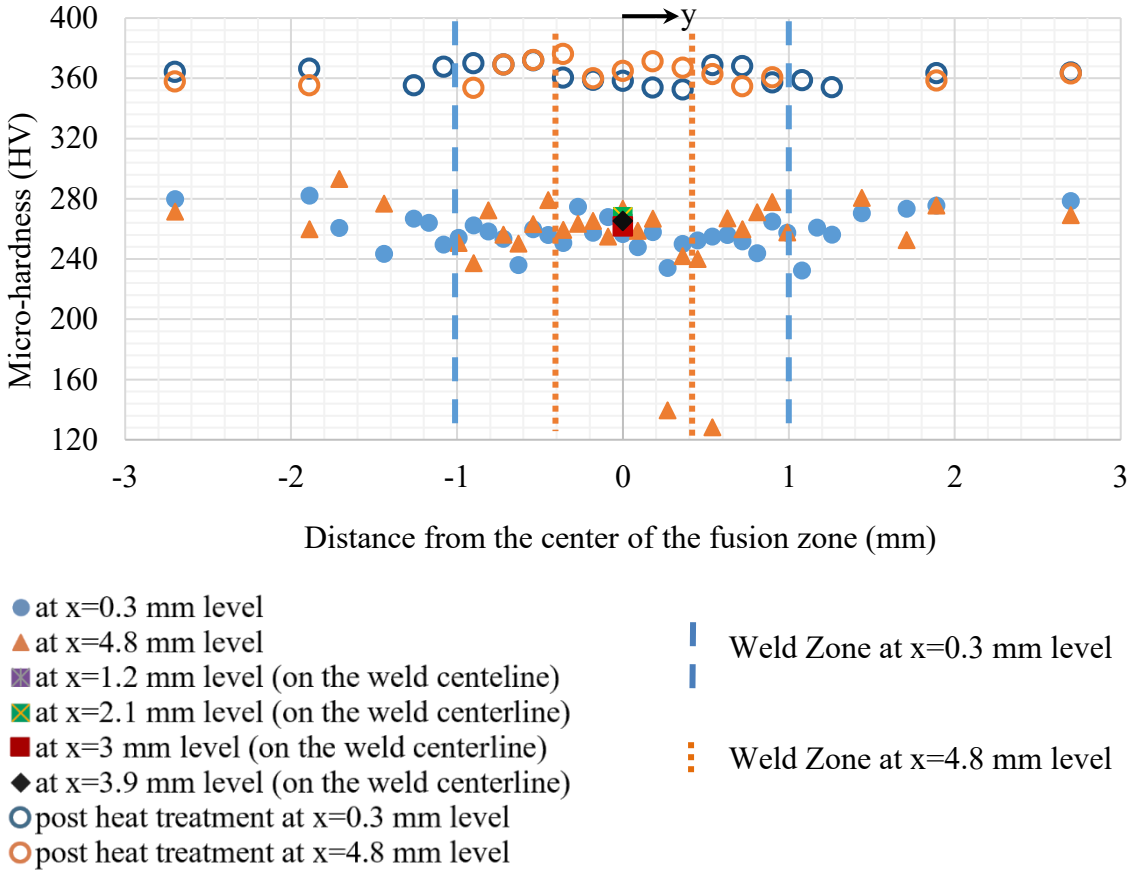

Figure A.4 Microhardness distribution of EBW'ed sample A6 (209.6 J/mm) before and after heat treatment

APPENDIX B: STATISTICAL ANALYSIS

Table B.1 ANOVA for fusion zone area vs welding speed and beam current

Source	DF	Adj SS	Adj MS	F-Value	P-Value
Model	4	49.7687	12.4422	148.23	0.000
Linear	4	49.7687	12.4422	148.23	0.000
1000/Welding Speed (mm/min)	2	38.2010	19.1005	227.56	0.000
Beam Current (mA)	2	11.5676	5.7838	68.91	0.000
Error	13	1.0912	0.0839		
Lack-of-Fit	4	1.0801	0.2700	219.94	0.000
Pure Error	9	0.0111	0.0012		
Total	17	50.8599			

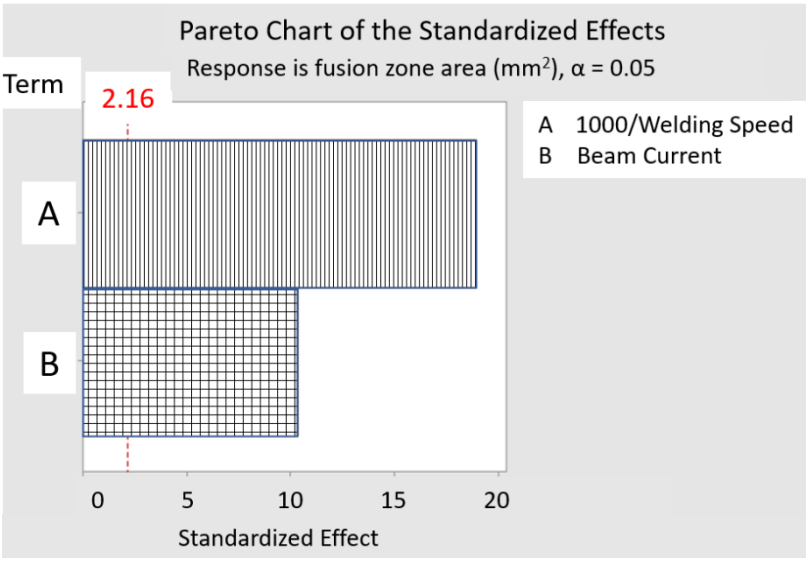

Figure B.1 Parameter effect analysis for fusion zone area

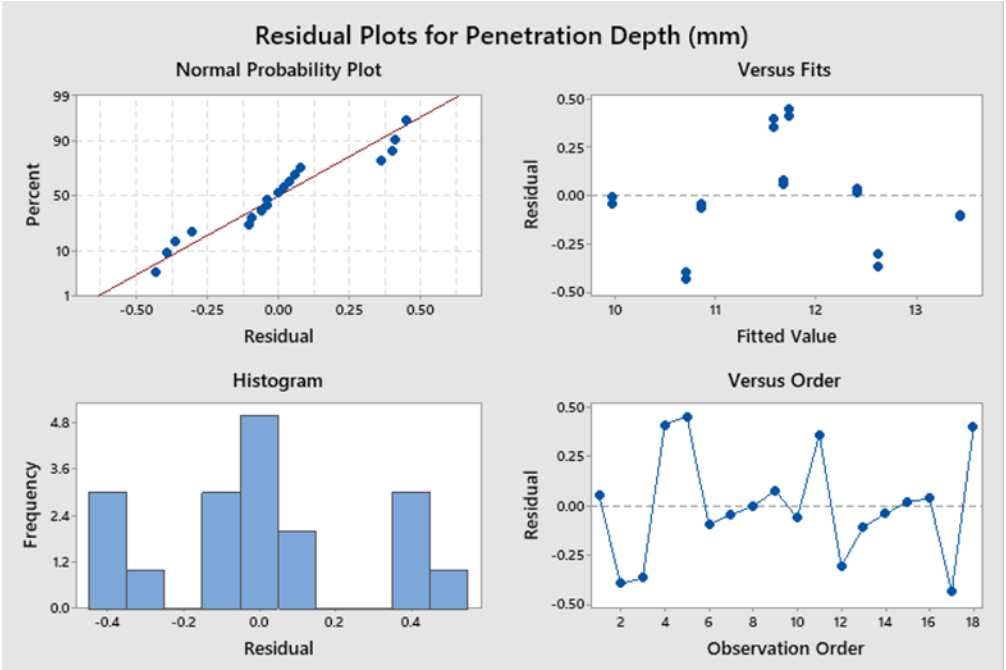

Figure B.2 Residual plots for the penetration depth by a linear model

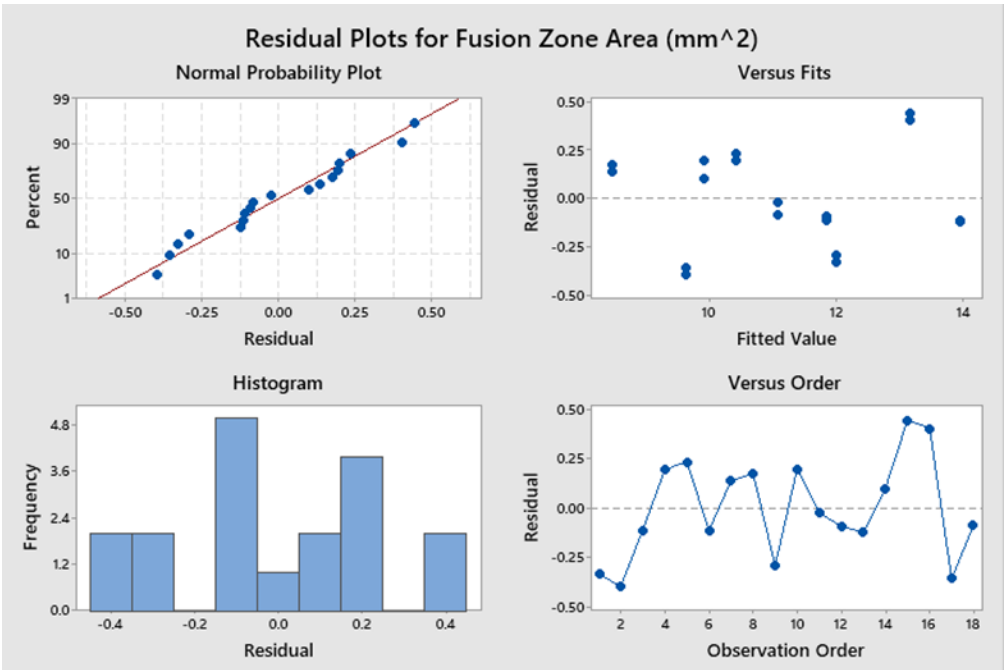

Figure B.3 Residual plots for the fusion zone area by a linear model

APPENDIX C: TENSILE TEST STRESS-STRAIN CURVES

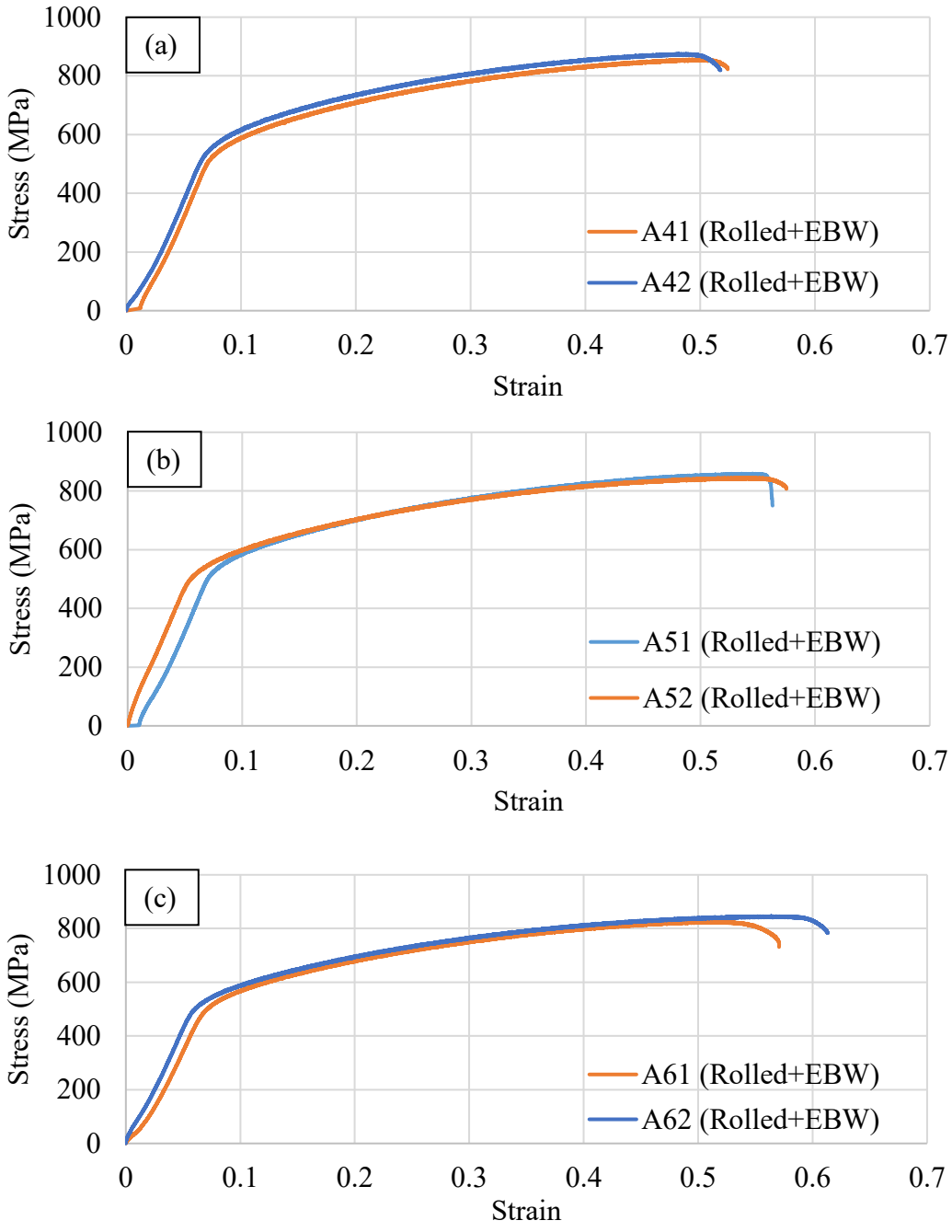

Figure C.1 Tensile test stress-strain curves for (a) sample A4 (247.6 J/mm) (b) sample A5 (228.6 J/mm) (c) sample A6 (209.6 J/mm) and their replicates

Note: The curves are shifted horizontally for illustration purposes.

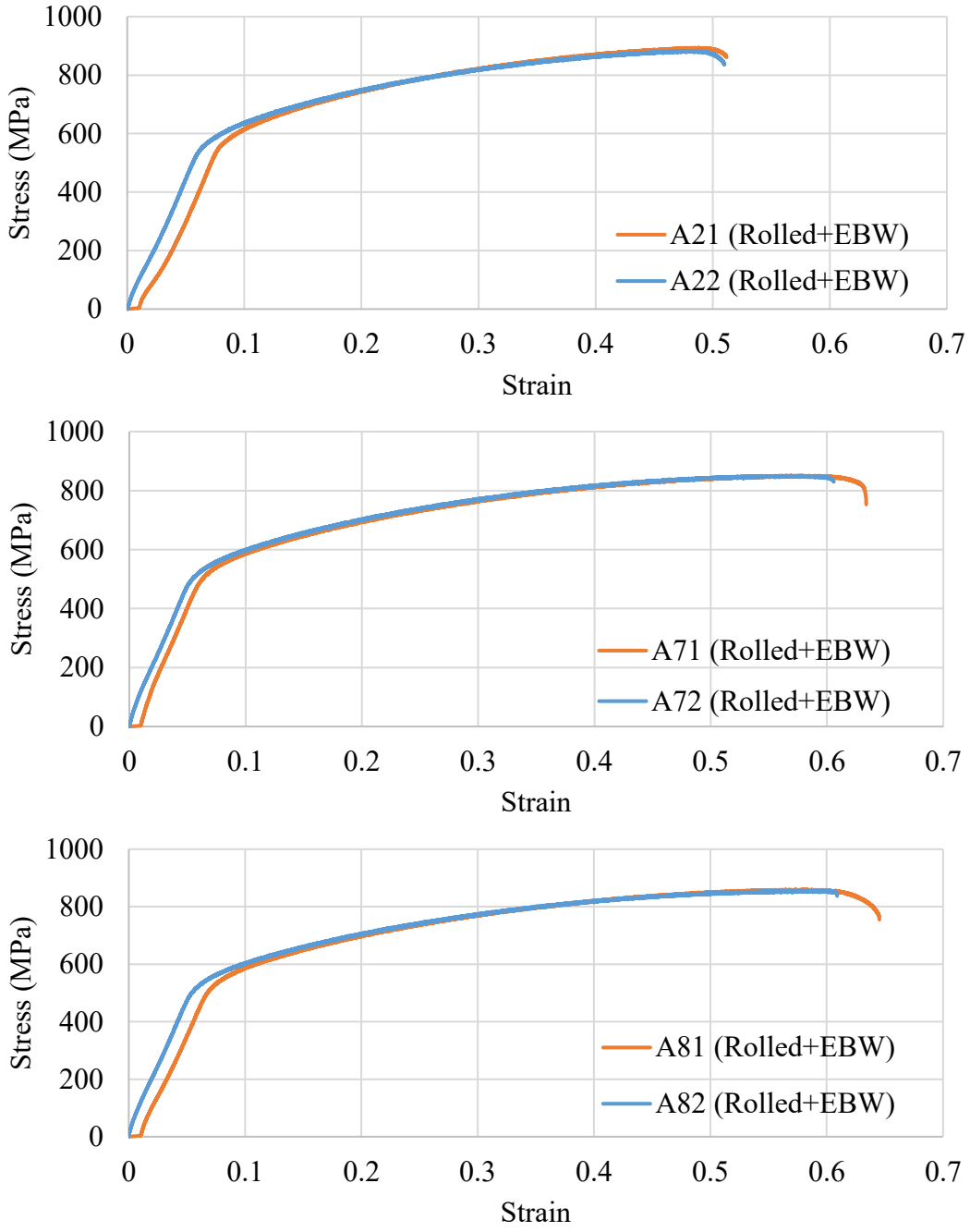

Figure C.2 Tensile test stress-strain curves for (a) sample A2 (272.6 J/mm) (b) sample A7 (213.2 J/mm) (c) sample A8 (196.8 J/mm) and their replicates

Note: The curves are shifted horizontally for illustration purposes.

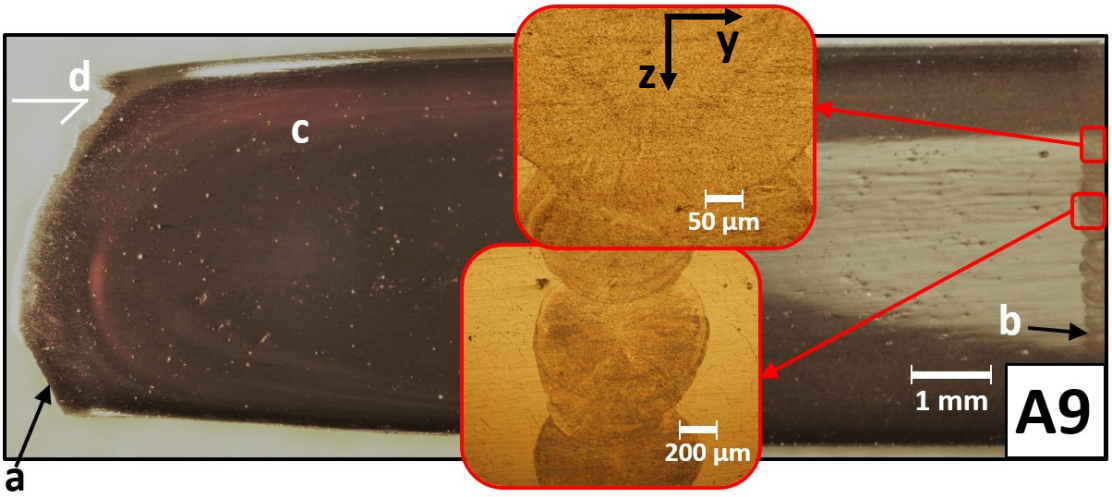

Figure D.1 Sample A9 (180.4 J/mm) fractured outside the weld zone showed no defect in the microstructure of the weld zone when viewed by optical microscope after etching. a: fracture zone, b: weld bead, c: base metal, d: ductile fracture at 45˚ to the loading direction

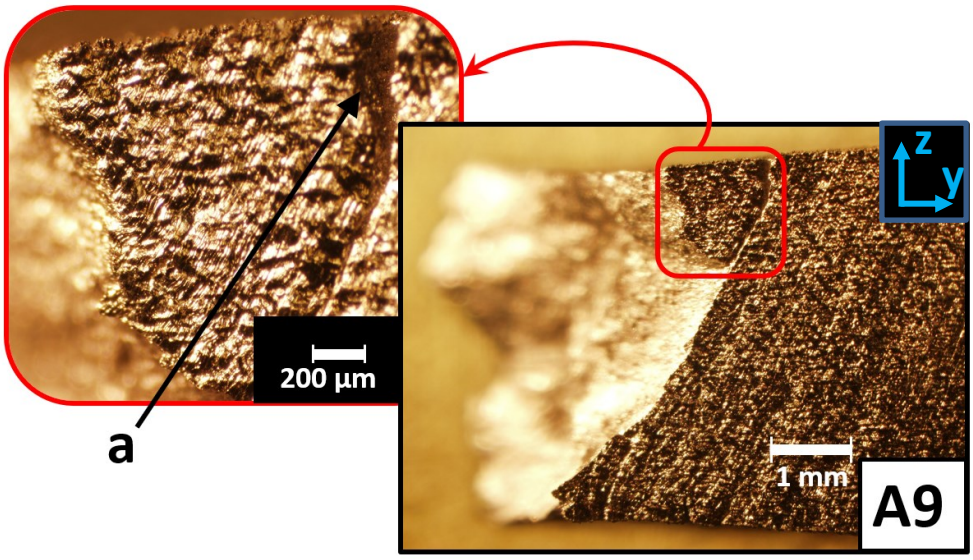

Figure D.2 Sample A9 (180.4 J/mm) fracture zone observed under optical microscope. a: Secondary cracks of width 150 to 200 µm were observed close to fracture zone

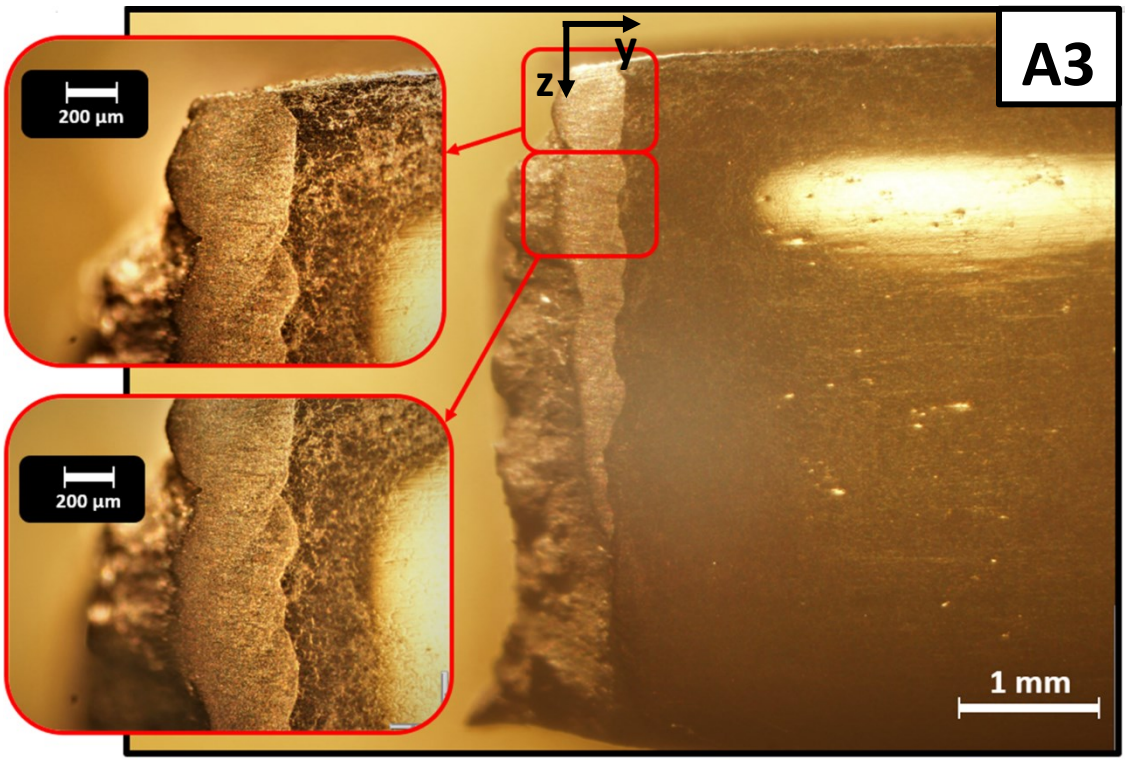

Figure D.3 Sample A3 (249.8 J/mm) fractured through weld zone observed by optical microscope after etching showed less ductile characteristics

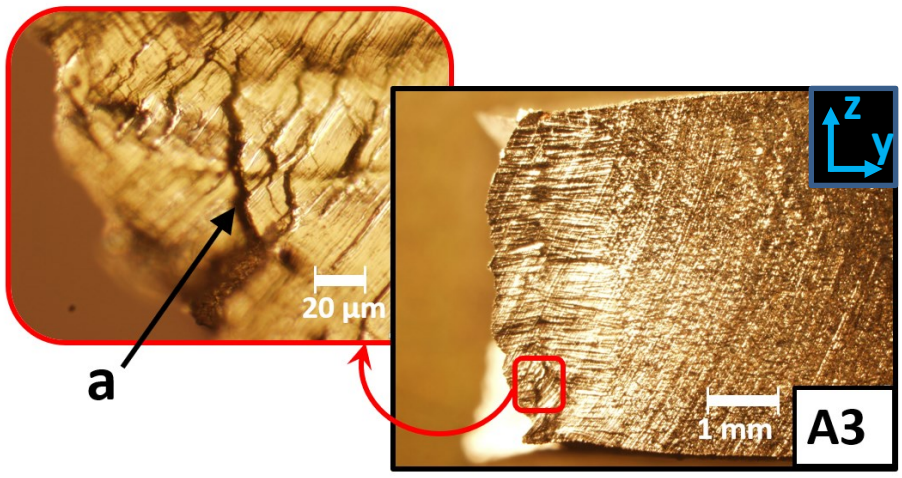

Figure D.4 Sample A3 (249.8 J/mm) fracture zone observed under optical microscope. a: Secondary cracks of width 10 to 20 µm were observed close to fracture zone

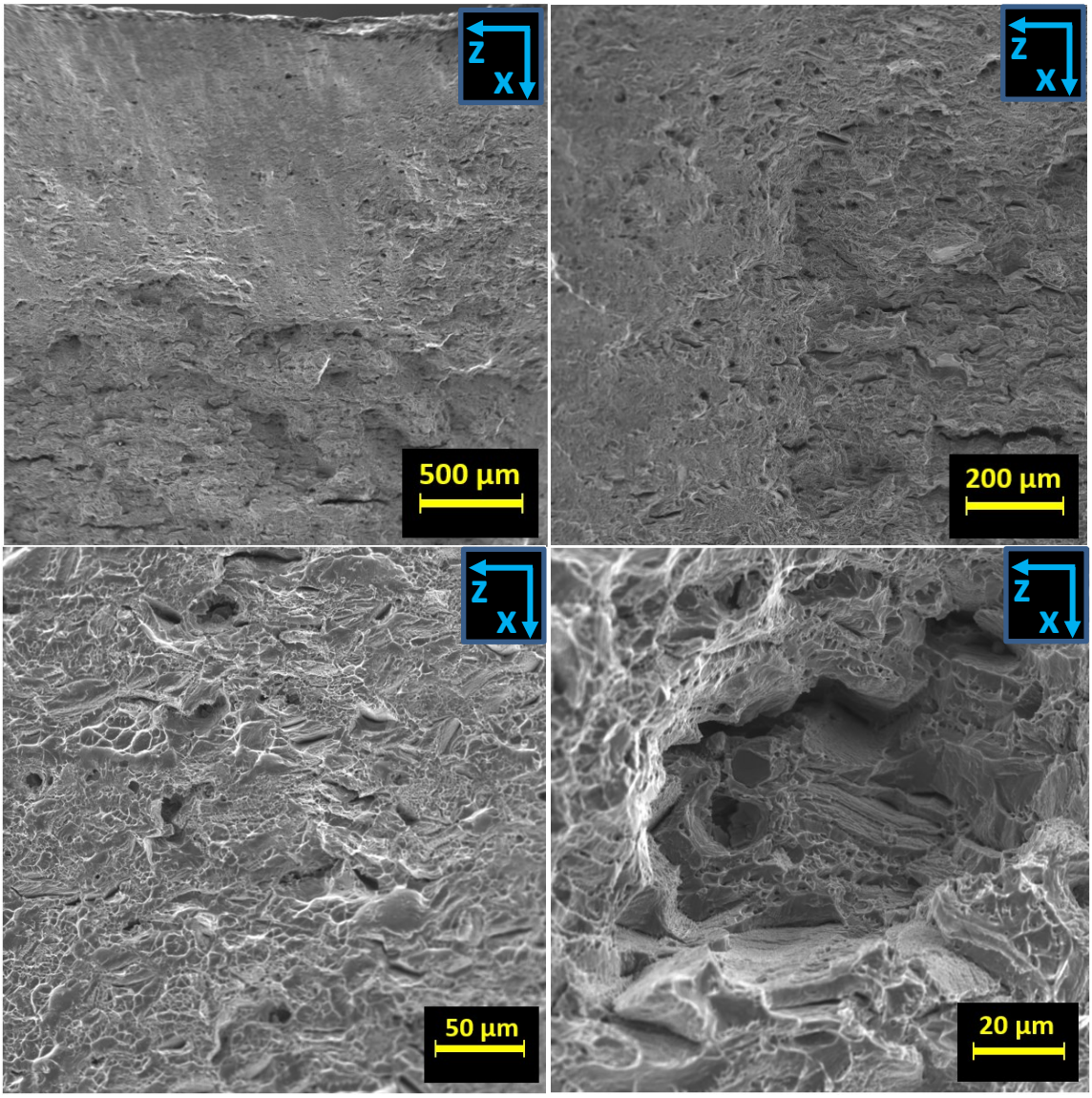

Figure D.5 SEM fractograph of the rolled IN718 sample A91 (heat input 180.4 J/mm)